

Wire and Arc Additive Manufacturing of Manganese Aluminium Bronze

Microstructure Control for Corrosion Resistance

Milan Agnani

Master of Science Thesis

Wire and Arc Additive Manufacturing of Manganese Aluminium Bronze

Microstructure Control for Corrosion Resistance

MASTER OF SCIENCE THESIS

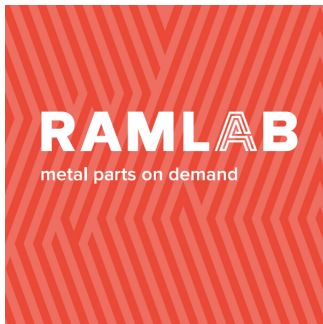
For the degree of Master of Science in Mechanical Engineering - MEA
at Delft University of Technology

Milan Agnani

Supervisor: Dr.ir.M.J.M. Hermans

August 23, 2017

Faculty of Mechanical, Maritime and Materials Engineering (3mE) · Delft University of
Technology



The work in this thesis was performed in collaboration with RAMLAB, Rotterdam. Their cooperation is hereby gratefully acknowledged.



Department of Materials Science and Engineering (MSE)

Abstract

Wire and Arc based Additive Manufacturing (WAAM) processes are novel technologies that are seen as promising candidates for fabricating complex 3-Dimensional large scale components. These processes offer avenues to locally tailor metallurgy of the melt pool and thus produce functionally and compositionally graded components for improved performance in extreme conditions. This thesis explores in-situ alloying of commercial Manganese Aluminium Bronze (MAB) with copper rich Cu₃Si filler wire during deposition, as a microstructure control strategy for designing components that are resistant against selective phase corrosion.

Evolution of microstructure during WAAM processing of MAB and during in-situ alloying with Cu₃Si wire is investigated using optical and electron microscopy, x-ray diffraction and fluorescence. The microstructure of the as-deposited MAB bead is observed to change from continuous connected dual phase to cellular single phase upon controlled addition of Cu₃Si in a MAB melt pool. Corrosion tests showed reduced severity of surface attack and an improvement in the rate of corrosion by 3 times for the new alloy. Thus this technique can be used in industries to improve corrosion resistance as an energy efficient alternative of conventional high temperature aging treatments.

Additionally, the possibilities of improving mechanical behaviour of the new alloy (cellular single phase) are explored using the principles of grain refinement in the context of WAAM.

Table of Contents

Acknowledgements	xi
1 Introduction	1
1-1 Wire and Arc Additive Manufacturing	1
1-2 Material	2
1-3 Corrosion Behaviour	3
1-4 Outline	4
2 Literature Review	5
2-1 Microstructure	5
2-1-1 Phase Transformations	6
2-1-2 Nature of Phases	8
2-2 Corrosion Resistance	9
2-2-1 Forms of corrosion	9
2-2-2 Mechanism of corrosion	9
2-2-3 Microstructure control	11
2-3 Wire and Arc Additive Manufacturing	13
2-3-1 Process	13
2-3-2 Microstrucutre	14
2-3-3 Microstructure Contol	16
2-4 Conclusions	18
3 Parametric Analysis	19
3-1 Introduction	19
3-2 Experimental Apparatus	19
3-3 Experiments	21
3-4 Results and Discussions	22
3-4-1 Raw Materials	22
3-4-2 Parameter study	22
3-4-3 Layer deposition study	27
3-5 Conclusions	30

4	In-situ Alloying	33
4-1	Introduction	33
4-2	Experiments	33
4-2-1	Compositionally Graded Deposition	34
4-2-2	Optimal Alloying	35
4-2-3	Solidification Analysis	35
4-3	Results and Discussions	35
4-3-1	Compositionally Graded Deposit	36
4-3-2	Alloy Analysis	42
4-3-3	Solidification Analysis	44
4-4	Conclusions	47
5	Corrosion Behaviour	49
5-1	Introduction	49
5-2	Experiments	49
5-2-1	Materials	50
5-2-2	Electrochemical Polarization	51
5-2-3	Surface Morphology Analysis	51
5-3	Results and Discussions	52
5-3-1	Microstructure	52
5-3-2	Potential - pH Diagram	52
5-3-3	Electrochemical Polarization	53
5-3-4	Surface Morphology Analysis	56
5-4	Conclusions	57
6	Grain Refinement	59
6-1	Introduction	59
6-2	Experiments	60
6-3	Results	61
6-3-1	Process	61
6-3-2	Microstructure	61
6-3-3	Hardness	64
6-4	Discussion	65
6-4-1	Microstructure	65
6-4-2	Hardness	67
6-5	Conclusions	68
7	Summary	69
7-1	Conclusions	69
7-2	Outlook	70
A	Aging Analysis of MAB	71
B	Process Parameter - In-situ Alloying	73
	Bibliography	75

List of Figures

1	Wire and Arc Additive Manufacturing - overview	2
2	Applications of Aluminium Bronzes	3
3	Biofouling susceptibility of various structural alloys	3
4	Binary phase diagrams	6
5	Microstructure of Manganese Aluminium Bronze quenched at different elevated temperatures from 880 °C	7
6	Schematic of phase transformation and as-cast microstructure	8
7	Selective phase attack on as-cast MAB surface	10
8	Heat treated NAB microstructure. Arrows show globular κ_3 precipitates	11
9	Friction Stir Processing for improved corrosion resistance	12
10	Cross section line scan and atomic sketch of Ni coating on NAB surface, annealed for different times	12
11	Micrographs of as-cast and laser remelted microstructure	13
12	Notional Thermal Profile of WAAM processing of TiAl6V4	14
13	A schematic of constitutional supercooling	15
14	Morphology of primary grains structure based on solidification parameters	15
15	Temperature gradient induced grain morphology	16
16	(a) Solidification map of grain morphology (b) Grain refinement by trace boron addition	17
17	Gas Tungsten Arc Welding setup	20
18	Optical micrographs of MAB wire and NAB substrate	22
19	Macrographs of cross-sectional geometries of the deposits	23
20	A schematic of primary grain growth during AM deposition in Argon atmosphere	23
21	Optical micrographs of WAAM processed MAB deposits	24
22	Post-processed binary micrographs of MAB100 and MAB150	25

23	XRD patterns for MAB100 and MAB150	26
24	SEM/EDS micrograph and elemental maps of MAB	27
25	Macrostructure of cross-section of 6-layer deposits on NAB base plate	28
26	Optical micrographs of 6-layer deposit	29
27	Hardness trends along the height of 6-layer deposits	30
28	Deposition process parameters for in-situ alloying	34
29	A section of Cu-Al binary phase diagram	36
30	A section of in-situ alloyed compositionally graded deposit	37
31	Scanning electron micrographs and elemental maps Continuous Dual Phase (CDP) microstructure	38
32	Scanning electron micrographs and elemental maps Discontinuous Dual Phase (DDP) microstructure	39
33	Scanning electron micrographs and elemental maps Single Phase Columnar (SPC) microstructure	40
34	Trends in composition and phase fractions	40
35	Trends in hardness values along the length of the deposit.	41
36	Optical micrographs of longitudinal cross section of MABCu deposit	42
37	X-Ray Diffraction patterns of in-situ alloyed MABCu	43
38	Selected sections of MABCu XRD pattern highlighting precipitates.	43
39	XRD pattern of heat treated samples	44
40	Characterization of MABCu aged and quenched from 950 °C	45
41	XRD pattern of MABCu aged at 950 °C and furnace cooled	46
42	Electrodes for electrochemical polarization experiments	50
43	A schematic of experimental setup for electrochemical analysis	51
44	Optical Micrographs of (a) MAB (b) MABHT and (c) MABCu	52
45	Pourbaix diagrams (a) copper (b)manganese (c) aluminium d) Cu11Mn7Al (MAB)	53
46	Open Circuit Potential of alloys under consideration	54
47	Potentiodynamic Polarization results	54
48	Anodic Polarization curves	56
49	Electron micrographs of alloy surfaces subjected to forced corrosion during polarization experiments	57
50	(a) Schematic of coil configuration (b) Experimental setup of grain refinement analysis	60
51	(a) Schematic diagram of grain refinement alloying process (b) Mass % of Fe along the segment, determined using EDS	61
52	Macrostructure of Fe enriched MABCu deposit	62
53	Optical micrographs of different regions in the grain refined deposit	62
54	Scanning electron micrographs of MABCu and Fe enriched MABCu	63
55	EDS elemental distribution maps for Fe enriched MABCu deposit	64

56	A 3D bar plot depicting hardness values of 0.5HV indents marked along the deposit	64
57	Indents categorized according to their microstructural environment (a) columnar (b)coarse equiaxed and (c) fine equiaxed	65
58	Trends in hardness values of different microstructures	65
59	A section of Cu-Fe binary phase diagram	66
60	Optical micrographs of aged MAB samples at (a) 650 °C (b) 750 °C	71
61	Optical micrographs of aged MAB samples at (a) 850 °C (b) 950 °C	72
62	XRD pattern of MAB aged at 650 °C and MAB as-deposited	72
63	Parameter selection for in-situ alloying	73

List of Tables

1	Composition of MAB wire and NAB substrate determined by XRF analysis (wt %)	20
2	GTAW process parameters for the parametric analysis experiments	21
3	GTAW process parameters for the layer buildup analysis experiments	21
4	Area fraction of α and β phases (in %) in the MAB deposits	26
5	Elemental Composition of Cu3Si filler wire determined by XRF analysis (wt%) . .	34
6	Process parameters for optimal in-situ alloying	35
7	Heat treatment parameters for solidification analysis of MABCu	35
8	Elemental composition of MABCu deposit determined by XRF analysis (wt%) . .	42
9	GTAW process parameters for MAB sample	50
10	GTAW process parameters for the MABCu sample	50
11	Potentiodynamic Polarization parameters	55
12	Processing parameters for grain refinement analysis	60
13	Heat treatment parameters for aging analysis of MAB	71
14	Parameter selection for in-situ alloying	73

Acknowledgements

First and foremost, I offer my gratitude to my supervisor, Dr.ir. Marcel Hermans for providing me with the his strong support and guidance while allowing me with intellectual freedom to define my own approach. Elaborate and insightful discussions with him were always an immense source of knowledge and have greatly contributed to my understanding of metallurgy. I can not imagine a more supportive and friendlier supervisor. I would also like to thank Dr. Yaiza Gonzalez Garcia as her guidance has been instrumental towards the outcomes of this work. She and her group members were always there to help me in crucial times and I can not thank them enough.

Results in this thesis have been accomplished through the help and support of various people at MSE department. I would like to appreciate Remko Seijffers, Richard Huizenga, Agnieszka Kooijman and Ruud Hendrikx for helping me with the nuances of experiments and for sharing their knowledge with me. I was lucky to have friendly colleagues including Gautam, Constantinos, Ashwath and Ankit with whom I enjoyed working in lab and discussing results, I am thankful to their cheerful presence and the insightful conversations. This report has countless contributions from kind souls I was fortunate to meet at TU Delft and I am indebted to them for their help.

Beyond this project, I am grateful to Prof. Sietsma and Dr. Zalao for giving me the opportunity to explore metals research. I am glad I could learn from them and develop a foundation in experimental research. I should also acknowledge my professors at MEMS,IITB, specially Prof. Ballal for inspiring me to pursue materials research.

My stay in Delft has been fun and lively. I want to thank the pillars of my social support here, Divyam for sharing nostalgia in good times, Ayushmaan for sharing pop-culture craze, Salil for random pep talk during self-inflicted crisis, Rhythima and Vinay for pseudo-intellectual discussions. Further, I am thankful to Rimit, Joe and friends at MSE who were always there for fun when needed and otherwise.

Lastly, I would like to thank my parents and my sister for their unconditional love and support since forever. "Thanks" is just a word, but it means much more here.

Delft, University of Technology
August 23, 2017

Milan Agnani

Master of Science Thesis

Milan Agnani

Chapter 1

Introduction

Development of most modern technologies is intimately related with the availability of suitable materials. As a result, advancements in materials development are often the forerunners to the technological progress of the society [1]. Materials research aims to explore the relationships between material, processing techniques and the resulting properties for an application. The knowledge gaps within these domains are bridged via the means of microstructure. In recent years, metal additive manufacturing is gaining importance as a viable alternative for conventional processing techniques like casting, milling and forging. This opens up new avenues to explore - microstructure-property relationships associated with this processing technique. However, current research of Metal AM involves only a few commercial (TiAl6V4, SS316L) alloys, other alloys are largely unexplored [2, 3, 4]. Various roadmaps indicate that materials development is a key challenge that needs to be addressed to realize full potential of these AM technologies [5, 6].

Aerospace industry is utilizing the potential of additive manufacturing (wire and arc based) to fabricate large scale components [7]. Ship building industry can greatly benefit from the development in additive manufacturing. The current work is aimed at fabricating (potentially repairing and reconstructing) marine propellers for container vessels. For this application, it is of utmost importance that the propeller has both high strength and high resistance to corrosion in marine environment. Processing of Manganese Aluminium Bronze (MAB), a copper alloy with excellent sea water corrosion resistance, using Wire and Arc Additive Manufacturing (WAAM) is explored in this work. To achieve this, a comprehensive understanding of all the components, the material - aluminium bronzes, the processing -WAAM and the phenomenon of corrosion in marine environment is essential towards an informed WAAM based alloy development. These aspects are individually discussed in sections below.

1-1 Wire and Arc Additive Manufacturing

WAAM is a novel technique of fabricating large structural components layer by layer. A WAAM setup consists of a conventional welding setup as a heat source, a wire feeder and

a robotic arm to guide deposition schematically shown in Figure 1 (a). The material is deposited only at desired location to achieve a near net shape. This results in reduced material wastage as it is fundamentally different from conventional subtractive manufacturing where material is removed from undesirable places. Additionally, more complex geometries and customized components, for example hollow propeller blades, can be fabricated using additive manufacturing [4, 5].

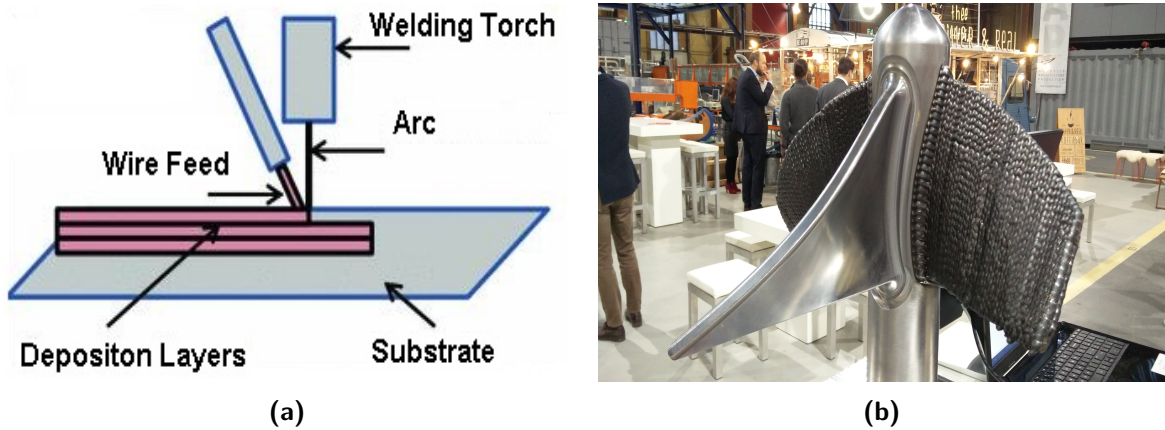


Figure 1: (a) Schematic of wire and arc additive manufacturing [5] (b) A WAAM processed propeller at RAMLAB[8].

Conventional propellers are manufactured using casting methods which leads to thick sections of coarse microstructures and hence inferior mechanical properties. Strength of the structure is further reduced due presence of casting defects like porosity [9, 10]. Additionally, lead production timings for such a cast propellers are often in the range of a few months. Thus WAAM is a feasible alternative since it results in fine microstructure, defect free builds and lead times of a few weeks [11]. A WAAM processed propeller at RAMLAB, Rotterdam is shown in Figure 1 (b). Hence, there is an impetus to explore the metallurgical aspects of WAAM processing of MAB.

1-2 Material

Alloys of copper and aluminium, known as aluminium bronzes are an important and widely-used class of engineering materials. These metallurgical systems along with various alloying additions like Fe, Ni, Mn and Si offer a diverse range of properties and thus are fit to serve in diverse environments. One such important alloy system, known as manganese aluminium bronze (MAB) is characterized by a composition consisting of typically 11% - 13% Mn, 6% - 8% aluminium, upto 3% nickel and iron each.

MAB has a complex multiphase microstructure comprising of an equilibrium FCC α , a high temperature BCC β and intermetallic precipitates κ . By virtue of its microstructure, Al bronzes offer a combination of properties like high strength, ductility, wear-resistance, resistance to biofouling and other forms of corrosion like pitting and erosion [12].

Due to these properties, MABs are used in aerospace, marine and offshore industry. For example, in aerospace industry their main application is in landing gear bearings. Properties



Figure 2: Applications of aluminium bronzes (a) ship propeller (b) offshore pipeline [12]

like bearing resistance against steels, high strength, wear resistance and corrosion resistance against de-icing salts makes MAB an ideal alloy system for the application. Most importantly due to its excellent sea water corrosion resistance and resistance to cavitation corrosion, it is used extensively in marine environments for applications like fabrication of propellers for commercial vessels and cruisers. Hence, in the current work, emphasis has been laid on the corrosion resistance of the alloy [13].

1-3 Corrosion Behaviour

Propellers are subjected to harsh corrosive marine environments which contain corrosive components like 3% NaCl which acts as electrolyte to enhance electrochemical reaction, dissolved oxygen which is unevenly distributed, results in electrochemical reactions and biofouling i.e. sedimentation of organisms and debris (shown in Figure 3).



Figure 3: Susceptibility to biofouling of various alloys. No.1-10, 24-26 are copper alloys, 11-14 nickel, 22-23 Titanium and rest are steels. Copper alloys show lowest susceptibility. [12]

Depending upon the application, components can be prone to various forms of corrosion like crevice corrosion and pitting in pump fittings, erosion corrosion due to liquid flow and selective phase corrosion in steady sea water [12]. While ferrous alloys are found to be unsuitable in such corrosive environments, aluminium bronzes offer excellent corrosion resistance along with a strength equivalent to some of the low alloy steels. In this work, selective phase corrosion of MAB has been identified as a key concern due to its complex multi-phase microstructure and thus microstructure is designed for improved resistance against selective phase corrosion.

1-4 Outline

This report primarily explores strategies for microstructure control during wire and arc additive manufacturing. The emphasis lies on alloy design and microstructure development for improved selective phase corrosion resistance of WAAM processed MAB alloy.

Chapter 2 discusses the existing knowledge on the microstructure of the material, corrosion behaviour of alloy in seawater and metallurgical aspects of WAAM. Additionally, previous works on microstructure control strategies in relevant domains of WAAM processing and corrosion resistance are discussed. Based on them, the scope of the problem and methodology is then described.

Evolution of microstructure during WAAM is discussed in detail in Chapter 3 . Influence of process parameters and layerwise deposition are investigated. In Chapter 4, in-situ alloying during deposition has been implemented to fabricate compositionally graded deposits. A new alloy is developed with emphasis on improving corrosion resistance. Its microstructure and non-equilibrium solidification behaviour is investigated. Subsequently in Chapter 5, the corrosion behaviour of WAAM processed MAB and the newly developed alloy is investigated.

Chapter 6, an exploration, discusses preliminary attempts aimed towards enhancing mechanical properties of additively manufactured α Al-bronze. Concepts of grain refinement are explored in the context of WAAM processing. Finally Chapter 7 summarises the conclusions are drawn from the work and recommends directions for future research.

Chapter 2

Literature Review

The following chapter aims to present the background knowledge associated with microstructure control during Wire and Arc Additive Manufacturing (WAAM) of Manganese Aluminium Bronze (MAB) for improved corrosion resistance.

MAB has a complex multiphase microstructure due to the presence of multiple alloying elements (Al, Mn, Fe and Ni). The development of microstructure, including the role of the mentioned alloying elements, equilibrium solidification microstructure and nature of stable phases are discussed in a greater detail later in section 2-1.

A peculiar property which offers immense functionality to this alloy is its excellent resistance to seawater corrosion. The corrosion behaviour of the alloy including its susceptibility to various forms of corrosion and mechanism of corrosion is discussed in section 2-2. This is done with a focus on the applications of MAB in marine environment as a propeller. Furthermore, in section 2-2, it also discusses the existing approaches towards tailoring microstructure for improved corrosion resistance of these alloys.

Subsequently, metallurgical aspects of wire and arc additive manufacturing is discussed in section 2-3 with an emphasis on nonequilibrium solidification. Recent works aimed at microstructure control during processing are also discussed. Lastly, in section 2-4, based on the literature review, research methodology is presented.

2-1 Microstructure

In MAB, various alloying elements serve different purpose. Aluminium content ranges from 7-9% and is the main strengthening element. Manganese improves castability and weldability along with improving strength. 6% manganese provides strengthening equivalent to 1% aluminium. Nickel upto 3% in conjunction with iron (also 3%) improves corrosion resistance and mechanical strength. Since iron has low solubility in copper, it helps in grain refinement and increases toughness [13].

It has been reported that the microstructure of MAB comprises of a FCC based Cu rich solid solution called α , a high temperature BCC β phase and some strengthening intermetallic precipitates collectively denoted as the κ phases. Figure 4 depicts Cu-Al binary phase diagram and a section of Cu-Al equilibrium diagram with 12% Mn, 8% Al, 2.8% Fe and 2% Ni [13].

In Figure 4 (b), the alloying elements, Fe and Ni, introduce an intermetallic phases known as κ . In addition to that, the detrimental hard phase γ can be avoided at greater concentrations of aluminium. In the section below, the phases and intermetallics are discussed in detail by the means of a sequence of phase transformations during slow solidification.

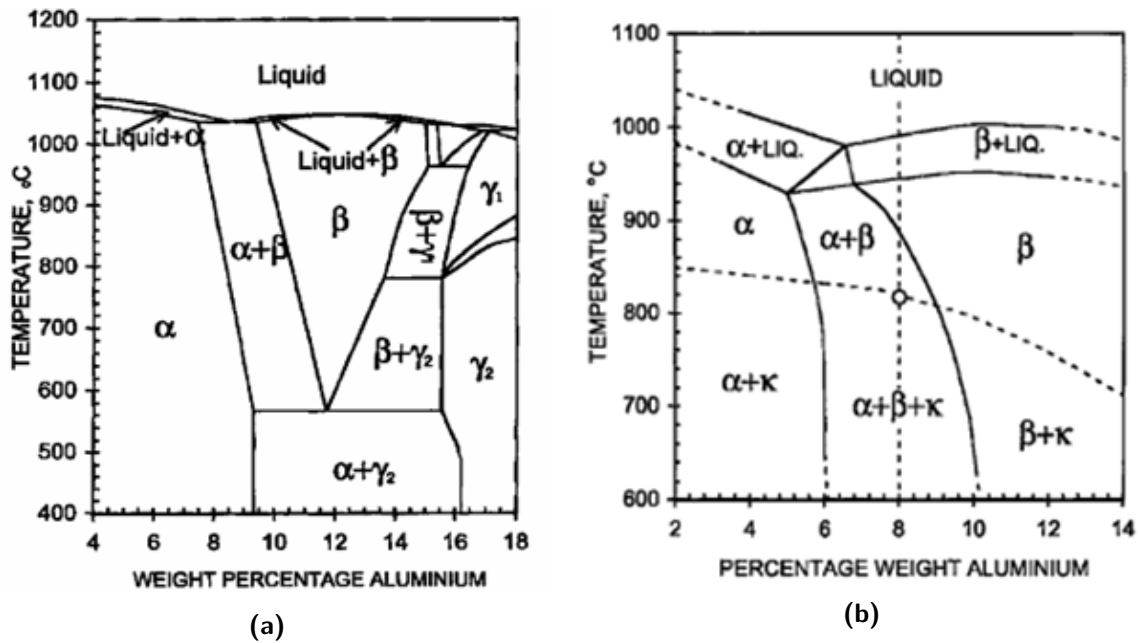


Figure 4: (a) Equilibrium binary diagram of Cu- Al system (b) A section of Cu-Al binary diagram with 12% Mn, 8%Al, 2.8% Fe and 2% Ni [13]

2-1-1 Phase Transformations

Iqbal et al. investigated the development of microstructure of CuMn11Al8Fe3Ni3 alloy at elevated temperature [14]. Alloy specimens were heated to 880 °C, followed by cooling at 5 °C/min. Specimens were subsequently quenched at different temperatures to gain insights into stability of phases -

- After quenching from 880 °C, the microstructure consists of β phase with undissolved particles. The same particles were also observed at 950 °C close to liquidus. Fig 5 (a)
- After quenching from 825 °C, it was observed that α phase grew at the grain boundaries of β grains and around existing dendritic particles. Fig 5 (b)
- At 775 °C, dendritic precipitates emerged in β phase. Fig 5 (c)
- After quenching from 730 °C, the above mentioned precipitates were enveloped in growing α . New precipitates were observed at α/β interface. Fig 5 (d) and (e)

- After quenching from 670 °C , α grows further, enveloping the newly formed precipitates. Even more precipitates grow at the displaced phase boundaries. Cuboid particles precipitate within α grains. Fig 5 (f)
- After quenching from 500 °C , microstructure Fig 5 (g) looks like the as cast Fig 5 (h)

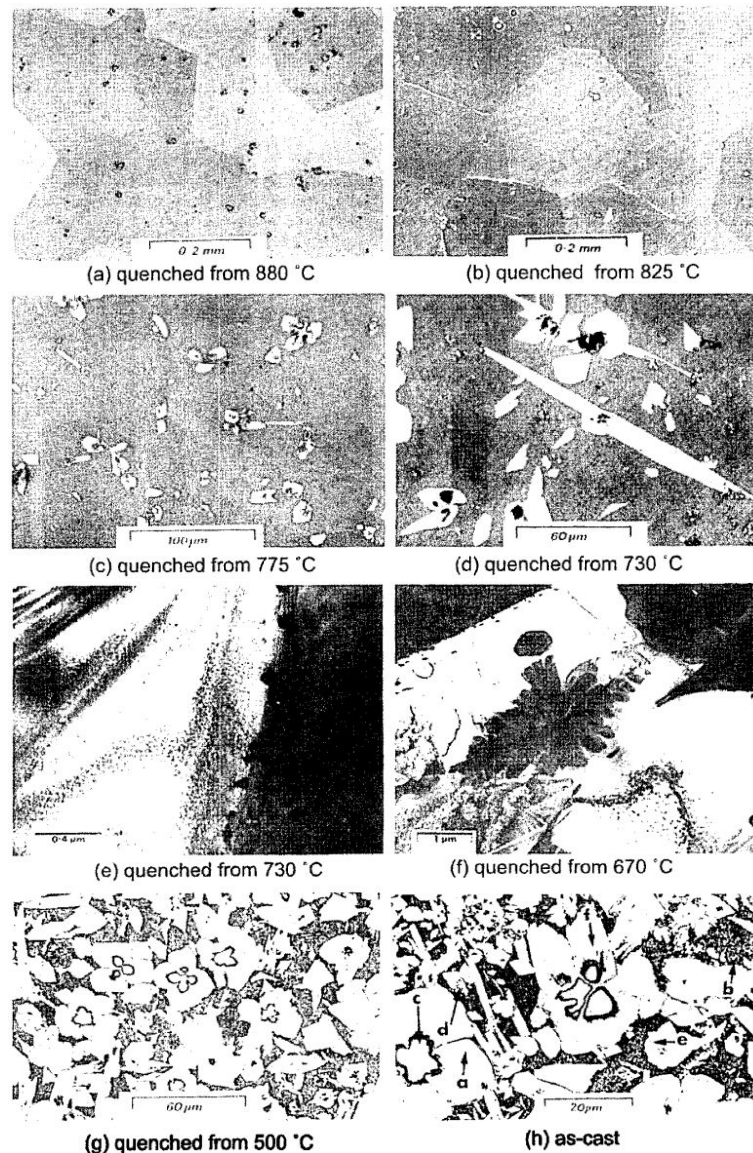


Figure 5: Microstructure of manganese aluminium bronze quenched at different elevated temperatures from 880 °C [14].

The as-cast microstructure consists of a light-etched α phase, a dark-etched β phase, large dendrites, small dendrites, globular and cuboidal precipitates. The schematic diagram Figure 6 below shows series of phase transformation and an as-cast microstructure.

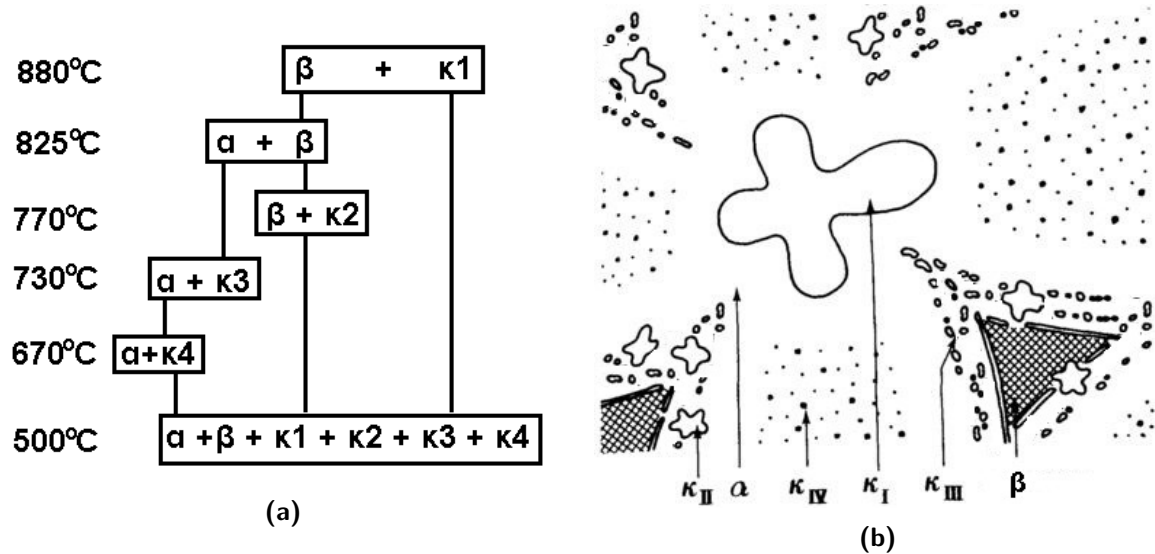


Figure 6: Schematic representation of (a) solidification phase transformation (b) as cast microstructure [15]

2-1-2 Nature of Phases

The phases present in the microstructure are discussed below -

- **The α phase** - A copper rich stable solid solution with FCC structure. α phase contains certain amount of dissolved Ni and Mn along with Fe rich κ precipitates. α phase is primarily responsible for the ductility of the alloy whereas the other phases provide the strengthening
- **The β phase** - It is a high temperature intermediate phase that has a body centered cubic structure and is a solid solution with dissolved Fe, Ni, Al and Mn. In general it has a higher concentration of aluminium than the average Al alloy composition.
- κ 1 are large dendritic Fe and Mn rich precipitates found in the middle of α grains. It is suggested that they form from within the melt
- κ 2 are smaller dendritic precipitates rich in Fe, Mn and Al. They form in β phase and are then engulfed by α
- κ 3 are globular precipitates that form in α near the α - β interface. They are rich in Fe, Mn, Cu and Al with a bcc structure based on
- κ 4 are cuboidal precipitates peppered within the α grains. Composition is similar to κ 3 based on γ (Fe).

The microstructure discussed above corresponds to an as-cast near equilibrium microstructure [13]. The evolution of microstructure under non-equilibrium solidification condition during WAAM processing is discussed in Chapter 3.

2-2 Corrosion Resistance

With its complex microstructure and presence of alloying elements, manganese aluminium bronze offers high strength and resistance to corrosion. Thus it is widely used for marine applications under corrosive environments and extreme mechanical loading.

In order to have a good corrosion resistance various factors like presence of a protective coating, absence of corrodible phases or discontinuous corrodible phases. The alloy derives its corrosion resistance from a thin adherent copper/aluminium rich oxide layer Cu_2O and Al_2O_3 . Due to the presence of Al_2O_3 , the protective film has high hardness and hence is resistant to erosion corrosion too [13]. In this section, the material behaviour under attack of various forms of corrosion is briefly discussed. Later, the mechanism of corrosion and corrosion prevention is discussed in detail.

2-2-1 Forms of corrosion

Pitting: It generally occurs due to localised damage to the oxide or presence of defects on the surface as it results in differential aeration of the surface. Defects like slag inclusions, porosity or oxide inclusions are a common site for initiation of pitting [12].

Crevice corrosion: Crevice is an area where two surfaces are in close contact but there is a thin layer of corrosive medium between them. Such assemblies are common in pipeline joints under the sea. Such a thin layer is void of oxygen and the differential aeration leads to crevice corrosion due to complex electrochemical reactions which will be discussed later. Such a corrosion can be avoided by heat treatment by allowing the oxide layer to form under control[13].

Biofouling: It is a form of macro corrosion which can have a major impact on sea water structures as it obstructs water flow and adds weight. MAB and other Cu alloys are observed to have high resistance to biofouling. Figure 3 shows results of biofouling experiments on structural alloys. Steels, aluminium alloys and titanium alloys show extensive biofouling whereas copper alloys are resistant to biofouling [12].

Selective Phase Corrosion: Due to complex multi-phase microstructure of as-cast alloy, there is presence of more noble and less noble phases adjacent to each other in the microstructure. In this case, the less noble phase selectively corrodes. In manganese aluminium bronzes, the Al-rich β phase and the Fe rich κ phases are highly corrodible. Figure 7 shows selective attack at the κ_1 precipitate and α - β phase boundaries when as-cast MAB was immersed in 3.5% NaCl [16].

The section below discusses the mechanisms of electrochemical corrosion with an emphasis on selective phase corrosion.

2-2-2 Mechanism of corrosion

Corrosion in metal takes place when a positively charged ion leaves the surface and enters the corrosive medium. The rate of corrosion depends on the inherent tendency of the metal relative to that specific medium and is called its electrical potential in that medium.

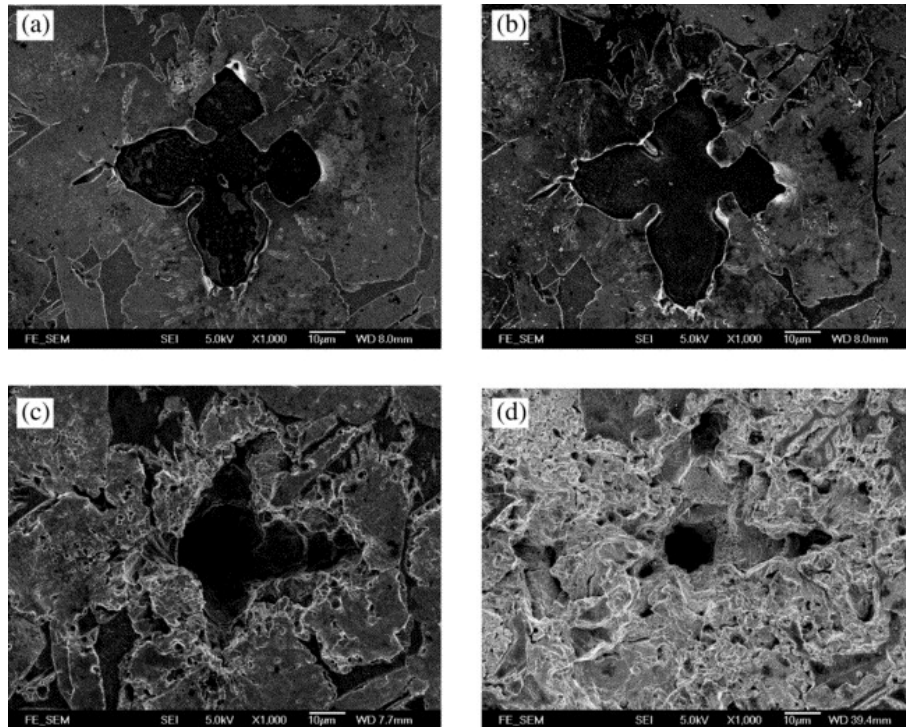


Figure 7: Selective phase attack on as-cast MAB surface in 3.5%NaCl solution (a) 30s b) 2.5 min (c) 30min and (d) 90 min. κ 1 and β phase have preferentially corroded [16].

Most alloys see a range of these potentials in seawater depending on water temperature, turbulence, aeration, pH and presence of other ions. Presence of a hard and noble oxide film over the metal prevents or significantly reduces the rate of discharge of these ions from the surface of metals. However, due to processes like erosion, the film may get damaged, leaving localised areas prone to corrosions, thus resulting in pitting.

A single metal is less prone to corrosion as opposed to two dissimilar metals that are in electrical contact. This arrangement is called a galvanic couple and the corrosion is called galvanic corrosion. Based on the surrounding medium, the more electropositive metal is cathodic and the more electronegative metal is anodic. An electrolytic cell is formed where ions move through the medium and electrons through the metals [13].

In case of MAB or alloys in general, they solidify in complex microstructures consisting of different phases. These phases vary in compositions and crystal structure with respect to each other. Hence these phases have different electrochemical potential in a corrosive medium. This difference can be as large as 100 mV in case of α and γ phases [17].

In case of aluminium bronzes, Al-rich phase acts as anodic and gets into the solution. Alternatively, the cathodic copper ions redeposit on the corroded anodic phase. The newly deposited copper is porous and appearance seems discoloured. Other alloying elements also undergo selective phase corrosion and hence a generic de-alloying is observed. The rate of corrosion depends on the relative areas of cathodic and anodic phases. Hence a continuous deep rooted network of anodic phases like γ or β can lead to corrosive attacks deep within the bulk of the component.

Hence for good corrosion resistance against selective phase corrosion in static seawater, the anodic phases (β phase in MAB) need to be avoided. This can be achieved by controlling the cooling rate or by changing the composition. Furthermore, it should be ensured that the unavoidable phases like κ_1 do not form a detrimental continuous network [13]. This can be done by heat treatments or mechanical working. In the following section, various existing microstructure control strategies to improve corrosion resistance are presented.

2-2-3 Microstructure control

As discussed in the sections above, in order to improve corrosion resistance, it is important to tailor the microstructure. Nickel Aluminium Bronze (NAB), a similar alloy to MAB with Fe and Ni 5% and Mn 1.5% has been extensively studied. The following section elaborates upon various microstructure control strategies that can be found in the existing literature for NAB. Due to similarities in microstructure, parallels can be directly drawn for MAB. The techniques primarily revolve around avoiding corrodible phases (β) or avoiding the presence of cathodic and anodic phases adjacent to each other. Additionally, in some cases the microstructure is modified to avoid continuous distribution of unavoidable corrodible phase (κ_3) (Not present in MAB).

Heat Treatment : It is the commonly-used industrial practice to improve corrosion resistance. Since the detrimental β phase is a high temperature phase which is retained as a consequence of fast cooling, the components are annealed at an elevated temperature within the range of 500 °C-750 °C for 6hrs. During this heat treatment, the β phase decomposes into $\alpha + \kappa$ phases and the κ_3 precipitates also undergo coarsening. The lamellar κ_3 precipitates spheroidise and as a result, the continuous network along the grain boundaries breaks [12]. The recrystallization temperature of nickel aluminium bronze is about 675 °C. Annealing at a lower range of temperatures, namely from 500 °C-600 °C leads to enhancement of mechanical properties by precipitation of κ_4 phase. In the high temperature annealing range of about 700 °C the ductility of the alloy improves at the expense of its strength. Figure 8 below shows annealed microstructure devoid of β phase consisting of globular κ_3 precipitates [12].

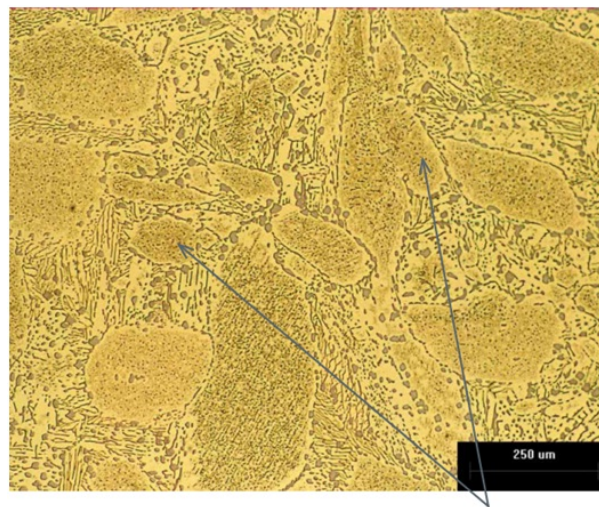


Figure 8: Heat treated NAB microstructure. Arrows show globular κ_3 precipitates [12]

Friction Stir Processing: It is a surface microstructure modification technique derived from friction stir welding. A cylindrical wear resistant tool consisting of a small-diameter pin concentric with a large shoulder is inserted in the surface of material, rotated and made to hover over the surface. As a result, under mechanical stress and frictional loading, the material around the pin gets heated up and locally displaced. This significantly softens the material at elevated temperatures and improves the rate of phase transformations by orders of magnitudes. Oh-ishi et al(2004) investigated the microstructural modification during FSP and reported homogenization, grain refinement, closure of porosity and improvement in mechanical properties near the surface. A schematic diagram in Figure 6 shows friction stir processing and the corresponding micrograph with respect to surrounding as cast microstructure [18].

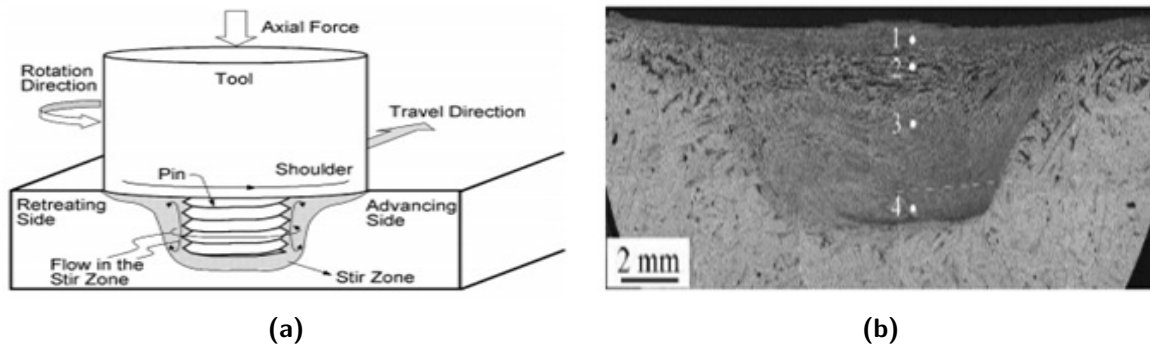


Figure 9: (a) Schematic of Friction Stir Processing (b) Optical micrograph of FSP modified microstructure [18]

Solid Solution Coating: Luo et al.[19] electrodeposited a nano-crystalline Ni layer on NAB alloy. An outer Ni-Cu layer and an inner Cu-Ni-Al intermetallic layer was obtained using intrinsic property of triple diffusion of the system. This resulted in a gradual drop of volta potential along the thickness of Ni-Cu layer thereby reducing the driving force for selective phase corrosion. Improvement in corrosion resistance was also attributed to a protective film of $Ni(OH)_2$ and Cu_2O . Schematic elemental distribution can be seen in Figure 10.

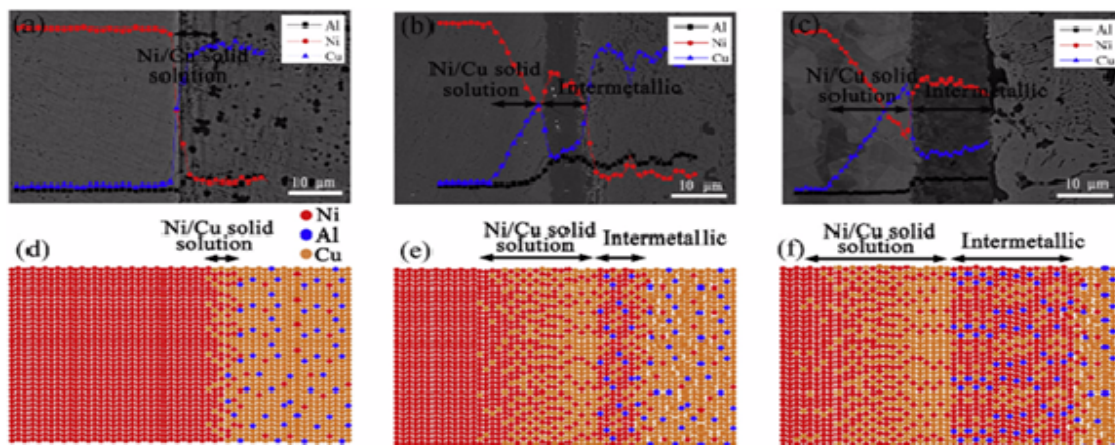


Figure 10: Cross section line scan and atomic sketch of Ni coating on NAB surface annealed for different times (a) 0.5 hrs (b) 6 hrs and (c) 12 hrs [19]

Laser Surface Melting: Tang et al. modified the microstructure of the surface material to improve its resistance against cavitation and erosion corrosion. The rate of cavitation erosion corrosion was reduced by 5 times. Using a Nd:YAG laser, the surface layer was heated until local remelting. This localised heating resulted in high cooling rates. The heterogeneous multi-phase solidification microstructure melted and resolidified as single phase β . Since β has higher hardness, the erosion corrosion resistance increased greatly. Moreover, single phase surface is resistant to selective phase corrosion [16].

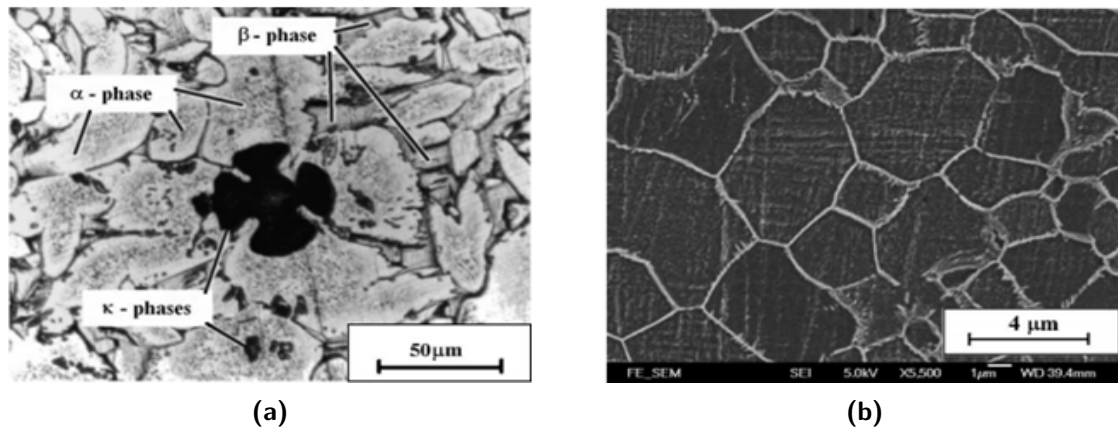


Figure 11: Micrographs of (a) cast microstructure (optical) and (b) laser remelted microstructure (SEM) [16]

A common link between all the approaches was observed. It is concluded that a homogeneous single phase microstructure is desirable for improved resistance against selective phase corrosion. The section below discusses WAAM process with emphasis on its metallurgical aspects.

2-3 Wire and Arc Additive Manufacturing

2-3-1 Process

Wire and Arc Additive Manufacturing (WAAM) is a novel processing technique from the emerging field of Additive Manufacturing (AM). An AM process is characterized by its heat source, raw material and a motion system. In WAAM, the heat source is an electric arc, raw material is a welding filler wire and a robotic arm controls the guides the deposition process. WAAM is suitable for high deposition rate, large components and near net shaped components [4].

From a metallurgical point of view, during WAAM a single layer of metal is deposited on a previous layer. This layer undergoes a non-equilibrium solidification phase transformation. The layers beneath undergo complex thermal cycles of remelting and reheating. This results in a series of liquid and solid state phase transformations. Figure 12 shows thermal profile of a single deposit during WAAM processing of TiAl6V4 [3]. Seven distinct peaks correspond to seven layer depositions. Peak heights decrease as the depositions occur at increasing distance from the layer. The base temperature rises as the heat gets trapped in the built component.

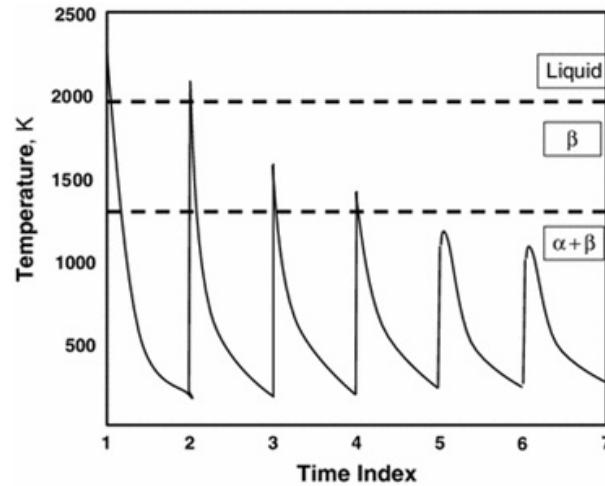


Figure 12: Notional Thermal Profile of WAAM processing of TiAl6V4 [3]

The progressive peak temperatures and cooling rates are dependent on process parameters and material properties while phase transformations depend on the alloy system.

The following report primarily explores strategies of microstructure control during WAAM. The emphasis lies on alloy design and microstructure development for WAAM processed MAB alloy for improved selective phase corrosion resistance.

2-3-2 Microstructure

Local alloy chemical composition and the temperature cycles experienced by the material define the metallurgy of WAAM. The final room temperature microstructure results from rapid directional solidification and subsequent phase transformations from thermal cycling. As a result, metastable phases, columnar morphology and banded microstructure are some common traits of WAAM processed metals [5]. In WAAM, conduction through the substrate and build material is the primary mode of heat transfer. Additionally, convection through shielding gas also offers cooling. Cooling rates of the order of 10^3 °C/s have been reported for WAAM [11]. The primary solidification microstructure is characterized by epitaxial growth perpendicular to the solid/liquid interface, the direction along maximum thermal gradient. Preferred orientation of growth is also observed for example along $\langle 100 \rangle$ direction for cubic metals. During deposition, the solidification front moves with a uniform speed. In doing so, solid expels solute atoms (depending on solubility) into the liquid near the interface. This results in a solute rich liquid, which has a lower liquidus temperature T_L , ahead of the solidification front. Interplay of temperature gradient and this reduction in T_L results in the phenomenon of constitutional supercooling, shown schematically in Figure 13 [20].

Different substructures can be formed in the primary grain structure depending upon composition and rate of solidification as shown in Figure 14. Solidification parameter, given by G/R where G is thermal gradient and R is speed of solidification front, expresses the rate of solidification. Based on this parameter, substructures can take flat, cellular, cellular dendritic or dendritic morphology [20]. From the process' perspective, heat input and torch velocity determine G and R and hence the primary solidification microstructure. In AM, solidification

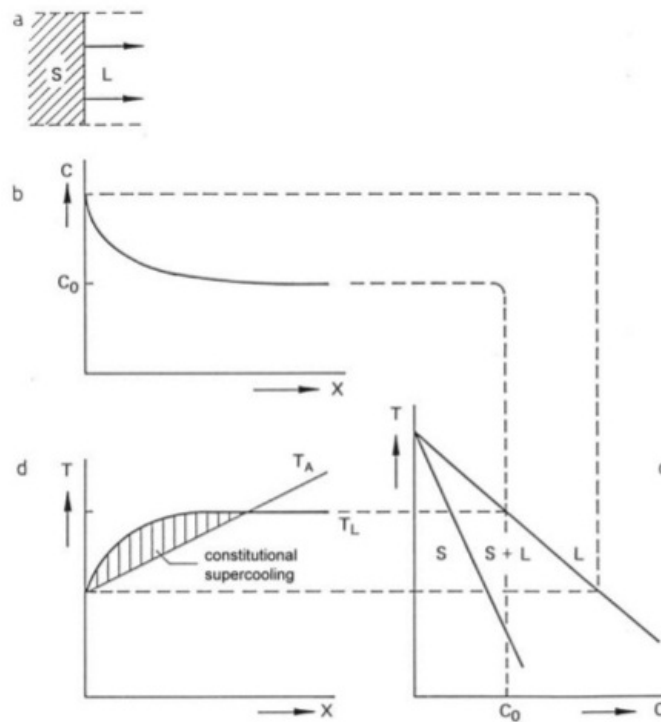


Figure 13: A schematic of constitutional supercooling [20]

process parameter window can be estimated and used to predict the nature of grain structure (columnar -equiaxed) [21, 22]

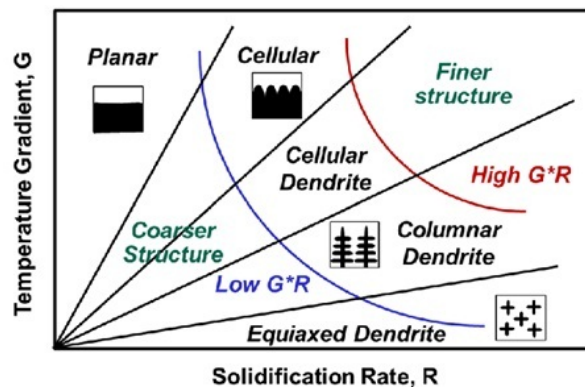


Figure 14: Morphology of primary grains structure based on solidification parameters [23]

Further, the secondary microstructure results from solid state phase transformations. During AM, the material undergoes thermal cycles (Figure 12) resulting in a banded tertiary microstructure [5].

2-3-3 Microstructure Control

Additive Manufacturing offers the possibilities of localized microstructure control by altering the metallurgy of melt pool. In recent years, various microstructure control possibilities have been explored to control macroscopic and microscopic features of AM components aimed towards enhancing their performance [24].

Macro-level properties of interest include porosity, residual stresses and texture. In case of powder bed fusion processes, removing porosity within the components is a key challenge. Some of the approaches to solve this revolve around determining a process parameter window (based on energy density, a function of laser power, scanning strategy and powder characteristics) such that both, lack of fusion and volatilization of constituents can be avoided [25]. Due to thermal cycling during layer deposition and corresponding expansion and contraction during AM processes, residual stresses can be present within the components. Authors propose strategies based on modifying heat source trajectories during deposition to minimize the residual stresses [26]. Due to the directional nature of solidification, a strong texture has been reported for AM deposits [27]. An equiaxed (non-textured) as opposed to a columnar (textured) microstructure can be achieved by manipulating solidification parameters, thermal gradient and rate of solidification (depends on heat input and deposition velocity) [28].

In the current work, however, microstructure control strategies for micro-level features are explored. Existing literature on grain size, morphology and phases is discussed below. Researchers have explored possibility of using parametric process control (to manipulate G and R) and compositional changes to control the phenomenon of solidification.

Thijs et al. [25] deposited subsequent layers in an alternate direction thereby achieving temperature gradient induced grain morphology. Since columnar grain growth takes place along the direction of thermal gradient, reversing the direction results in reversing the angle of columnar grain growth. The schematic and resulting microstructure of this approach is shown in Figure 15.

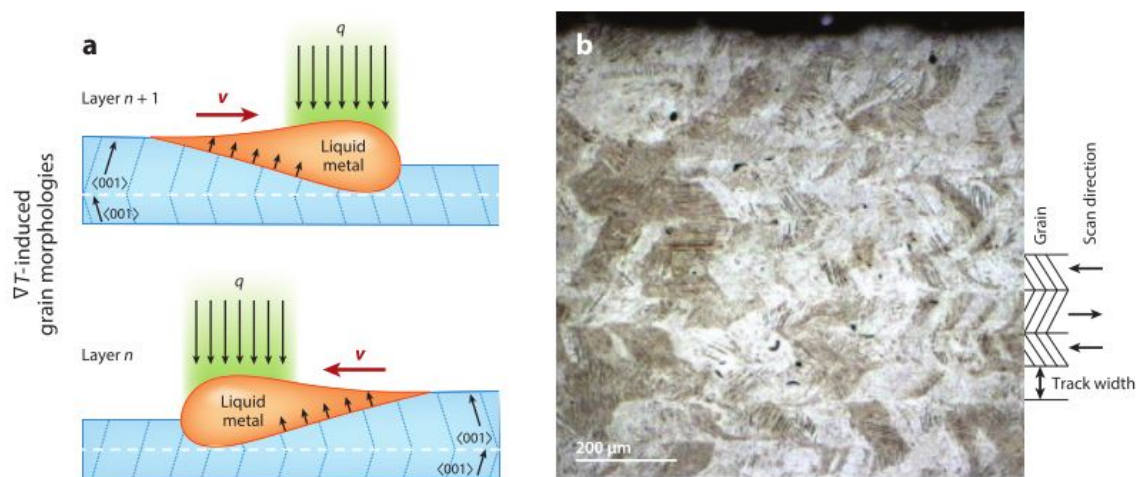


Figure 15: (a) Schematic of Zig-zag molten pool motion on successive layers and (b) corresponding microstructure [24]

Mode of solidification, as shown in Figure 14. can be modified in various ways. The relationship between temperature gradient and grain morphology for a fixed solidification rate is evident from Figure 14. Kobryn and Semiatin studied evolution of grain structures for different processing approaches for TiAl6V4 [29]. Different morphologies (columnar and equiaxed) were obtained using different processing routes as shown in Figure 16 (a). In two separate investigations, additive manufacturing of TNZT, nominally Ti-35Nb-7Zr-5Ta with and without 2% wt Boron showed columnar (strong texture) and equiaxed morphologies respectively. Presence of boride inoculants and increase in solidification range of the alloy was suggested as the reason for it. EBSD maps of the alloys can be seen in Figure 16 (b) [30, 31]

During AM, the large undercooling that governs morphology of primary grains, also impacts the volume fraction, sizes and distribution of phases formed from non-equilibrium solid state phase transformations. Rapid cooling and thermal cycling can produce metastable phases which are conventionally difficult to achieve [24]. For example, Ma et al. performed in-situ alloying of Ti and Al wire to form titanium Aluminide components [32].

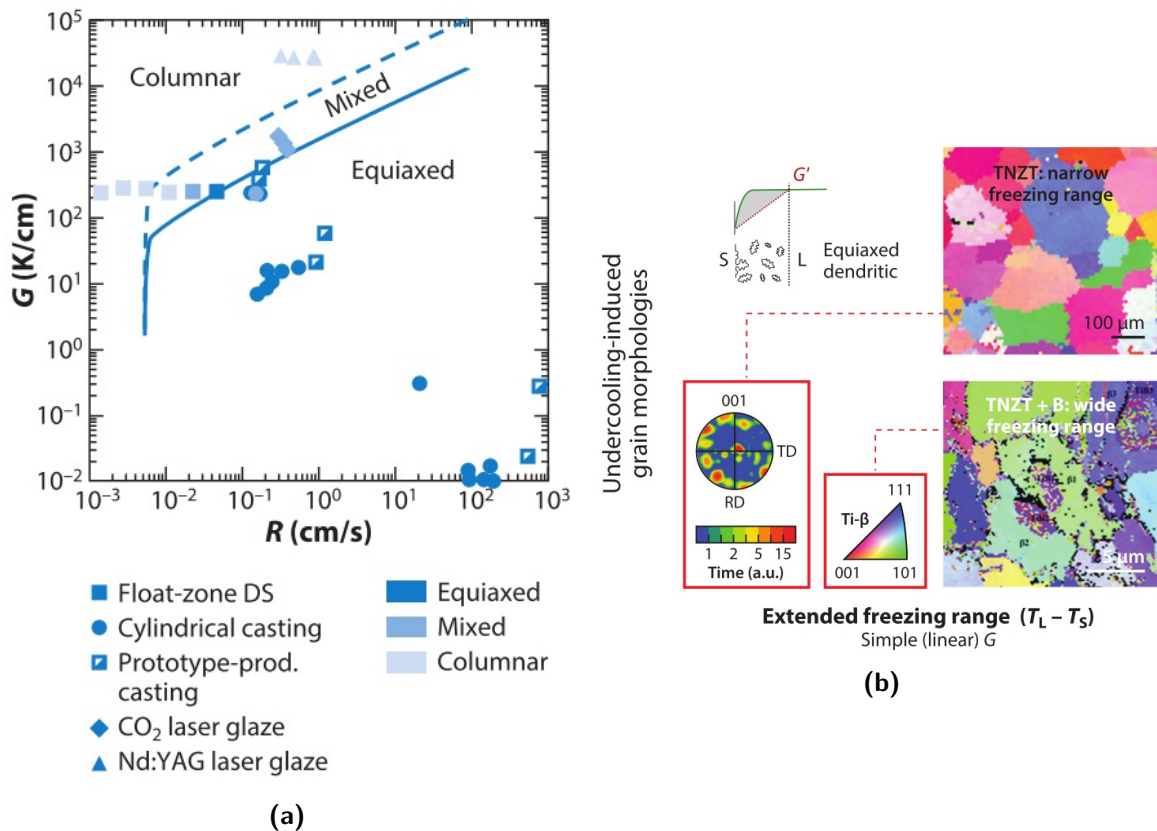


Figure 16: (a) Solidification map of grain morphology for different processing routes of TiAl6V4 (b) EBSD maps showing grain refinement in TNZT by trace boron addition [24].

Hence, process control and compositional manipulation can be utilized for microstructure control aimed at tailoring grain size, morphology and phase distribution during WAAM processing of alloys.

2-4 Conclusions

The key take-aways from the literature review are enlisted below -

- Manganese aluminium bronze has a complex multiphase microstructure consisting of a FCC α phase, a BCC β phase and intermetallic κ phases.
- MAB is used to fabricate propellers due to their corrosion resistance in marine environment. However, presence of continuous corrodible phases (β phase) in its microstructure renders it susceptible to selective phase corrosion in steady sea water.
- Microstructure control surface treatments aimed at obtaining homogeneous single phase fine microstructure have shown improvement in corrosion resistance.
- During the WAAM process, a material experiences complex cycles of solidification and solid state phase transformations. This results a microstructure characterized by directional solidification, metastable phases and cyclic tempering.
- Manipulating process parameters and local composition can help tailor microstructure for desirable grain morphology and phase distribution.

Based on the concepts from literature review, evolution of microstructure during WAAM is investigated in the following chapter. Subsequently, in-situ alloying, a microstructure control strategy is explored with an objective to obtain a single phase microstructure. Finally, corrosion behaviour of WAAM processed and in-situ alloyed material is evaluated.

Chapter 3

Parametric Analysis

3-1 Introduction

Manganese aluminium bronze (MAB) is used in propellers for marine applications due to its high strength and excellent sea water corrosion resistance. It has a complex multi-phase as-cast microstructure consisting of FCC α phase, high temperature BCC β phase and κ intermetallics (section 2-1). Conventionally, casting is used to fabricate these components. It is time consuming and often results in poor mechanical strength due to coarse microstructure and defects like porosity [11]. Wire and Arc Additive Manufacturing (WAAM), a novel processing technique can be used to fabricate large scale defect free components with a fine grained microstructure (section 2-3).

The following chapter discusses evolution of microstructure of MAB during WAAM processing. Firstly, the influence of process parameters (heat input, governed by operating current) on the as-deposited microstructure is investigated. Subsequently, evolution of microstructure as a consequence of cyclic re-melting and reheating during layer-wise WAAM is discussed.

3-2 Experimental Apparatus

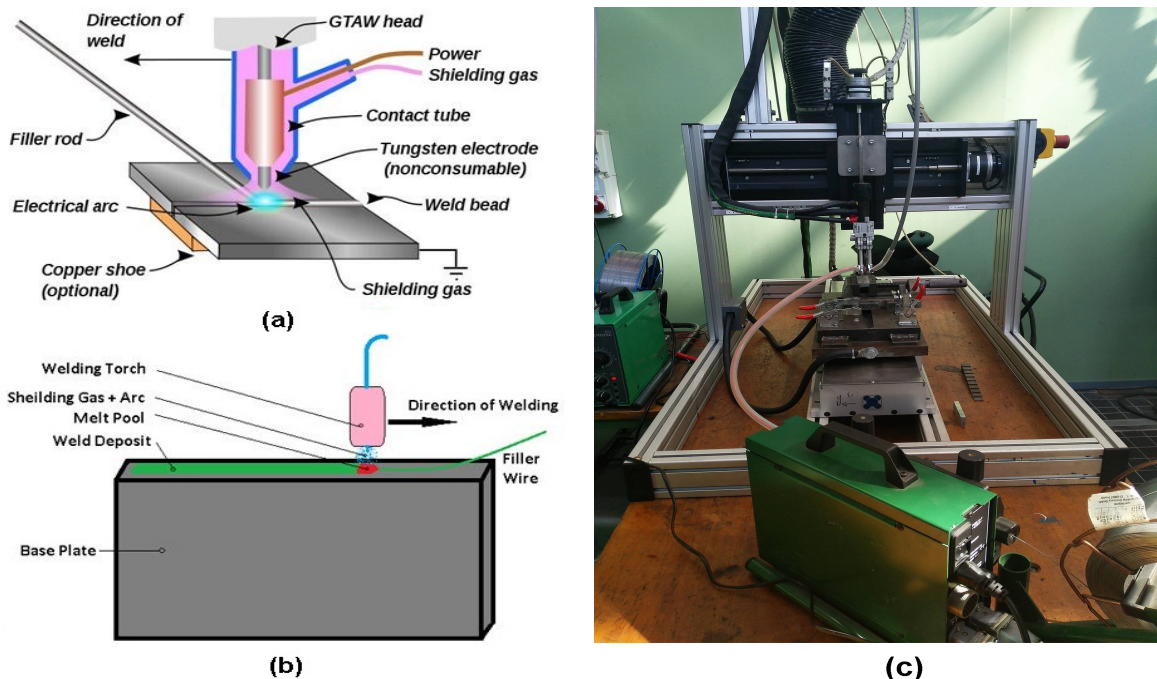
To study wire and arc based additive manufacturing (WAAM) of manganese aluminium bronze (MAB), MAB filler wire of 1mm diameter (SG CuMn13Al7, supplied by Certilas, NL) was deposited on a nickel aluminium bronze (NAB) substrates, 13 mm x 100 mm x 30 mm in dimension. To determine to composition of both the filler wire and the base plate, X-Ray Fluorescence (XRF) measurements were performed on specimens using Panalytical Axios Max WD-XRF spectrometer. The data hence obtained was analysed using SuperQ5.0i/Omnian software. The composition thus obtained has been tabulated in Table 1.

For deposition of the material, Gas Tungsten Arc Welding (GTAW or Tungstun Inert Gas, TIG) process was selected. As opposed to Gas Metal Arc Welding (GMAW or Metal Inert Gas, MIG) setup where the heat input is coupled with rate of mass deposition, TIG welding process

Table 1: Composition of MAB wire and NAB substrate determined by XRF analysis (wt %)

Material	Cu	Al	Ni	Fe	Mn	Zn	Si	Others
MAB	73.7	6.68	2.40	2.65	11.1	2.97	0.26	0.08
MAB dev	0.5	0.09	0.09	0.08	0.2	0.1	0.02	0.02
NAB	79.7	9.08	4.9	4.82	1.18	0.07	0.09	0.06
NAB dev	0.4	0.09	0.1	0.08	0.04	0.01	0.01	0.02

offers an additional flexibility where both these parameters can be controlled independently. Migatronc TIG commander 400 welding setup was used during all the experiments. The welding torch is attached to a CNC platform and is capable of motion along X, Y and Z direction. DMC terminal software is used to plan and define the trajectory of the torch. An arc is established between a nonconsumable tungsten electrode (2.4 mm diameter, 98.34% W, 1.5% La, 0.08% ZrO₂, 0.08% Y₃O₂, E3 purple) and the base material using a high frequency high voltage pulse. The power source is operated in constant current condition as it ensures a stable arc and hence a reproducible GTAW process [33]. Once a stable arc of arc length 2.5 mm is formed, in the local shielding environment of Argon gas (130 bar, 13 l/min), the filler wire (1 mm diameter) is fed into the arc and melt pool along the base plate. Hence the filler material is deposited on the 13 mm x 100 mm surface of the base plate in the form of a weld bead. This surface was chosen to ensure low deformation of the base plate as a result of warping due to welding. In an automated GTAW process, the rate of material deposition can be controlled via two parameters namely wire feed rate and travel speed of the torch. A schematic diagram of the GTAW setup and deposition process is shown in Figure 17.

**Figure 17:** Material deposition using GTAW (a) schematic of TIG welding [34] (b) schematic of the deposition process and (c) torch mounted on CNC stage along with wire feeder

3-3 Experiments

To study the influence of processing parameters on the evolution of microstructure during WAAM, single weld beads of MAB were deposited on top of NAB base plates as described in the previous section. Prior to deposition, the substrate was ground using 180GSM grit paper to remove oxides and was subsequently washed with ethanol. The base plates were not pre-heated before the deposition was carried out. The process parameters are tabulated in Table 2. The rate of material deposition was kept constant and the amount of heat input was varied using different welding currents. Material deposition rate was 0.75 kg/hr.

Table 2: GTAW process parameters for the parametric analysis experiments

S. No	Current (Amp)	Travel Speed (mm/s)	Feed Rate (mm/s)
1	100	3	36
2	125	3	36
3	150	3	36

Metallographic samples of cross-sectional surfaces of the NAB base plate, MAB filler wire and the deposited beads were prepared using standard procedure and were etched using a mixture of $FeCl_3$, HCl and H_2O (5:25:70). Keyence digital microscope was used to observe the macrostructure and microstructure. An in-built image processing software was used to quantify phase area fractions of different phases in optical micrographs. The microstructure was further examined using JSM IT-100 scanning electron microscope (SEM) equipped with tungsten hairpin filament as electron source, Everhart-Thornley secondary electron detector and Silicon drift energy dispersive spectroscopy (EDS) detector. Bruker D8 advance diffractometer with $Co\ K\alpha$ (1.789\AA) was used to identify phase constituents. X-ray Diffraction scans are performed from $2\theta = 25^\circ - 130^\circ$ with a step size of 0.035° and the data was evaluated using Bruker software Diffrac.EVA vs 4.2. The top surface of the weld bead was polished and analyzed in this method.

To investigate the influence of WAAM related complex thermal histories on the evolution of microstructure, a single wall of MAB was built. Six weld beads were deposited layer wise on top of one another unidirectionally. As a result, a 10.5 mm high wall was obtained. Process parameters for the deposition are tabulated in Table 3. k-type thermocouples were brought in contact with the deposit and the temperature of the top surface was monitored after deposition. The interpass temperature between subsequent deposition was kept below $200^\circ C$. Metallographic samples were prepared from the longitudinal and transverse cross-sections of the wall for characterization of the microstructure. Series of hardness measurements were recorded using Streurs DuraScan 70 device. A 0.5 HV ($0.5\text{kgf}/\text{mm}^2$) load was applied using a diamond indenter and the inter-indent spacing was defined to be $250\ \mu\text{m}$ (more than 4 times the diagonal of the indent).

Table 3: GTAW process parameters for the layer buildup analysis experiments

S. No	Current (Amp)	Travel Speed (mm/s)	Feed Rate (mm/s)
1	125	3	36

3-4 Results and Discussions

3-4-1 Raw Materials

Optical micrographs for the as received NAB rolled sheet and MAB filler wire can be seen in Figure 18. Both the materials have a dual phase microstructure where the α (FCC) and β (BCC) phases are the lighter and the darker phases respectively. Precipitate particles (presumably Fe rich) can be observed in the MAB microstructure. However for this thesis, the microstructure of the as-received wire is unimportant since it liquefies before deposition.

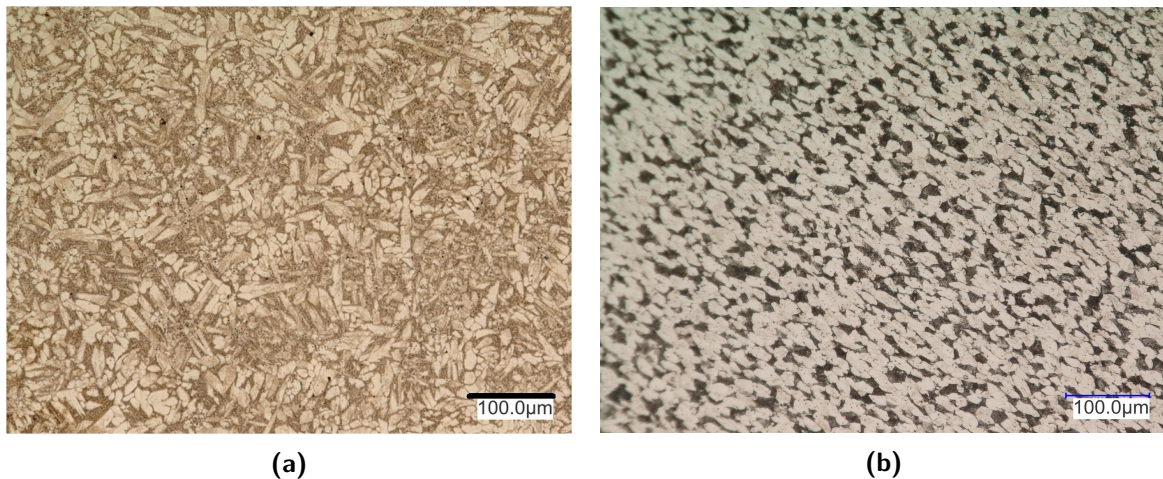


Figure 18: Light optical micrographs of (a) NAB cross-section and (b) MAB cross-section

3-4-2 Parameter study

Figure 19. shows optical macrographs of the weld beads corresponding to MAB100, MAB125 and MAB150, respectively, where numbers represent current level. Clear differences can be seen in the geometries of the cross-section with respect to the angle of contact and the amount of intermixing between MAB deposit and the NAB base plate. In case of higher heat input i.e. MAB150, there is significant intermixing between the filler material and base plate as opposed to MAB100. MAB100 has a higher angle of contact as compared to MAB150. Weld bead geometry and wetting of the base plate is a complex configuration, which is determined by nonequilibrium conditions at the solid liquid gas interface where forces like gravity, inertia, and surface tension play a major role along with thermal effects [35].

During the deposition process, the heat from the arc is consumed primarily for two purposes: for liquefying the filler wire and at the same time, for heating the base plate or melting a part of it. In case of higher heat input, a significant portion of heat goes into creating a wider and deeper melt pool in the base plate and corresponding shapes of the beads [20]. This is also apparent from the large heat affected zone.

The shape of the melt pool plays a role in the subsequent solidification and hence the microstructure. Solidification initiates perpendicular to the fusion line along the direction of maximum temperature gradient. Simultaneously, since the deposition is taking place in atmosphere of Ar gas, there is another thermal gradient perpendicular to the outer surface of

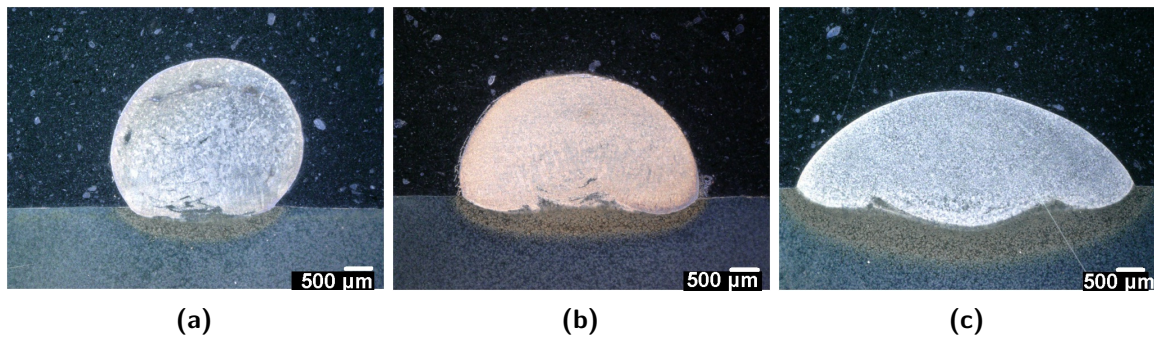


Figure 19: Macrographs of geometries of the deposit a)MAB100, (b) MAB125 and(c) MAB150. Clear difference in the surface wetting and contact angles can be seen.

the deposit. Hence there are two competing gradients, one of which causes primary grains to grow as columns from fusion line, another, which promotes heterogeneous nucleation of equiaxed β grains of Fe rich primary precipitates. This is shown schematically in Figure 20.

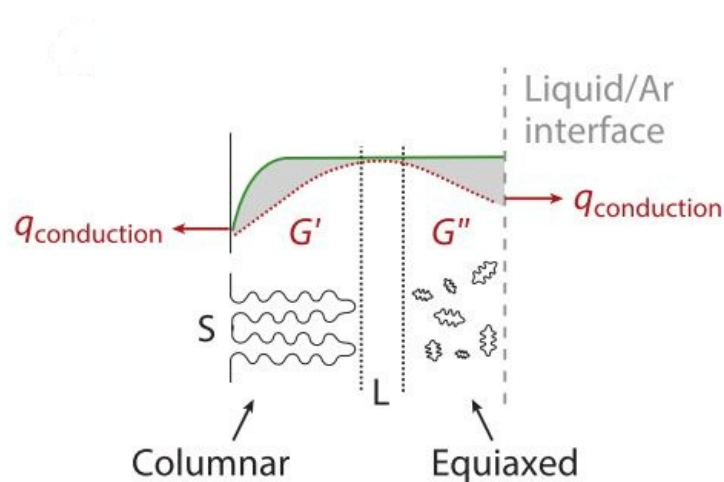


Figure 20: A schematic of primary grain growth during AM deposition in Ar atmosphere [24].

In Figure 21, the microstructure corresponding to MAB100 and MAB150 can be seen at various magnifications. Etching has resulted in dark and light grains where darker grains correspond to the retained β phase and the lighter grains correspond to the α phase. Presence of grain boundary α clearly outlines prior β grain boundaries, that were formed initially upon solidification from the liquid phase. In Figure 21, (a) and (b) it can be seen that near the deposit-base plate interface, columnar prior β grains are formed and further up in the deposit, the prior β grains are equiaxed. However, in case of MAB150, the columnar grains near the interface are suppressed and greater numbers of equiaxed grains are formed. In case of MAB100, due to low heat input, there is a steep temperature gradient across the fusion line. Hence, columnar grains β grains grow which are otherwise suppressed in MAB150 (a predominantly equiaxed β grains microstructure). Based on grain boundary α , some prior beta grain boundaries are highlighted in 21 (a) and (b). Similar results have been reported by Wang et al. [4] for TiAl6V4.

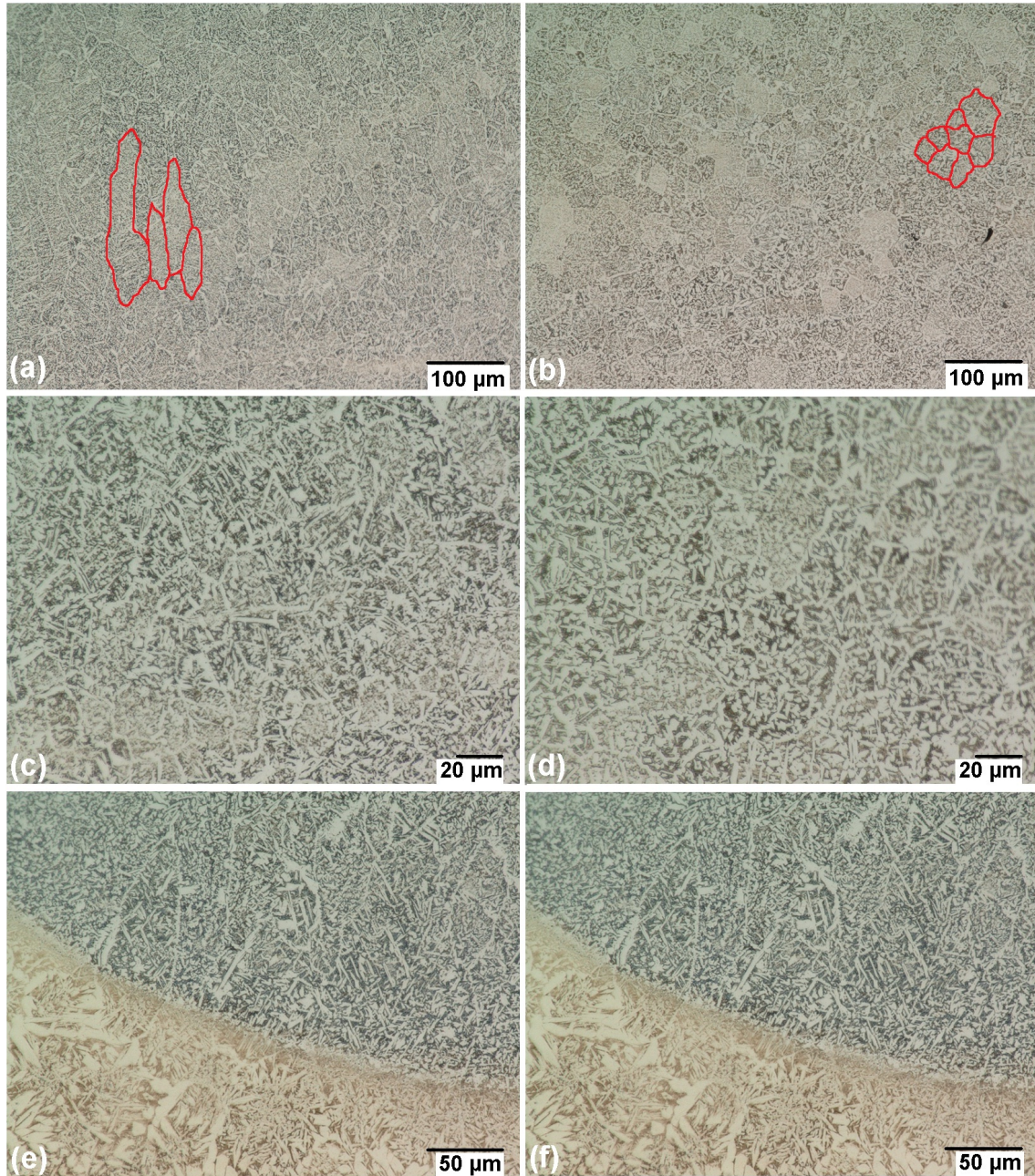


Figure 21: Light optical micrographs of single weld deposits. (a) MAB100 low magnification (b) MAB150 low magnification (c) MAB100 high magnification (d) MAB150 high magnification (e) MAB100 interface and (f) MAB150 interface. Differences in morphology of prior β and α grains with respect to heat input can be observed

As the temperature is lowered, β to α phase transformation takes place. In Figures 21 (c) and (d) the optical micrographs of MAB100 and MAB150 can be seen at high magnification. As mentioned previously, the grain boundary α can be clearly observed along the prior β grain boundary. Acicular α grains are observed within β grains. In addition to that, Widmanstätten α morphology can also be seen growing towards the center of the grain from the prior β grain boundaries. Such a morphology has been observed in the literature for solid state phase transformations corresponding to wire and arc additive manufacturing [4, 36]. The mechanism of nucleation and growth of Widmanstätten grains is beyond the scope of this work. However, it can be seen that MAB100 has fine Widmanstätten and grain boundary α , while MAB150 has coarse α grains. Differences in cooling rates can potentially explain the observations.

Figures 21 (e) and (f) show the fusion zone and the heat affected zone of the NAB base plate in case of MAB100 and MAB150, respectively. A nearly $10\ \mu\text{m}$ layer consists of the interface that has undergone remelting followed by rapid solidification. This has resulted in a predominantly β phase zone. The adjacent β rich zone with fine α grains can be attributed as the heat affected zone (HAZ), which was heated beyond the β - α transformation temperature. It can also be seen that the width of the HAZ in case of MAB100 is less than $50\ \mu\text{m}$ whereas for MAB150, the width of HAZ is more than $100\ \mu\text{m}$. The higher heat input in MAB150 can explain the observations.

In order to quantify the amount of phases, proprietary image processing software from Keyence digital microscope was used. Two different regions at same magnification for each specimen were analysed. Figures 22 (a) and (b) show the post processed binary images. Area fractions of the α and β phases has been tabulated in Table 4. The amount of κ phases has been ignored in this method and hence only semi-quantitative phase fractions can be obtained. Due to the presence of continuously connected grains along the boundaries, no meaningful data on grain sizes and circularity of the grains can be obtained. It was observed that there are insignificant changes in the phase fractions due to the range of heat inputs provided, however morphologies are different.

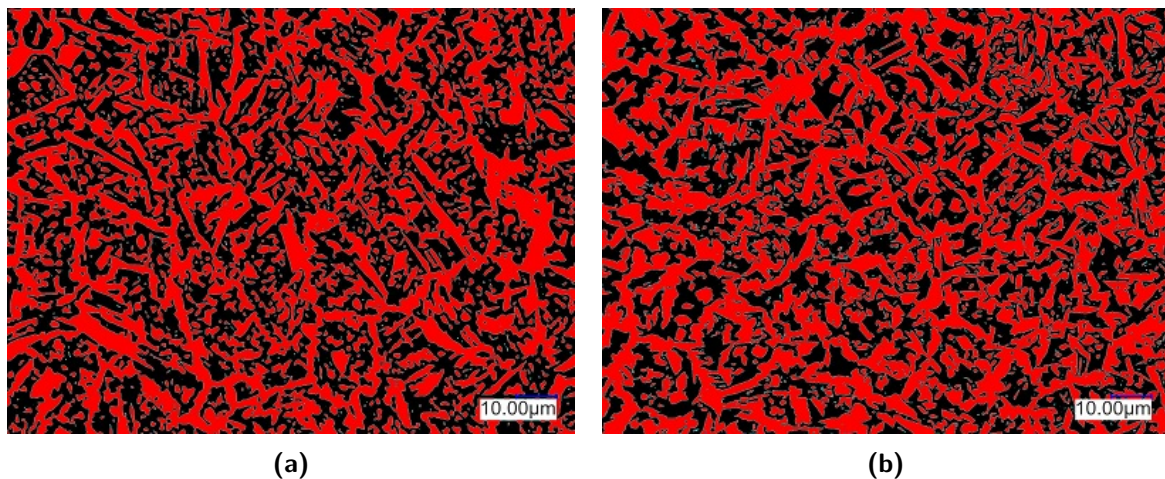
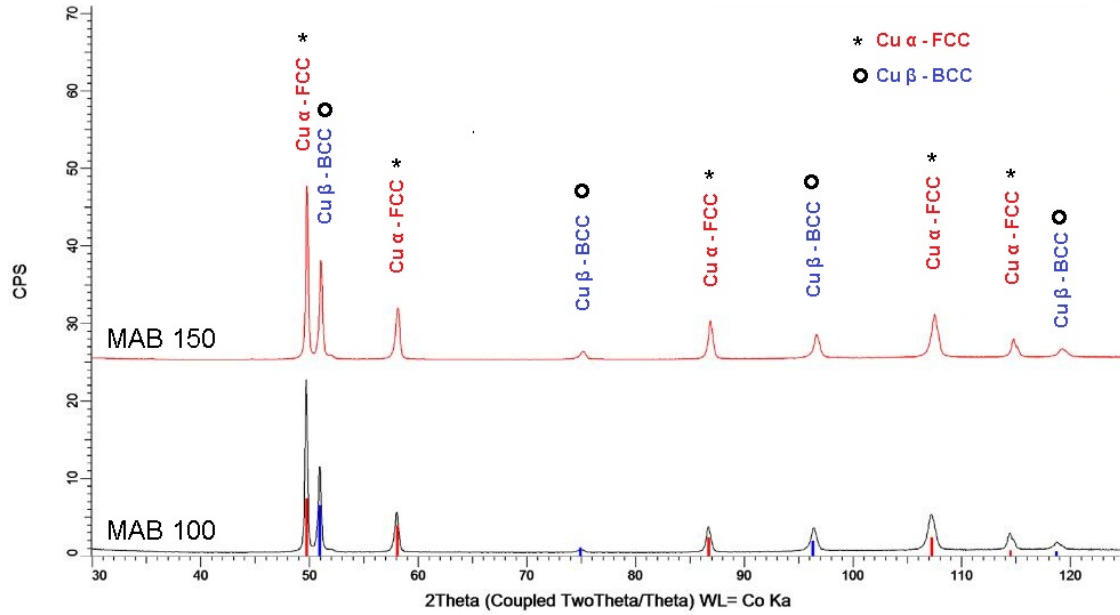


Figure 22: Post processed binary micrographs for (a) MAB100 and (b) MAB150. The red regions correspond to α grains in the respective microstructures

Table 4: Area fraction of α and β phases (in %) in the MAB deposits

Material, Phases	α Phase (%)	β Phase (%)
MAB100	55.92	44.08
	52.21	47.79
MAB150	55.46	44.54
	56.88	43.12

**Figure 23:** XRD patterns of MAB100 and MAB150 are represented in black and red respectively. According to the database, standard peaks corresponding to Cu-FCC and Cu-BCC are shown in red and blue respectively along the x-axis

XRD patterns of MAB100 and MAB150 can be seen in black and red respectively in Figure 23. Counts per second (CPS) are recorded on the y-axis against the 2 theta angles (indicative of the d-spacing) along the x-axis. Peaks corresponding to Cu- FCC and Cu- BCC are also indicated [11]. It is evident that both the phases are present in the materials. A comparison of peak heights for the two phases did not reveal any coherent trend indicating that the differences in the phase fractions in two different configurations are not significant. This further supports the data from image processing of optical micrographs.

Scanning electron micrographs of a typical dual phase deposit can be seen in Figure 24. α , β and κ phases have been indicated. Retained β phase is preferentially etched and hence can be differentiated easily. Globular sub-micron precipitates can also be seen in the micrographs. To understand the nature of these precipitates and the dominant phases, EDS elemental maps were constructed. The color bars next to the elemental maps depict the relation between the color and its relative presence within the corresponding map. The ranges of color bars for different elements are unrelated to each other and hence, no quantitative data can be gathered from these maps. This holds for all EDS elemental maps discussed in this thesis. It can be seen that the β phase is richer primarily in aluminium and small amounts of

manganese and nickel are also observed. Additionally, Fe rich precipitates have also been detected in the microstructure. These results are coherent with the existing literature on the composition of phases [15]. Point wise analysis is not an effective tool to determine the precise composition of precipitates as the size of the interaction volume of electrons (given as $x\mu\text{m}=0.1 * E_o^{1.5} \text{KeV}/\rho g/\text{cm}^3$, Potts et al [37]), $1.12 \mu\text{m}$ is larger than the size of the sub-micron precipitates formed in the studied microstructures.

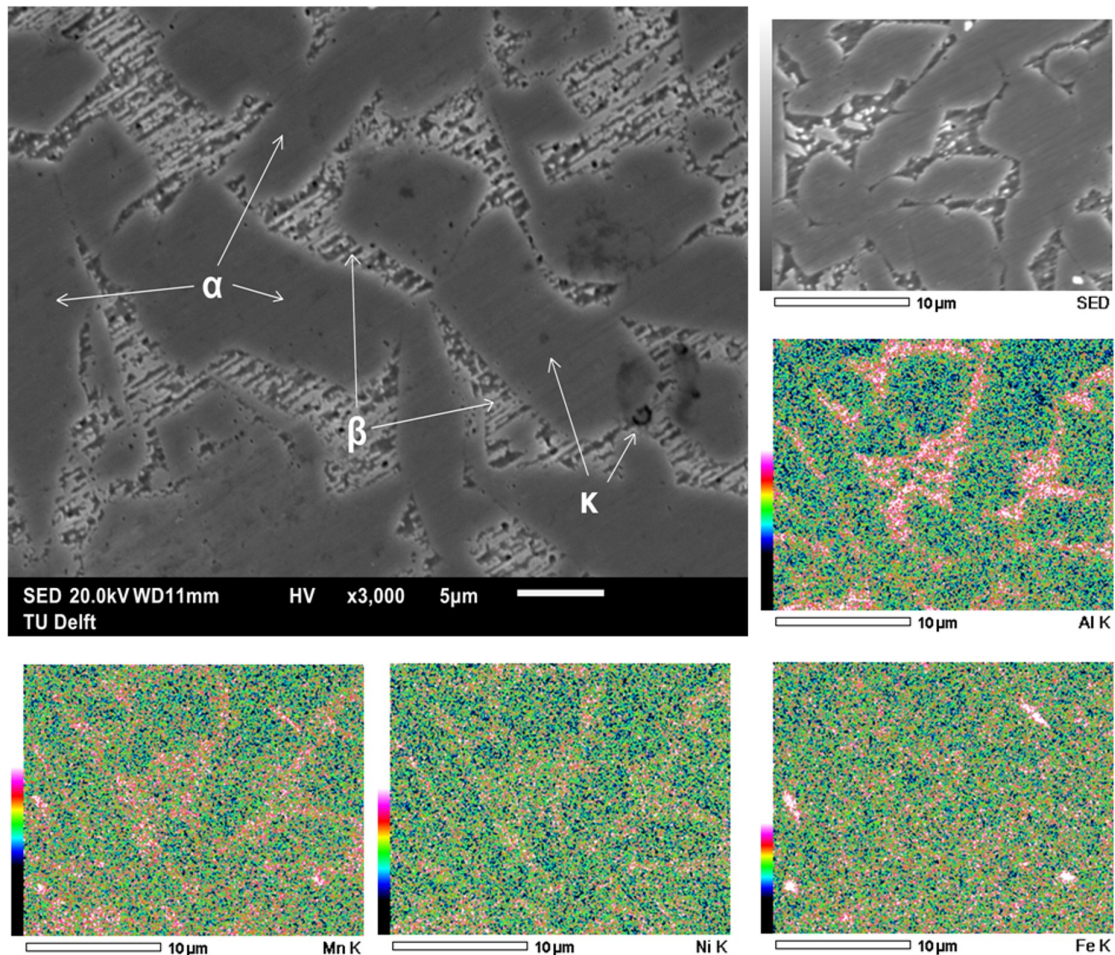


Figure 24: Scanning electron micrographs and EDS elemental maps. (a) Dual phase electron micrograph with phases indicated (b) electron graph for EDS and spatial distribution of (c) aluminium, (d) manganese, (e) nickel and (f) iron

3-4-3 Layer deposition study

Figure 25 shows the macrostructure of a transverse cross-section of 6 layers of MAB deposited on top of one another. The banded macrograph has been widely reported in literature concerning wire and arc additive manufacturing [4, 11]. There are 6 of these bands including the interface between MAB and NAB, corresponding to each of the deposit. No porosity or inclusions were observed along the cross-section. The distance between these bands is 1 mm as opposed to 3 mm for the height of an individual deposit because each deposition involves

remelting of a part of the previous deposit. This ensures bonding between subsequent layers. The bands are the interfaces and heat affected zones between the consecutive layers caused by remelting and sub melting-point reheating as suggested by Liu et al. [38]. The microstructure in the specific cross-section can be characterized as dual phase bands with different α and β phase fractions. Both coarse and fine α morphologies are observed.



Figure 25: Macrostructure of cross-section of 6-layer deposits on NAB base plate. Characteristic WAAM based layer microstructure bands are observed.

Figure 26 (a) shows a low magnification representative optical micrograph consisting of the above mentioned different bands. Based on the location of the grain boundary α , a combination of equiaxed and columnar prior β morphologies are observed. Wang et al. reported similar observations for AM of TiAl6V4 [4]. It is suggested that, equiaxed grains in a deposit serve as the nucleating points of columnar grains during the next deposition. Hence, columnar to equiaxed transitions are observed in layers. Figures 26 (b),(c) and(d) shows high magnification images of selected regions. Figure 26 (b) can be characterized as the as deposited fine Widmanstätten morphology for α grains. Such a microstructure is obtained for high cooling rates comparable to microstructure of MAB100. Figure 26 (c) consists of fine needle like α grains originating from rapid solidification after reaching a temperature above the α - β transformation temperature. Figure 26 (d) shows coarse α grains which can be thought of as Heat Affected Zone (HAZ) of the next deposit. Heating below the α - β transformation temperature due to subsequent depositions contributes to the coarsening of the α grains. The location and formation of differing morphologies within WAAM based structures can be attributed to complex local thermal histories that arise during processing. Computational thermal modelling of the process can offer insights into the final microstructures.

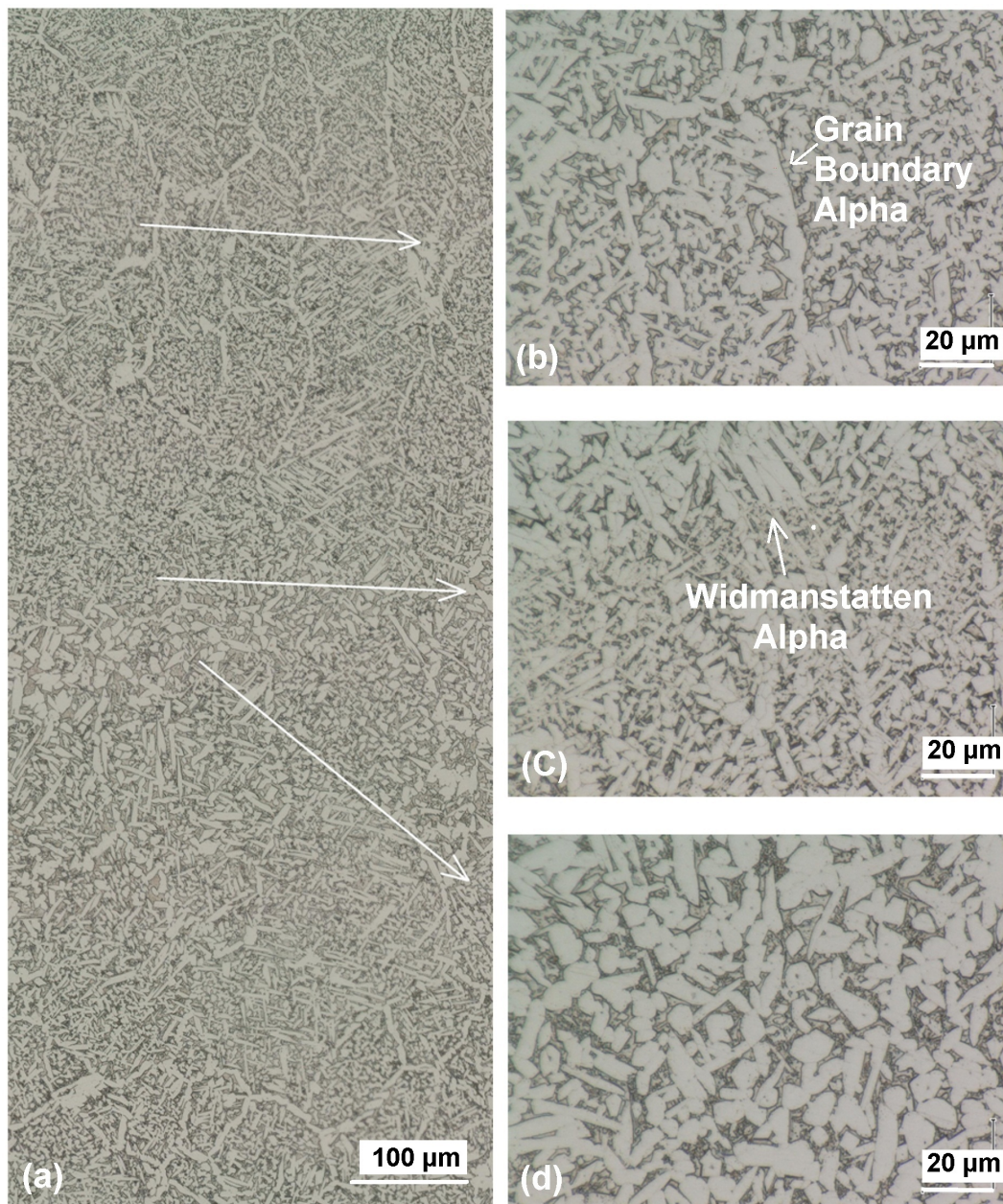


Figure 26: Optical micrographs of longitudinal cross-section of WAAM processed single wall of MAB (a) Overview of multiple layers and selected regions (b) Fine Widmanstätten and GB α , (c) re-molten zone with α needles and (d) coarse Widmanstätten and GB α

The results of the hardness measurements can be seen in Figure 27. The Vickers hardness is plotted along the y axis and the location of the indent is plotted along the x axis starting from base plate to the top of the wall. Corresponding regions are also depicted in the plot. Error bars show variations resulting from 3 different series as can be seen in the low magnification cross-section in Figure 27 ((a)). Exceptional high hardness values corresponding to indent locations 3 and 4 are due to intermixing between filler and base plate, rapid solidification and the presence of fine needle like α grains in the heat affected zones near the interface of the first deposit and the base plate. The other indents along the height of the wall have a hardness in between 220HV and 230HV. No repetitive trend in the fluctuations is observed since the bands of different morphologies are narrow ($<50 \mu\text{m}$) as opposed to the inter-indent spacings of $250 \mu\text{m}$.

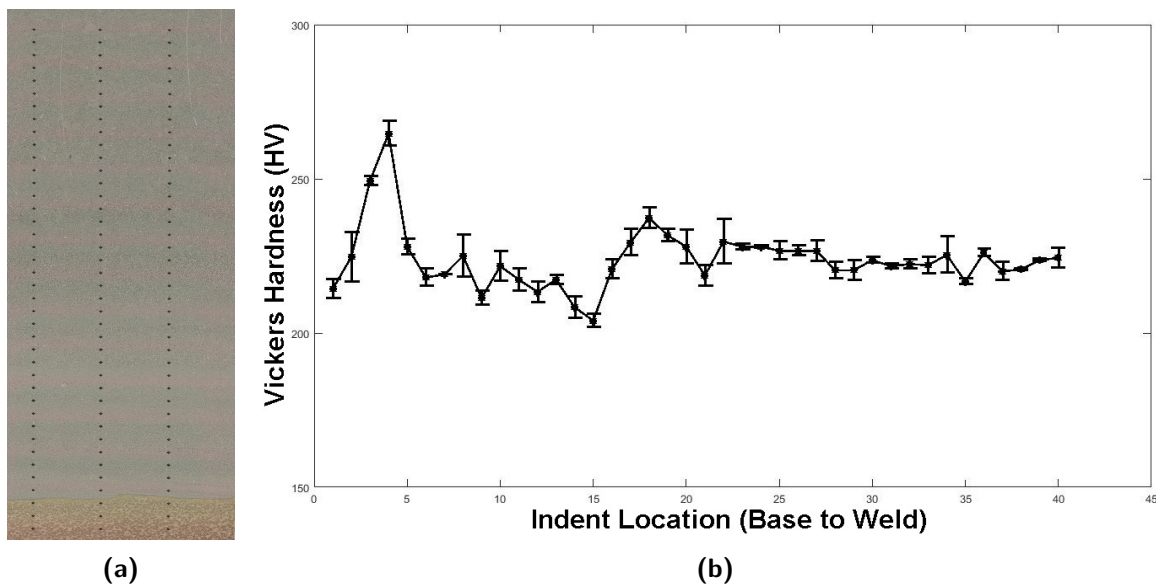


Figure 27: Series measurement of hardness of single wall (a) Optical Micrograph and (b) plot of vickers hardness versus the location of the indent from base plate to wall (left to right)

3-5 Conclusions

The potential of fabricating structural components using wire and arc additive manufacturing of manganese aluminium bronze has been demonstrated. The evolution of microstructure during WAAM processing and its dependence on process parameters has been investigated. Further layer-wise deposition resulted in defect free single walls. The following conclusions can be drawn-

- Non equilibrium solidification during WAAM results in a dual phase microstructure consisting of an α , Cu- FCC and an Al, Mn and Ni rich β , Cu-BCC phase. Fe rich precipitates are also found.
- The macrostructure for low energy input comprises of epitaxial and equiaxed prior β grains whereas high energy input results in predominantly equiaxed prior β grains

- The microstructure comprises of retained β , Grain Boundary α and Widmanstätten α . High energy input results in coarse α morphologies as opposed to fine ones during low heat inputs.
- Layer wise single wall deposition of MAB results in bands of coarse and fine dual phase microstructure consisting of deposits, heat affected zones and interfaces
- Hardness of the deposited wall structure is $222\text{HV} \pm 8.6\text{HV}$ which is comparable to the conventional NAB wrought alloy

The processing parameters corresponding to 150 A offer wetting of the base plate, ensures good bonding with previous layer and results in an equiaxed fine microstructure. These parameters will be used for further studies in the thesis.

In-situ Alloying

4-1 Introduction

Aluminium bronzes and particularly manganese and nickel aluminium bronzes are extensively used in marine environments for applications such as propellers, pipelines and valves[1]. This is because they offer good mechanical and excellent resistance to corrosion in seawater. The commercial alloys in their as-cast state or WAAM as deposited condition have a dual phase microstructure and hence they have complex heterogeneous distribution of elements within the phases as described in section 3.4. This however has limited their application due to their susceptibility to selective phase corrosion.

Tanabe reported that α aluminium bronzes ($\text{Al} < \sim 6\%$) have high resistance to selective phase corrosion (de-aluminification). Presence of other phases (β and κ) increases de-aluminification [39].

In the following chapter , in-situ alloying of MAB deposit with Cu3Si filler wire during deposition was explored with the aim to reduce Al wt% below $\sim 6\%$. A compositionally graded deposit was characterized to find optimum alloying parameters for a single phase α deposit. Non-equilibrium solidification microstructure of the new α phase alloy during WAAM processing was investigated further.

4-2 Experiments

A conventional GTAW setup as described in section 3-2, was used in the following experiments. To study the evolution of non-equilibrium solidification microstructure as we lower the amount of aluminium, in-situ alloying was performed using copper rich Cu3Si wire. Composition of the wire was measured using a Panalytical Axios Max WD-XRF spectrometer. The results have been tabulated in Table 5 below.

On an already deposited single weld bead of manganese aluminium bronze as described in Chapter 3, a single bead of Cu3Si filler wire was deposited. This resulted in re-melting of a

Table 5: Elemental Composition of Cu3Si filler wire determined by XRF analysis (wt%)

Material	Cu	Si	Mn	Cl	Al	Zn	Mg	Others
Cu3Si	93.9	3.12	0.99	0.7	0.31	0.17	0.23	0.44
Cu3Si dev	0.5	0.05	0.04	0.03	0.02	0.1	0.01	0.07

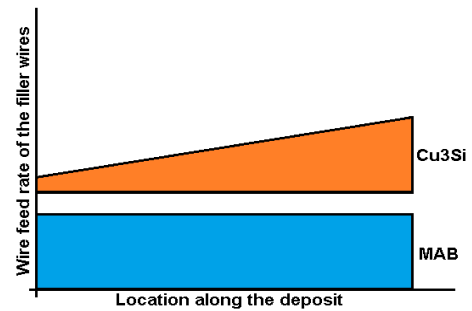
part of MAB deposit along with the Cu3Si filler wire and thereby alloying within the melt pool. Process parameters were chosen so as to ensure full remelting of only the previous bead and not of the base plate. Wire feed rate for the process parameter selection experiments was chosen based on trials and qualitative estimates from phase diagram and mass balance calculations. The corresponding details can be found in Appendix B.

4-2-1 Compositionally Graded Deposition

During the in-situ alloying experiment, the wire feed rate of Cu3Si was increased progressively along the bead to obtain a single weld deposit with incremental amounts of copper in the composition of the melt pool along the deposit. Process parameters for the experiment along with a schematic diagram of the experiment are shown in 28.

Material	Current (Amp)	Travel Speed (mm/s)	Feed Rate (mm/s)
1/MAB	150	3	36
2/Cu3Si	150	3	6 - 36 (ramp)

(a)



(b)

Figure 28: Deposition process parameters for in-situ alloying. Schematic diagram of wire feed rate qualitatively indicating the local composition of the melt pool

The longitudinal cross section of the deposit was polished using standard metallographic procedures and etched using a mixture of $FeCl_3$, HCl and H_2O (5:25:70). Keyence digital microscope was used to stitch the macrostructure of the compositionally graded deposit. Optical micrographs of selected regions in the deposit were recorded. Series of hardness measurements were recorded using a Streurs DuraScan 70 device. A 1 kgf/mm^2 load was applied using a diamond indenter and the inter-indent spacings was defined to be 4 mm (more than 4 times the diagonal of the indent). A section of the deposit was further analyzed at distinct points along its length with scanning electron microscopy and energy dispersive x-ray analysis using a Jeol JSM-IT100. Image processing in MATLAB was used to observe trends in phase fractions.

4-2-2 Optimal Alloying

Based on the results of the experiment described above, optimal alloying composition and hence the process parameters were identified in order to form a single phase homogeneous non-equilibrium microstructure. The parameters are tabulated in Table 6. A Cu3Si single weld bead was deposited on a MAB deposit causing its remelting and hence alloying. Metallographic samples of the longitudinal and transverse cross sections were prepared. The microstructure was characterized using optical microscopy, scanning electron microscopy and X-Ray diffraction analysis. The top surface of the weld bead was analyzed in this method.

Table 6: Process parameters for optimal in-situ alloying

S. No/ Material	Current (Amp)	Travel Speed (<i>mm/s</i>)	Feed Rate(<i>mm/s</i>)
1/MAB	150	3	36
2/Cu3Si	150	3	21

4-2-3 Solidification Analysis

To gain insights into stability of phases at elevated temperatures and to study the solidification behaviour of the new alloy, alloy samples were heated in an Nabertherm box furnace at different elevated temperatures and subsequently quenched in water. The heat treatment parameters are tabulated below in Table 7. Microstructure was characterized using optical microscopy, electron microscopy and X-ray diffraction analysis. Similar experiments were conducted for MAB as well. The results can be found in Appendix A

Table 7: Heat treatment parameters for solidification analysis of MABCu

Temperature (°C)	Time (hrs)	Cooling
650°C	2.5	Water Quench
750°C	2.5	Water Quench
850°C	2.5	Water Quench
950°C	2.5	Water Quench

4-3 Results and Discussions

Aluminium bronzes can be characterized into single phase α bronzes and dual phase α - β bronzes based on the percentage of aluminium present [40]. A Copper-aluminium phase diagram constructed using ThermoCalc 16a, SSOL2 : SGTE Alloy solutions database is shown in Figure 29. It can be seen that at elevated temperature, the phase diagram has three characteristically different regions, namely $L+\alpha$, $L+\alpha+\beta$, and $L+\beta$ regions. Due to the presence of different alloying elements, various regions/phases in the phase diagram shift and move along the temperature-composition plane[13].

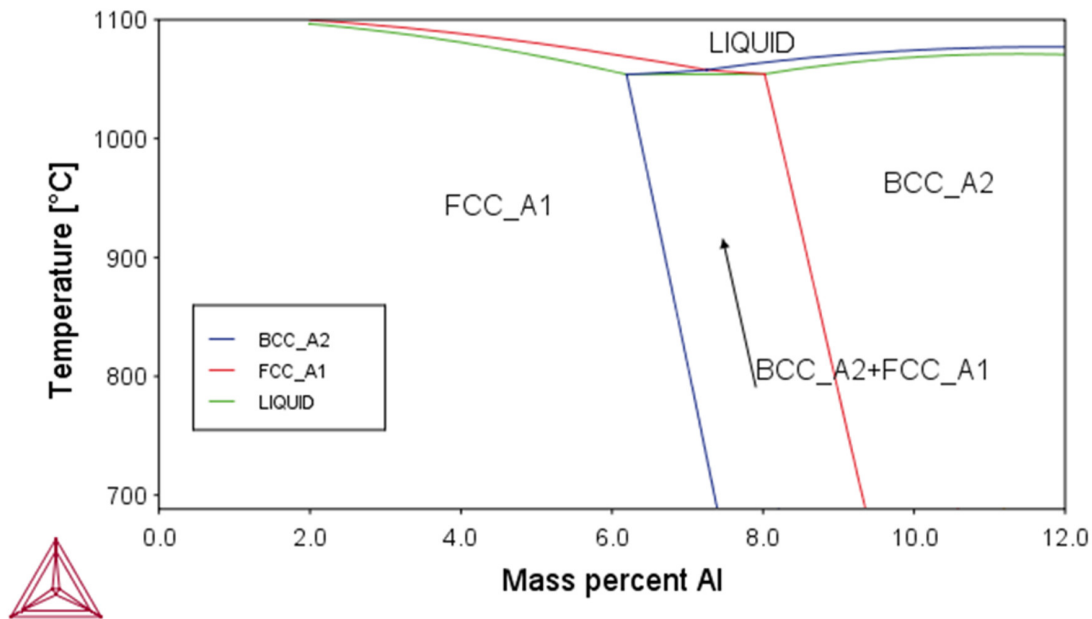


Figure 29: A section of Cu-Al binary phase diagram

4-3-1 Compositionally Graded Deposit

During the experiment described in section 4-2, as the percentage of aluminium decreases, the composition of melt pool changes from the $L+\beta$ region to the $L+\alpha$ region via the $L+\alpha+\beta$ region. A low magnification stitch of the macrograph can be seen in Figure 30 (a). Optical micrographs from selected sections of the compositionally graded deposit can be seen in Figure 30 (b), (c) and (d). Macro and Micro lenses were used in the digital microscope for respective images. As a result of combination of etching and lighting of the corresponding lens, in Figure 30 (a), the lighter phase dominant in the left corner is the β phase, whereas the dark regions towards the right of the macrograph correspond to the α phase. On the other hand, in micrographs (b), and (c) dark regions are β phase and the lighter regions are α .

It can be evidently observed in the macrograph that the microstructure changes from a dual phase to a cellular dendritic single phase. Three characteristically different regions can be identified, as can be seen in the micrographs in Figure 30. The continuous dual phase (CDP) microstructure in Figure 30 (b) consists of grain boundary α and Widmanstatten α grains in prior β grains. The above mentioned microstructure corresponds to a melt pool composition lying in the liquid+ β region of the Cu-Al phase diagram. This has been discussed in greater detail in Chapter 3 of this thesis.

Optical micrograph in Figure 30 (c) has a discontinuous dual phase (DDP) microstructure. The local composition corresponds to the liquid+ $\alpha+\beta$ region in the phase diagram. It can be seen that the non-equilibrium solidification microstructure at room temperature comprises of small β grains along the edges and at the corners of relatively larger α grains. κ phase precipitates can also be observed in both the phases. The mechanism of solidification in non-equilibrium conditions for DDP alloys is beyond the scope of this work.

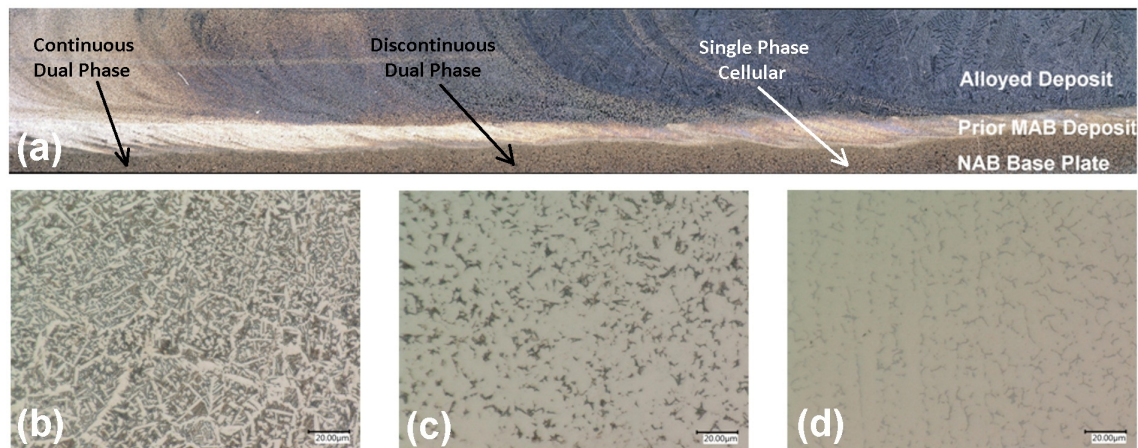


Figure 30: A section of in-situ alloyed compositionally graded deposit (a) macrograph of a section showing transition from dual phase to single phase microstructure (b) a continuous $\alpha + \beta$ microstructure (c) a discontinuous $\alpha + \beta$ microstructure and (d) single phase α microstructure

Figure 30 (d) can be identified as single phase cellular (SPC) microstructure with a composition corresponding to the Liquid+ α region in the Cu-Al phase diagram. Sets of around 10 μm wide parallel cellular dendrites can be observed along the direction of thermal gradient. This single phase microstructure will be discussed in greater detail in the following section. Scanning electron micrographs along with corresponding elemental maps for the three characteristically different microstructures, namely continuous $\alpha + \beta$, discontinuous $\alpha + \beta$ and single phase cellular α can be seen in Figure 31-33.

Etching has caused the β phase to be preferentially corroded and hence the grains in the form of pits correspond to β phase in Figure 31 and 32. This β phase is rich in aluminium and manganese as seen from elemental maps which is also reported in literature [13]. In Figure 33 aluminium is homogeneously distributed in α matrix as the corresponding composition lies within the solubility limit. In Figure 33, manganese on the other hand combines with the increasing amount of silicon along with nickel and iron to form precipitates. Upon close observations, two kinds of precipitates, one rich in Fe, Mn and Si and another rich in Fe, Ni, Mn and Si can be seen. These precipitates are individually indicated in Figure 33 Fe map and Ni map respectively. Fe and Si rich precipitates, similar to the ones mentioned above can also be seen in the DDP microstructure (Figure 32).

Figure 34 (a) summarizes the trends in concentrations of various alloying elements along the deposit. EDS was used to extract local compositions at discrete points along the deposit. Upon increasing addition of Cu3Si filler wire in MAB deposit, the concentration of Si in the deposit increases whereas the composition of aluminium, manganese, iron and nickel decreases. However, it can be observed that the trends are not linear. This is because, for a given amount of heat input, the amount of re-molten MAB decreases upon increasing additions of Cu3Si. Additionally, the temperature of the base plate during deposition is not constant, adding to the nonlinearity in compositional trends.

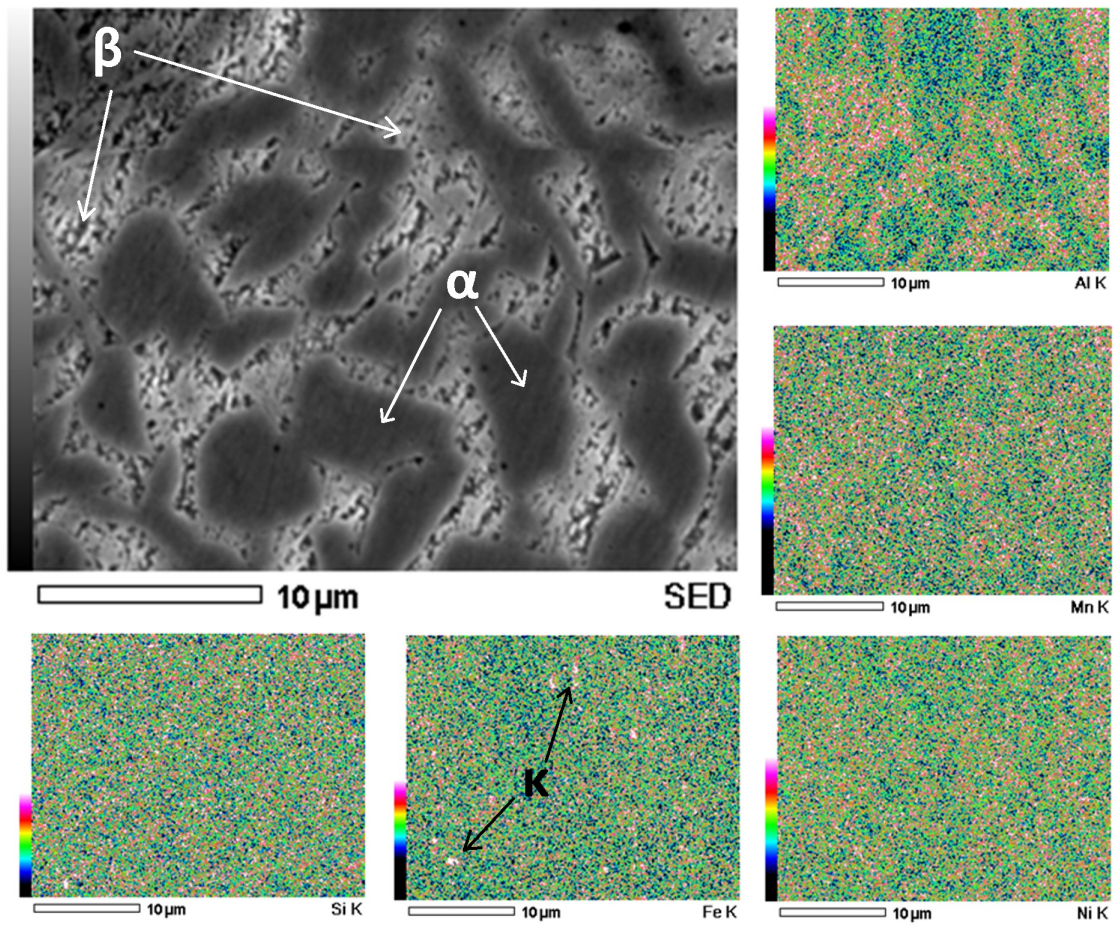


Figure 31: Scanning electron micrographs and elemental maps Continuous Dual Phase (CDP) microstructure

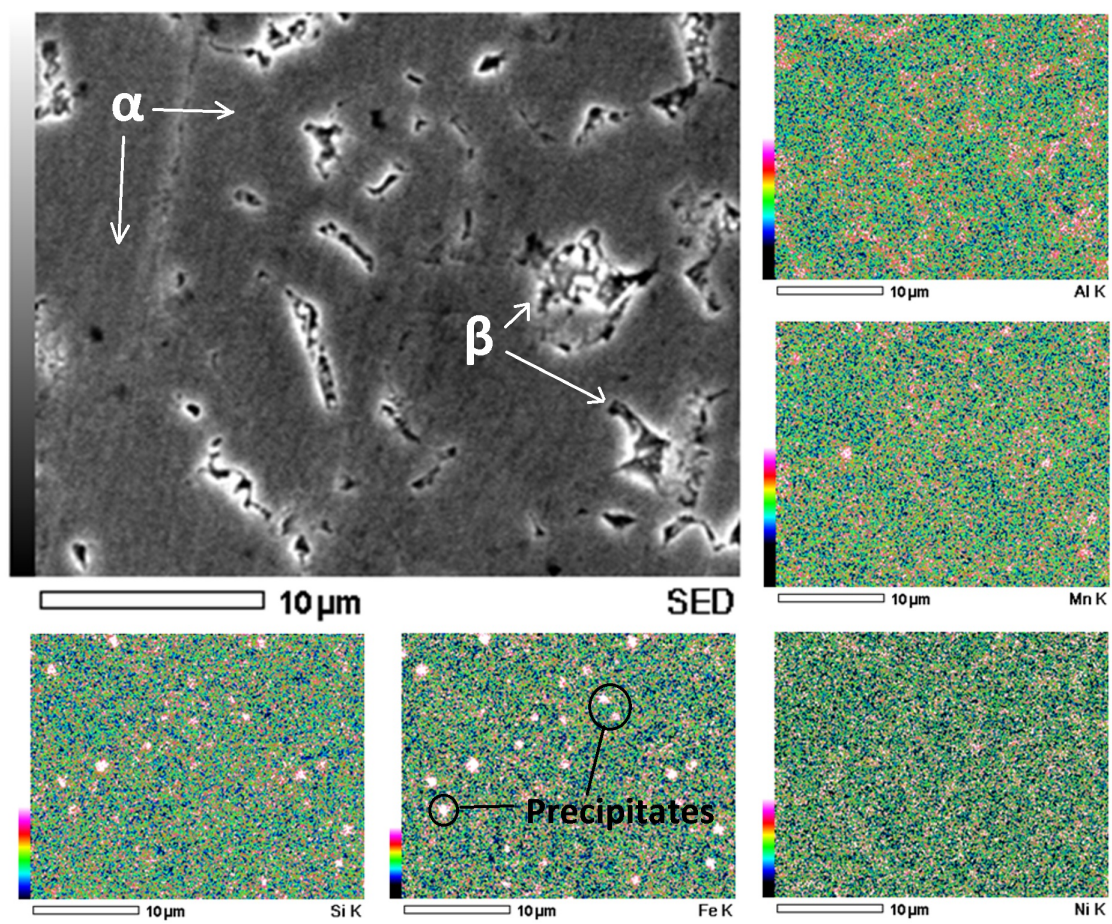


Figure 32: Scanning electron micrographs and elemental maps Discontinuous Dual Phase (DDP) microstructure

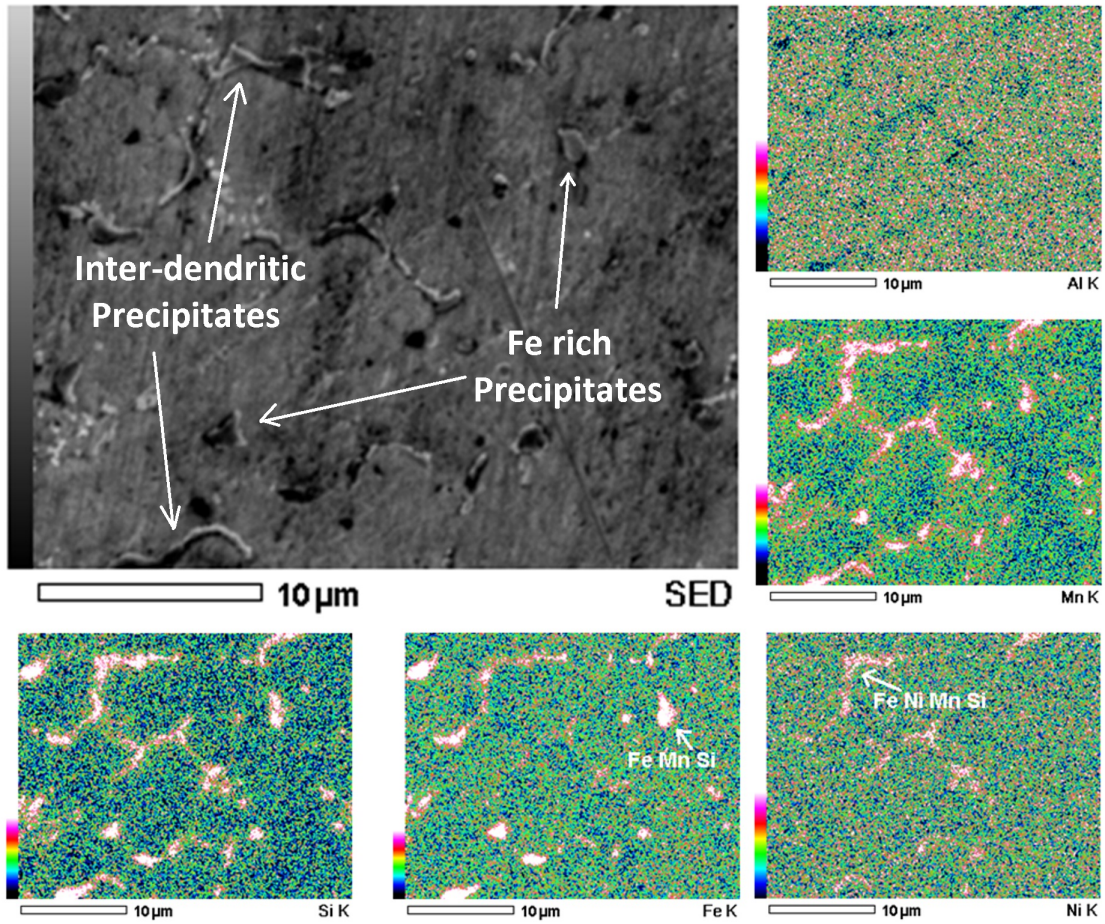


Figure 33: Scanning electron micrographs and elemental maps Single Phase Columnar (SPC) microstructure

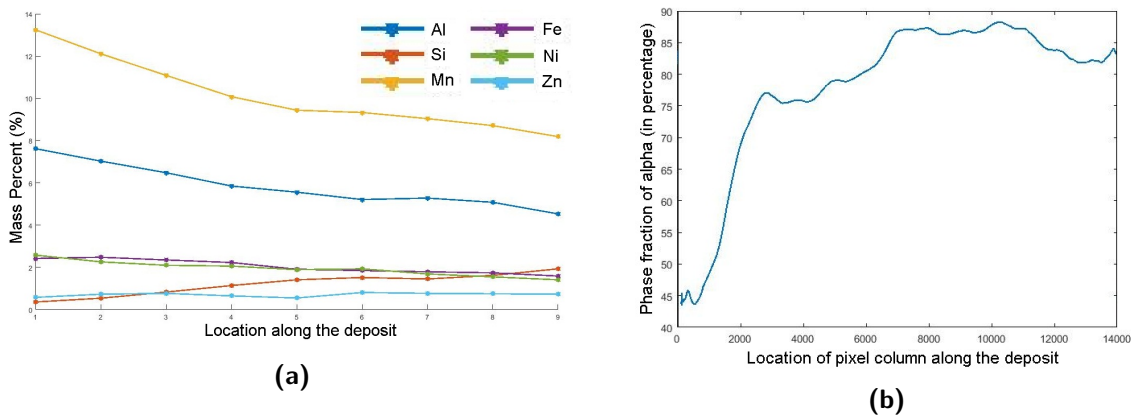


Figure 34: a) Trends in composition of alloying elements in the deposit (b) Phase fraction of α phase along the length of the deposit

The microstructure changes progressively from dual phase to single phase. Image processing (MATLAB) was used to quantify phase fractions along the deposit, shown in Figure 52 (a). The image was binarized with dark pixels corresponding to α and white pixels being β phase and the inter cellular regions. Figure 34 (b) shows the trend in α phase obtained. The absolute values of phase fractions are not accurate because of the resolution and lens lighting during acquisition, but a clear trend is visible. A curve starts with a phase fraction plateau in the CDP region, sharply reduces along the DDP region and subsequently reaches another plateau in the SPC region. This trend is coherent with the Cu-Al binary phase diagram as there is a fixed discrete value of aluminium concentration below which the microstructure is single phase irrespective of the composition.

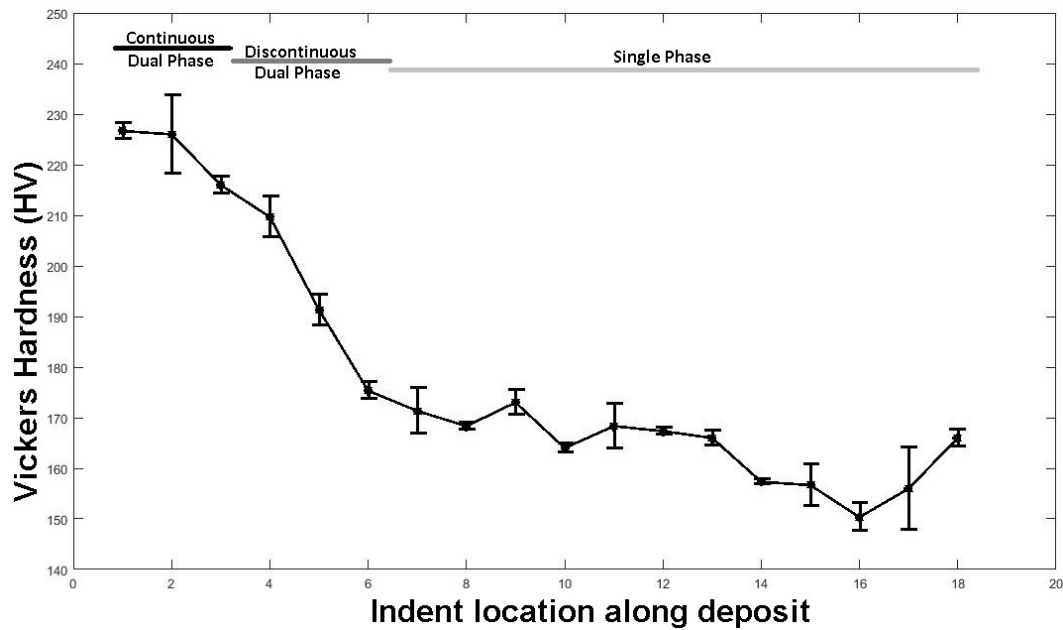


Figure 35: Trends in hardness values along the length of the deposit.

Figure 35 shows the trend in hardness along the deposit. Error bars correspond to the standard deviation from 3 series of measurements. The graduated bar on the top differentiates the three microstructural regions namely CDP, DDP and SPC. It was observed that there is a significant difference between as-deposited CDP microstructure ($\sim 225\text{HV}$) and the newly developed SPC microstructure ($\sim 165\text{HV}$). There is a sharp drop in the hardness values in DDP region. Thereafter the drop is more gradual in the SPC region. This can be explained as an outcome of different strengthening mechanisms associated with different microstructural regions. In the CDP region, the phase fractions of hard (beta) and soft (alpha) phases are similar and hence similar hardness values are found. However, in the DDP region as the phase volume fractions of the β phase drops (as seen in Figure. 34 (b) there is a sharp decline in hardness indicating that primary strengthening mechanism is presence of hard phases. In the SPC region on the other hand, strengthening mechanisms at work are solid solutions strengthening (aluminium and manganese content)[41] and precipitation hardening (discussed in this section). Hence, based on the results of the above experiments, parameters corresponding to solid solution and precipitation strengthened single phase alloy were optimally chosen. The material obtained with optimal parameters has been characterized in the section below.

4-3-2 Alloy Analysis

A single bead deposit of Cu3Si wire was deposited using 150 A at a wire feed rate of 21 *mm/s* (Table 6) on an existing MAB deposit (150 A; 36 *mm/s*) while ensuring remelting and remixing of the two deposits (will be referred to as MABCu). The composition of the deposit measured using a Panalytical Axios Max WD-XRF spectrometer is tabulated in Table 8 Figure 36 shows optical micrographs at different scales.

Table 8: Elemental composition of MABCu deposit determined by XRF analysis (wt%)

Material	Cu	Mn	Al	Ni	Fe	Si
MABCu	84.6	5.9	4.9	1.7	1.6	1.3
Dev.	0.9	0.2	0.1	0.1	0.1	0.1

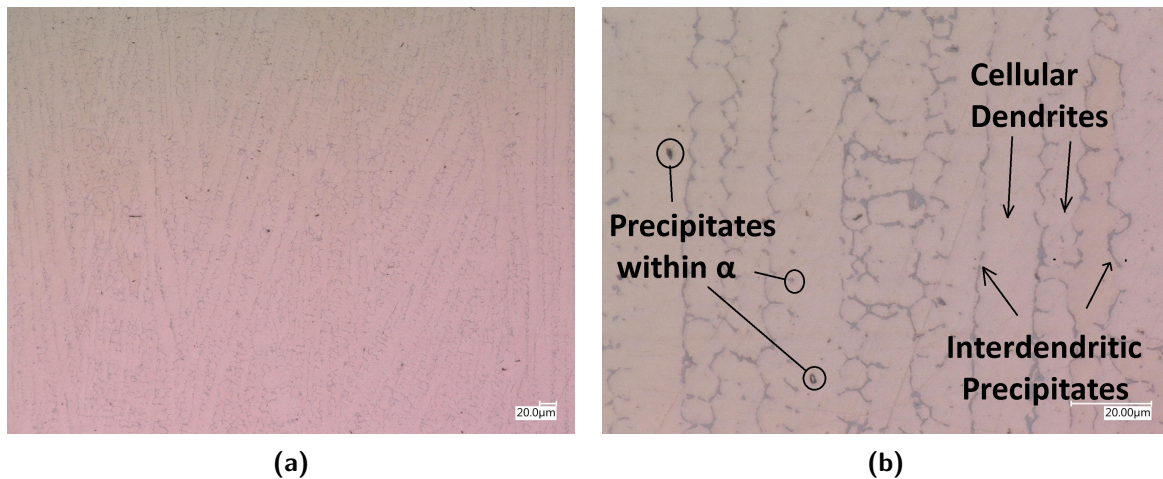


Figure 36: Optical micrographs of longitudinal cross section of MABCu deposit taken from different areas at different magnification. α phase and precipitates are indicated

The microstructure as seen in the Figure 36 (a) comprises of fine cellular dendrites about 10 μm wide. The direction of growth is along the direction of maximum thermal gradient. These cells are not completely continuous and they break at several sections along the length, combine and merge in one another. In Figure 36 (b), apart from inter cellular region, precipitates can also be observed within the grain. This indicates that during non equilibrium solidification, two kinds of nucleation and growth are observed. Firstly, the cells grow from the base plate interface along the direction of heat extraction. Simultaneously, Fe rich particles also act as nucleation sites for α copper grains. As the cellular and the equiaxed grains grow, the solid expels solute atoms (with low solid solubility) into the remaining liquid. These grains eventually upon cooling form the solid displaying a mix of cellular and equiaxed α segments with interdendritic precipitates. The microstructure however is predominantly consists of cellular morphology indicating that only a few equiaxed grains survive. It must be noted that 3-Dimensional morphology of cells and equiaxed segments can not be completely captured in a 2-Dimensional micrograph. In Figure 33, element distribution EDS maps of single phase cellular microstructure provide supporting evidence for the above mentioned analysis. Precipitates within an α Cu cells are rich in Fe, Si and Mn, whereas the interdendritic regions are rich in Fe, Ni, Mn and Si.

Figure 37 shows the X-Ray Diffraction pattern of the MABCu (Blue) sample along with the XRD pattern of MAB150 (black), the as deposited dual phase alloy discussed in Chapter 3. Peaks corresponding to Cu- FCC and Cu- BCC lattice structure are also indicated with Red and Blue, respectively. It can be evidently seen that the Cu-BCC β phase peaks are absent in the in-situ alloyed MABCu alloy. This is coherent with the above discussion about the non-equilibrium solidification microstructure. The ratio height of the Cu- α bars from the database corresponds to relative intensities from a random textured material. However, in the MABCu XRD pattern, the peaks at $2\theta = 58^\circ$ and at $2\theta = 108^\circ$ are disproportionately higher than the rest. This indicates the presence of a strong texture. Similar observations have been reported during WAAM of TiAl6V4 [42]. Further insights on texture can be obtained via EBSD analysis of the alloy but is beyond the scope of the current project.

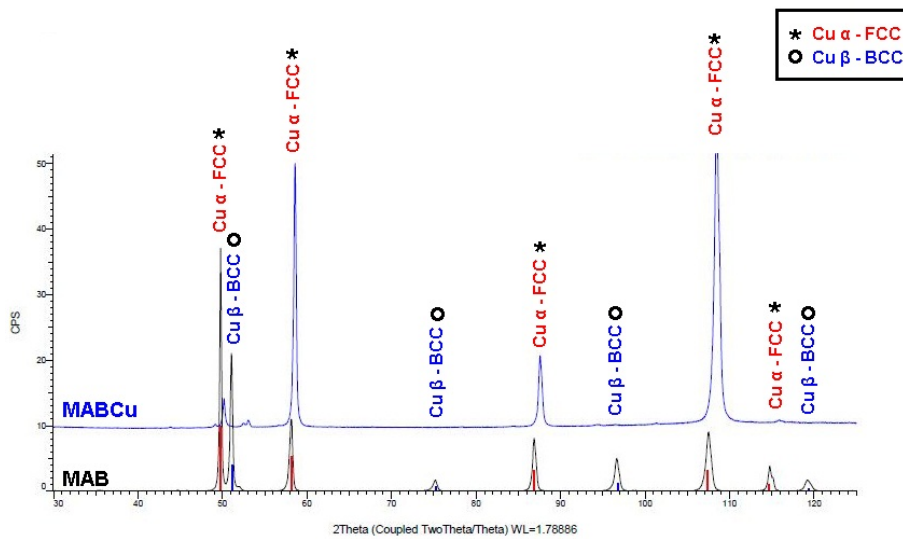


Figure 37: X-Ray Diffraction patterns of in-situ alloyed MABCu

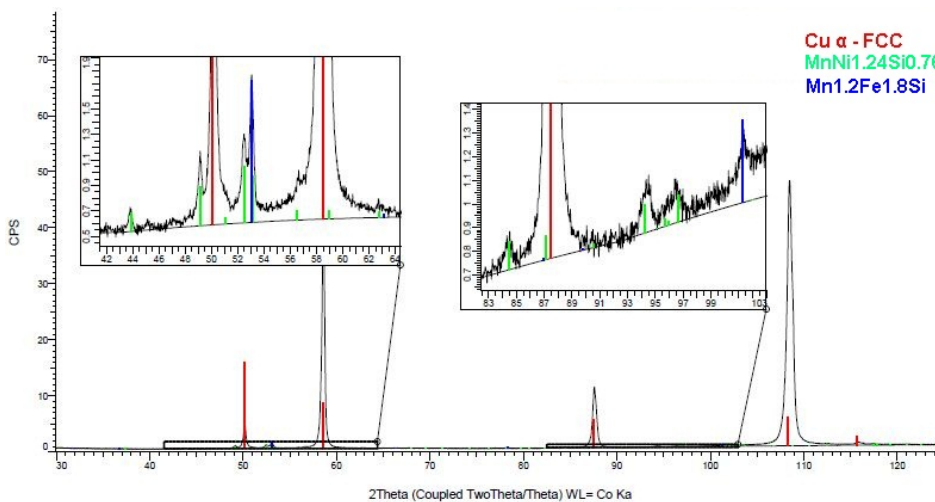


Figure 38: Selected sections of MABCu XRD pattern highlighting precipitates.

Figure 38 shows selected sections of the XRD pattern. Numerous small peaks presumably corresponding to the precipitates can be seen. Based on the EDS maps (Figure 33) and the database in Bruker software, peaks belonging to precipitates have been identified as hexagonal MnNi_{1.24}Si_{0.76} (P63/mmc) (speculated to be the interdendritic precipitates) and Mn_{1.2}Fe_{1.8}Si (BCC family, fm-3m) (speculated as the Fe rich precipitates). It is important to note that XRD patterns reveal only the crystal structure and not the exact composition of the precipitates. The results from the XRD analysis are also coherent with the evolution of the microstructure presented in the discussion. The newly developed alloy, MABCu has been further investigated to develop a greater understanding of non-equilibrium solidification and to study the stability of precipitates at high temperature by means of heat treatments.

4-3-3 Solidification Analysis

Aging heat treatment followed by water quenching was employed to study the stability of precipitates in the solidification microstructure (section 4-2-3). Selected region from X-Ray diffraction patterns of the aged and quenched samples are presented in Figure 39. The numbers associated with XRD patterns correspond to respective aging temperatures.

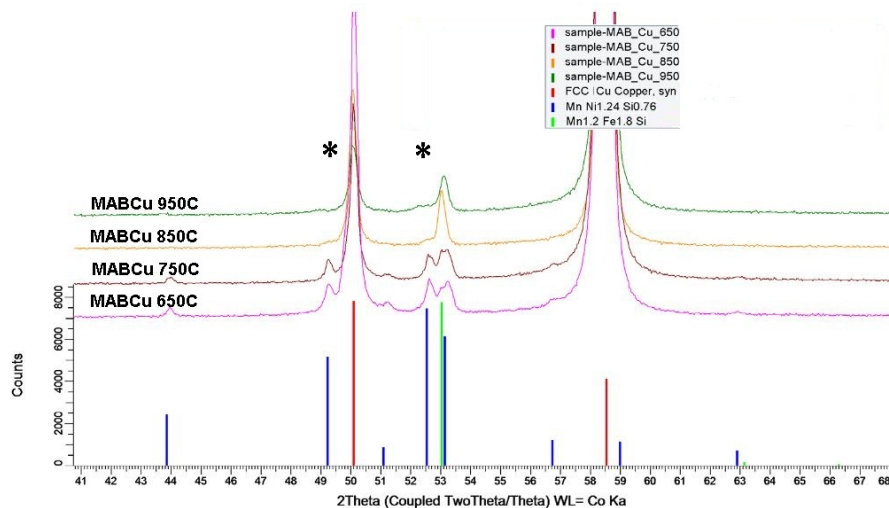


Figure 39: XRD pattern of heat treated samples. Indicator peaks corresponding to identified phases are indicated along the x-axis

Strong peaks of Cu FCC α phase can be seen for all heat treated samples. The peak for Mn_{1.2}Fe_{1.8}Si (Fe rich precipitates, $2\theta=53^\circ$) is also stable for all aging temperatures. This observation is coherent with the proposed solidification approach involving Fe rich precipitates as sites for heterogeneous nucleation of copper α phase (section 4-3-2). However, it was observed that the peaks for hexagonal MnNi_{1.24}Si_{0.76} precipitates (indicated by *) are not present in samples aged at 850 °C and 950 °C. This suggests that at an elevated temperature in the range of 750 °C and 850 °C, the interdendritic precipitates dissolve in the matrix. Upon rapid solidification the precipitation of these precipitates is suppressed. However, in XRD patterns of MABCu850 and MABCu950 at $2\theta=52.5^\circ$ a small bump (broad peak) is visible. Micrographs and EDS analysis (shown in 40) was performed on MABCu 950 to gain insights into the observation.

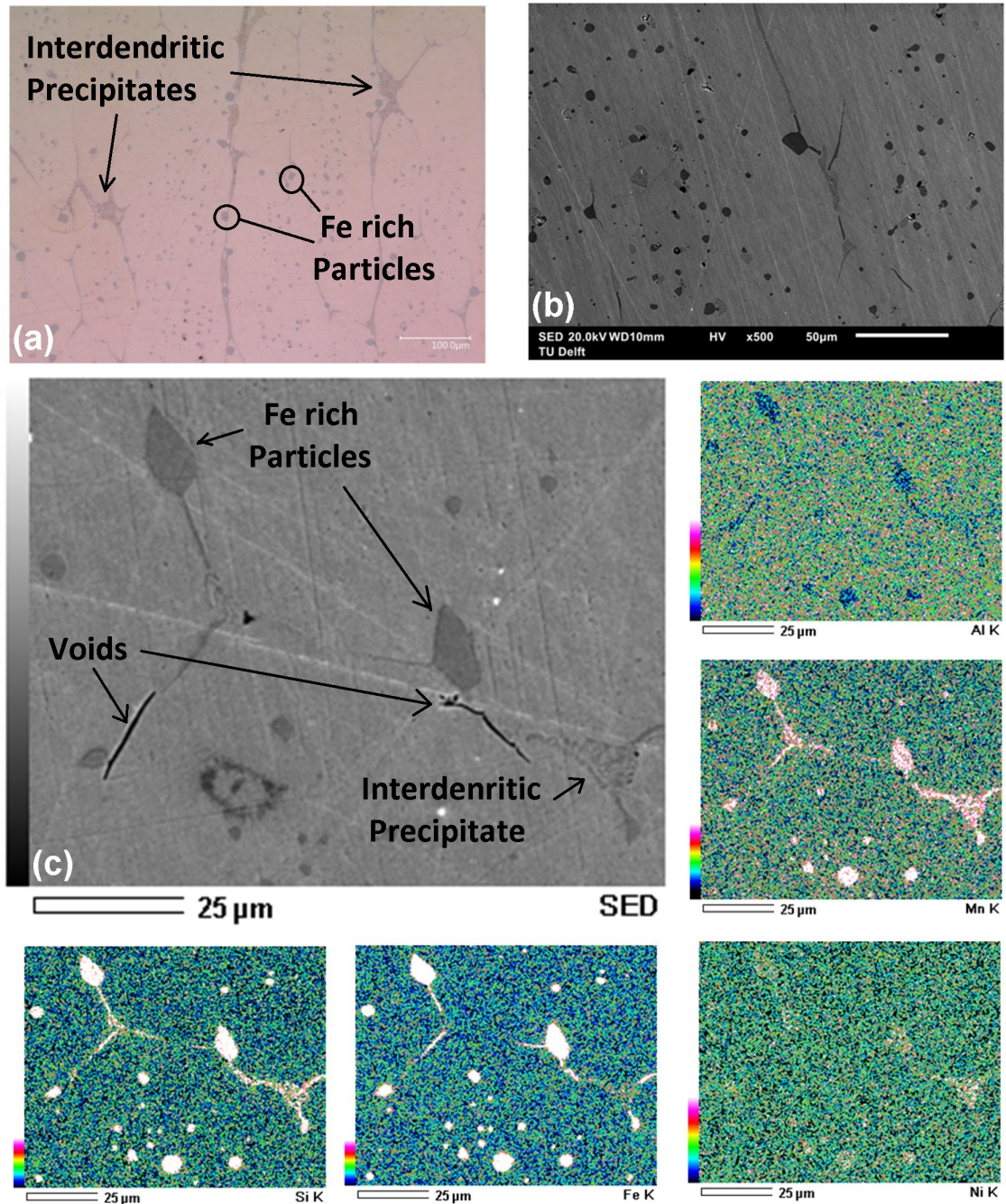


Figure 40: a) Optical Micrograph (b) scanning electron micrograph and (c) EDS Elemental Analysis of MABCu950. Two distinct kinds of precipitates can be seen.

The optical micrograph shown in Figure 40 (a) consists of an α Cu phase, circular dark precipitates and lamellar brown precipitates. Please note, the scale of the micrograph is larger than the as deposited microstructure shown in Figure 36. Hence it is suggested that during isothermal holding at 950 °C grain growth has taken place resulting in an increase of the interdendritic width from 10 μm to 100 μm . Grain boundaries are regions of high energy and hence at elevated temperatures, some grains grow and consume others to reduce the grain boundary area and hence internal energy [43]. Prominence of circular dark precipitates can be attributed to Ostwald ripening. In solid solutions at elevated temperatures, large precipitates grow in size at the expense of smaller precipitates as large precipitates are energetically favourable [43]. Similar phases and morphologies can be identified and observed in the scanning electron micrograph Figure 40 (b).

Based on the elemental maps, it is evident that the dark circular precipitates are the Fe-rich precipitates as observed in the as-deposited alloy. The brown lamellar precipitates also resemble the interdendritic precipitate (MnNi1.24Si0.76) in terms of elemental distribution. This however directly contradicts the absence of the peaks in XRD pattern shown in Figure 36. Hence, it is suggested that the interdendritic precipitate transforms into a liquid phase between the Cu α grains. Upon rapid quenching, the liquid forms a semi crystalline solid. Presence of voids in the regions surrounding the interdendritic precipitates strengthens the suggestion. These voids can be a possible consequence of a combination of solidification shrinkage in a constrained environment (in between α grains) and stresses due to differential thermal contraction [44].

To gain insights into the observations, the MABCu sample was heated to 950 °C, aged for 2.5 hrs and allowed to cool in the furnace (cooling rates less than 3 °C/min). XRD pattern of the slow cooled sample along with the water quenched sample is shown in Figure 41.

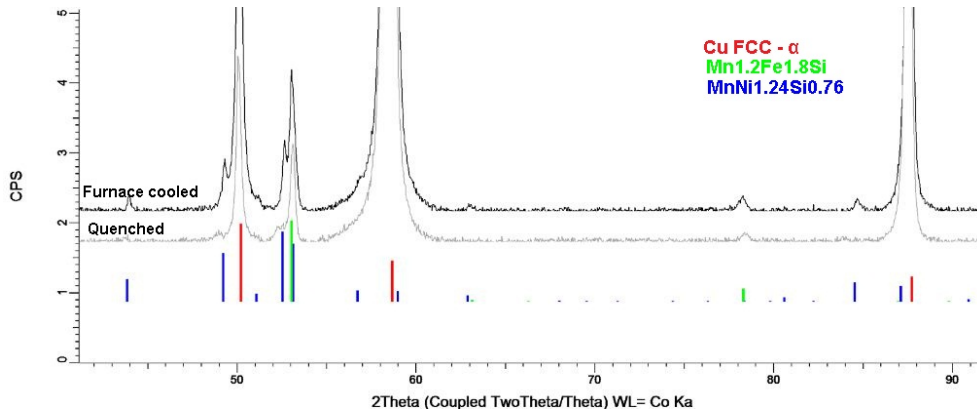


Figure 41: XRD pattern of MABCu aged at 950 °C and furnace cooled. Diffraction pattern of aged and quenched sample is plotted for reference.

It is observed that the diffraction peaks (for example $2\theta = 49^\circ$, 52° and 84°) corresponding to interdendritic precipitates (MnNi1.24Si0.76) are present in furnace cooled sample, whereas they are absent in the quenched sample. This observation is coherent with the hypothesis presented. Upon slow cooling the liquid precipitate enclosed in between Cu α grains crystallizes but upon quenching a semi-crystalline phase is obtained. Thus, the material is sensitive to thermal treatment and further analysis is needed to explore its potential applications.

4-4 Conclusions

Use of in-situ alloying as an effective microstructure control strategy during Wire and Arc Additive Manufacturing of aluminium bronze has been demonstrated. A compositionally graded deposit has been characterized for microstructure and mechanical properties. Non equilibrium solidification of a single phase bronze obtained from in-situ alloying is investigated. Following conclusions can be drawn-

- On the basis of composition, aluminium bronzes can be categorized into 3 types lying within the $L+\alpha$, the $L+\alpha+\beta$ and the $L+\beta$ region of the phase diagram. Their solidification results in single phase cellular dendritic, discontinuous dual phase and continuous dual phase microstructure, respectively.
- Continuous dual phase microstructure has a hardness of $\sim 225\text{HV}$. The hardness sharply drops as a function of β phase fraction from $\sim 225\text{HV}$ to $\sim 180\text{HV}$ for discontinuous dual phase microstructure. For single phase microstructures, the hardness drops slightly as a function of the increasing Cu concentration.
- In-situ alloyed single phase solidification microstructure consists of α phase cellular dendritic separated by inter-dendritic precipitates. Equiaxed Cu α segments with Fe rich precipitates within the grains are also observed.
- The newly developed single phase aluminium bronze is sensitive to thermal treatments and is susceptible to solidification defects like voids.

The newly developed alloy has a homogeneous single phase microstructure. This alloy will be used for corrosion and grain refinement studies in the chapters that follow.

Corrosion Behaviour

5-1 Introduction

Copper alloys have been used in the marine environments for various structural purposes like pipelines, pumps and, propellers. Aluminium bronzes particularly offer a combination of good mechanical properties and corrosion resistance. With increase in amount of aluminium, corrosion resistance of aluminium bronzes first progressively increases until a certain composition and then decreases. This composition of aluminium corresponds to the solubility limit of aluminium (%wt) in α phase. De-aluminification is rarely noticed in single phase α alloys [45]. Beyond this composition, the dual phase alloy undergoes severe selective phase corrosion (de-aluminification) [46].

Manganese aluminium bronze, our alloy of interest, has a composition corresponding to a dual phase microstructure (Chapter 3). In Chapter 4, in-situ alloying, a microstructure control strategy for WAAM processing is explored to transform a dual phase microstructure (MAB, Chapter 3) into a single phase microstructure (MABCu). In the following chapter, corrosion behaviour of the above mentioned alloys is investigated with an emphasis on susceptibility towards selective phase corrosion. To benchmark results against industrial practices, an annealed alloy (a standard practice to improve corrosion resistance of propellers) is also included in the study. Potentio-Dynamic Polarization experiments are performed in an acidic chloride medium to gain insights into the corrosion behaviour of MnAl bronzes.

5-2 Experiments

The section below describes the series of experiments that were performed to investigate corrosion behaviour of as-deposited, post processed and in-situ alloyed MnAl bronzes.

5-2-1 Materials

Three as-deposited MAB beads were obtained as described in Chapter 3 using the welding parameters tabulated in Table 9. For post processing, one of the MAB deposits was subjected to an annealing heat treatment. A Nabertherm box furnace was heated to 650°C and the weld deposit was exposed to this temperature for 2.5 hrs. The deposit was allowed to cool in the furnace ($\sim 2^\circ\text{C}/\text{min}$). The in-situ alloyed deposit was prepared by alloying an MAB deposit with Cu3Si wire as described in Chapter 4 according to parameters Table 10.

Table 9: GTAW process parameters for MAB sample

S. No	Current (Amp)	Travel Speed (mm/s)	Feed Rate (mm/s)
1	150	3	36

Table 10: GTAW process parameters for the MABCu sample

S. No	Current (Amp)	Travel Speed (mm/s)	Feed Rate (mm/s)
1.MAB	150	3	36
2.Cu3Si	150	3	36

To fabricate the electrodes for electrochemical analysis, 1.5 cm long sections were cut from each deposit namely MAB (as-deposited), MABHT (post-processed) and MABCu (in-situ alloyed). A multistrand copper wire was attached at the base of the deposit using a lead-free solder to establish electrical contact. The wire and weld assembly cold mounted in a non-conductive resin as schematically shown in Figure 42 (a). Three different samples were polished using standard metallographic procedures to expose $\sim 0.75\text{ cm}^2$ from the top of weld beads as shown in Figure 42 (b).

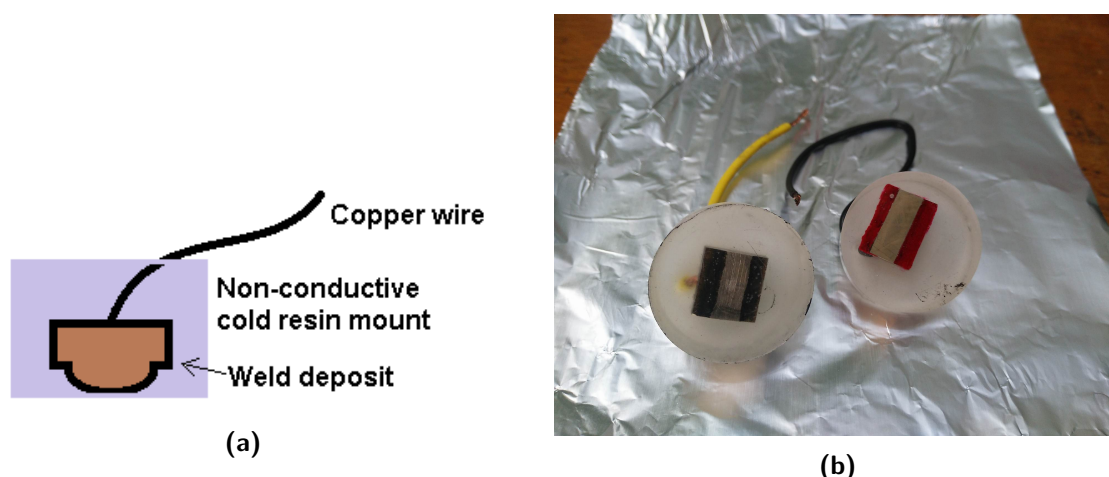


Figure 42: Electrodes for electrochemical polarization experiments (a) Schematic of embedded weld bead (b) polished samples of electrodes

The corrosive medium (electrolyte) was prepared mixing 100 mL 0.1M HCl with 29.25 g NaCl in 900 mL H_2O using a magnetic stirrer at room temperature. This resulted in a 0.01M HCl + 0.5M NaCl solution. The pH of the solution was found to be 2.12.

5-2-2 Electrochemical Polarization

Polarization tests were carried out in an electrochemical cell containing 100 mL of 0.01M HCl + 0.5M $NaCl$ solution using a standard 3 electrode configuration. A graphite counter electrode and an $Ag/AgCl$ reference electrode are used along with the respective samples as working electrodes. A schematic of concentration cell along with the electrodes can be seen in Figure 43. It should be noted that all the potentials were measured and plotted against Standard Hydrogen Electrode (SHE) after conversion from the $Ag/AgCl$ reference electrode. Experiments were conducted in absence of oxygen. In order to achieve this, before the experiments, the solution was flushed with N_2 gas for 15 mins in the beaker covered with a paraffin sheet. All electrochemical tests were conducted using an AutoLab Potentiostat Galvanostat.

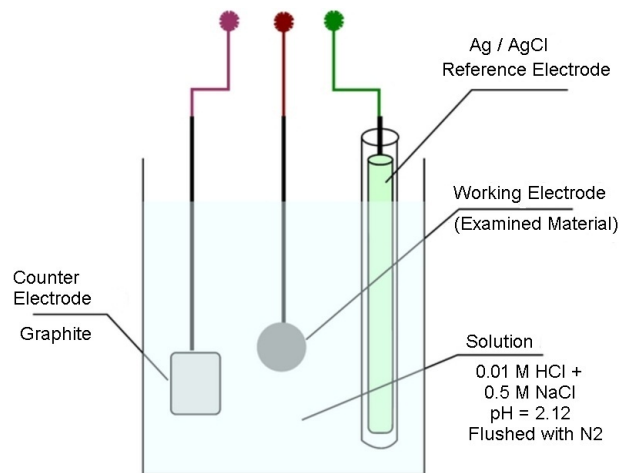


Figure 43: A schematic of experimental setup for electrochemical analysis [47]

Open circuit potential (E_{OCP}) was determined for all samples prior to respective potentiodynamic polarization (PDP) measurements by immersing the specimen in the electrochemical cell for 30 minutes. For PDP measurements, the potential was scanned from $-200\text{ mV v/s } E_{OCP}$ to $+200\text{ mV v/s } E_{OCP}$ at a scan rate of 0.5 mV/s . Subsequently, the Tafel extrapolation method was used to extract the polarization parameters from the PDP measurements. To further study the mechanism of corrosion, anodic polarization experiments were performed. After immersing samples at OCP for 30 mins, a potential scan from $-50\text{ mV v/s } E_{OCP}$ to $+1500\text{ mV}$ was performed. Conclusions regarding the relationship between the microstructure and the corrosion rate were drawn on the basis of $E\text{ v/s log}(i)$ graphs.

5-2-3 Surface Morphology Analysis

Finally, the surface morphology of the corroded surfaces after potentiodynamic polarization experiments were characterized using scanning electron microscope (Jeol JSM-IT100) to reveal insights regarding the nature of corrosive attack.

5-3 Results and Discussions

5-3-1 Microstructure

Figure 44 shows the optical micrographs of as-deposited, heat treated and in-situ alloyed specimen. Figure 44 (a) shows a continuous dual phase microstructure MAB consisting of primary β grains with grain boundary α along the prior β grain boundaries and Widmanstätten α within the grain. This microstructure has been discussed in Chapter 3 in more detail. Figure 44 (b) shows a fine grained single phase α microstructure MABHT. At the elevated temperature of 650 °C retained β transforms into α phase. The pre-existing α grains remain unchanged. Also, a large density of precipitates can be observed, which is a result of aging at high temperature (XRD pattern of MABHT can be seen in Appendix A). Figure 44 (c) shows the in-situ alloyed cellular dendritic single phase α microstructure as described in section 4-3-2

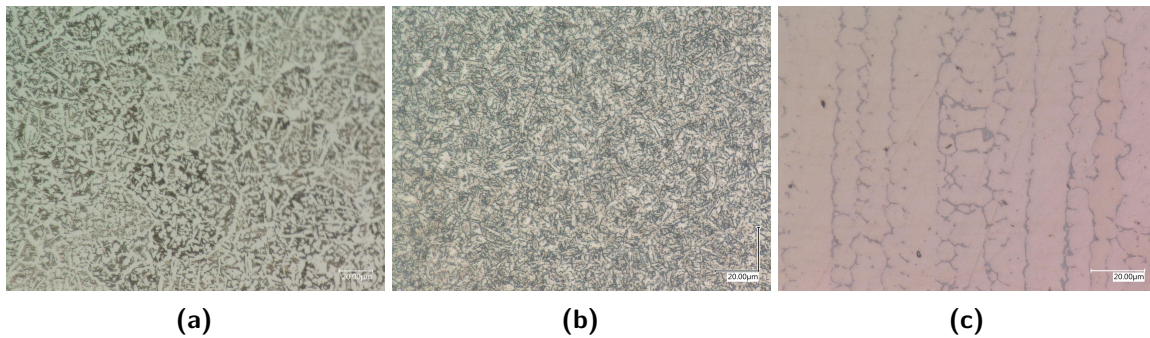


Figure 44: Optical Micrographs of (a) MAB (b) MABHT and (c) MABCu

5-3-2 Potential - pH Diagram

Pourbaix diagram or E - pH diagram represents electrochemical equilibria between different species in an aqueous media. They provide thermodynamic basis for the stability of phases in relation with the pH of the solution and the applied overpotential. Different regions correspond to the phases with minimum free energy. These diagrams play an instrumental role in understanding dissolution and passivation behaviour of alloys. Pourbaix diagrams for three principal elements namely Cu, Mn and Al are shown in Figure 45 (a) (b) and (c) respectively. Figure 45 (d) shows a selected region of a multi-element Pourbaix diagram consisting of 81% Cu + 11% Mn + 7% Al (\sim MAB composition). The diagrams have been obtained from open source collaborative database www.materialproject.org.

The lines in Pourbaix diagrams show equilibrium between activities of species on the either side calculated using Nernst equation. The respective species are predominant on each side of the line [48]. Factors like temperature and concentration of ionic species affect the stability of phases and shift the lines. Concentration of all ions in the software by default is $10^{-6}M$. The two orange dashed lines show the H_2 reduction line (lower) and line for oxidation of water to oxygen (upper). Below the Hydrogen line, H_2 gas evolves at the cathode and above the Oxygen line, O_2 gas evolves at anode. Stability regions corresponding to water, hydrogen and oxygen are labeled in Pourbaix diagram for copper. Pourbaix diagrams can be used to

get an indication about regions of immunity (metal is stable in solid form), corrosion (metal is stable in ionic forms) and passivity (metal oxides are stable). In a solution of pH of 2.12, solid metal and its cations are stable from -1 V to 1 V for all the three elements. It is important to note that these diagrams are based on thermodynamics and no predictions can be made about the rates of corrosion [48].

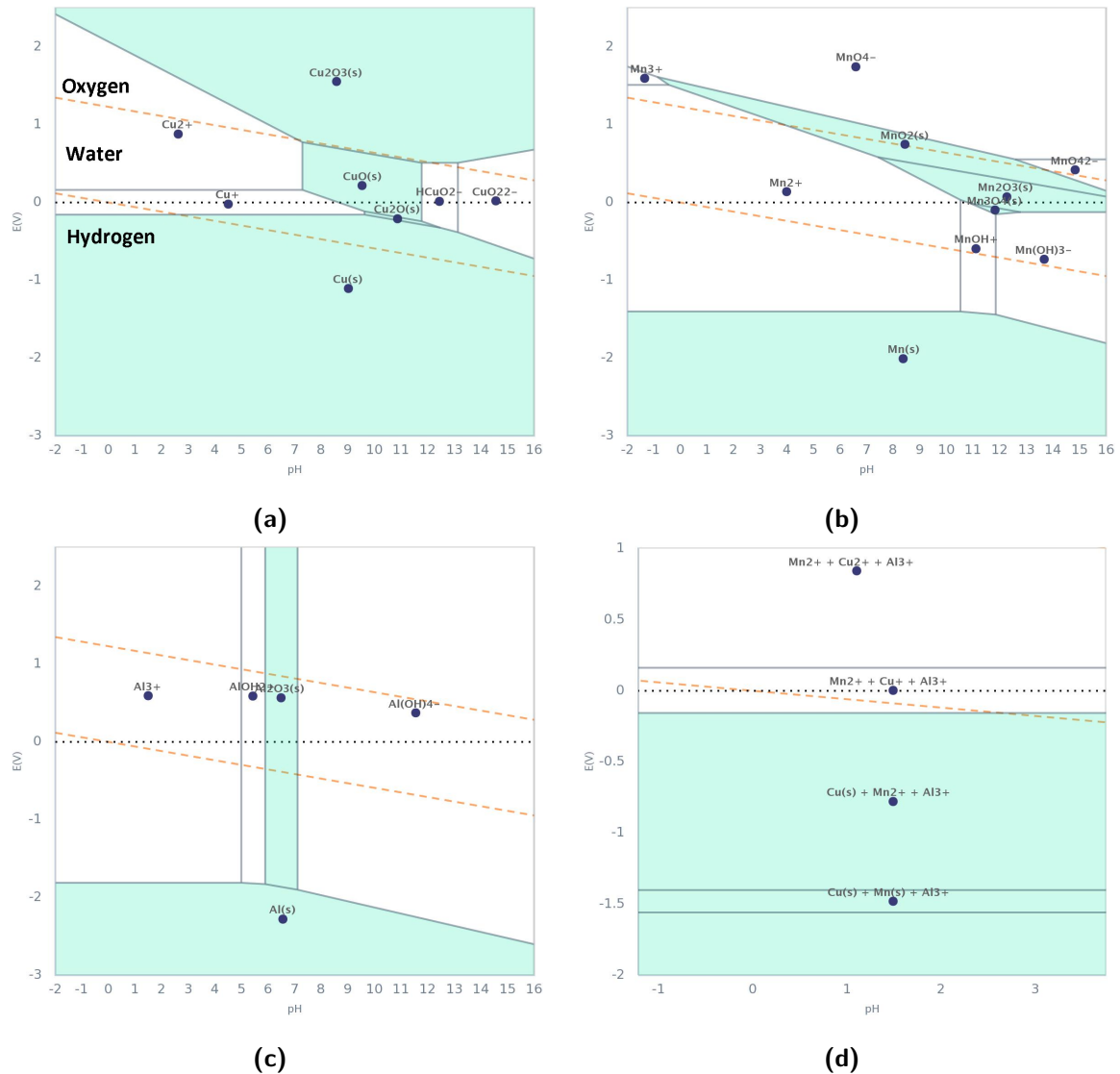


Figure 45: Pourbaix diagrams (a) copper (b)manganese (c) aluminium d) Cu₁₁Mn₇Al (MAB)

5-3-3 Electrochemical Polarization

Figure 46 shows selected open circuit potential curves of the three alloys. It can be observed that in the given time frame of 1800 seconds, a steady electrode potential was achieved for all the three alloys after a different initial transient behaviour. Similar values suggest that copper plays a dominant role in the electrochemical equilibrium. OCP measurements in

corrosive media for extended durations of time can potentially show appreciable differences in the behaviour.

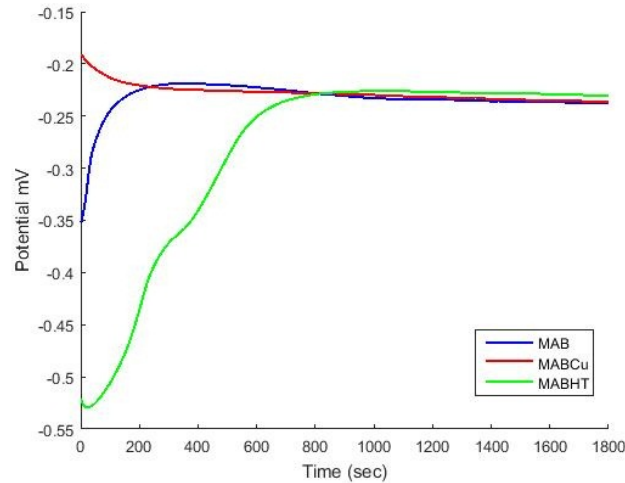


Figure 46: Open Circuit Potential of alloys under consideration

Figure 47 (a) shows average potentiodynamic polarization curves for different microstructures under consideration. The values in the curve represent a mean of three sets of repetition of the experiments. The value on the potential axis is adjusted against SHE from Ag/AgCl electrode. In the excess of H^+ ions at low pH values, mixed charge transfer and mass transfer polarization kinetics is assumed [49, 50]. Hence, using Tafel analysis E_{corr} and i_{corr} values from repeated measurements have been extracted in Table 11. A schematic diagram showing Tafel extrapolations to extract different parameters is presented in Figure 47 (b)

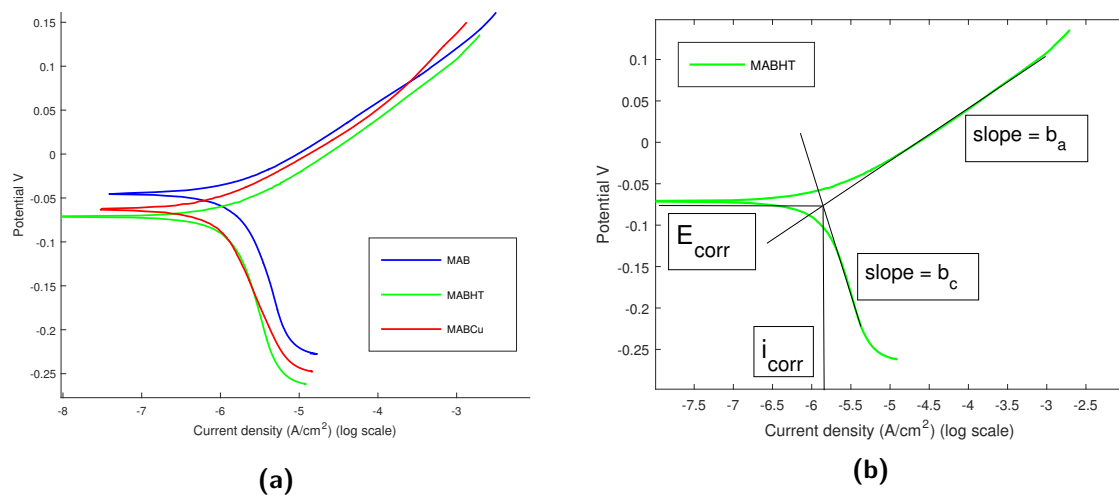
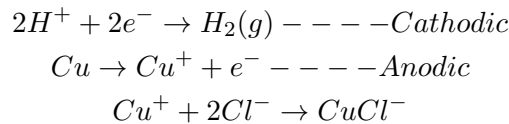


Figure 47: (a) Potentiodynamic Polarization plots for different microstructure (b) A schematic illustration showing Tafel extrapolation and various parameters for MABHT microstructure.

Table 11: Potentio-dynamic Polarization parameters of MAB, MABHT and MABCu microstructures immersed in 0.01M HCl+0.5M NaCl solution. Data is an average value of three experiments.

Material	$ b_{anodic} $ (mV/decade)	$ b_{cathodic} $ (mV/decade)	E_{corr} (mV)	i_{corr} ($\mu A/cm^2$)
MAB	60	305	-247 ± 2	1.92 ± 0.09
MABHT	64	300	-274 ± 9	1.42 ± 0.24
MABCu	54	204	-260 ± 7	0.70 ± 0.02

In absence of oxygen, in acidic conditions, the cathodic half cell reaction is evolution of hydrogen gas [51]. The initial primary anodic half cell reactions associated with copper is the formation of Cuprous Chloride ions [51]. The reactions are shown below.



The anodic arms of all three microstructures show a typical Tafel behaviour where the potential values increase linearly with $\log(i)$. Anodic Tafel slopes lie in the range of 54-64 mV/decade and no distinct differences can be observed. Similar values of Tafel slopes have been reported for copper alloys in neutral chloride solutions [52, 51]. Clear differences are seen in the cathodic arms of the polarization curves. Cathodic Tafel slope for MAB and MABHT are 1.5 times larger than the slope of MABCu alloy indicating slower kinetics of H_2 evolution for the later. This can be attributed to a homogeneous microstructure and lower amount of aluminium in MABCu. MAB and MABHT (7%Al by weight) microstructures, are richer in aluminium as compared to MABCu (5% Al by weight). The absolute values of current density are also higher for cathodic arm of MAB. It is hence speculated that due to presence of cathodic (α) and anodic (β) phases, a large number of galvanic couple sites get activated resulting in larger current density and the evolution of H_2 gas.

The rate of corrosion is given by,

$$R_m = \frac{M}{nF\rho} * i_{corr}$$

where M is the atomic mass of metal (Cu - 63.5), n is the number of electron taking part in the reaction and ρ is the density of metal (7.53 g/cm^3)[48]. Hence, i_{corr} values from Table 11 indicate that owing to its homogeneous microstructure, the in-situ alloyed MABCu alloy has a ~ 3 times lower rate of corrosion than the as deposited MAB alloys. However, it should be noted that potentiodynamic polarization experiments alone do not provide conclusive and holistic information about complex phenomena of corrosion resistance. Detailed analysis are needed to explore resistance of the materials towards other common forms of corrosion like pitting, erosion and crevice corrosion.

To gain insights into the mechanism of corrosion, anodic polarization was performed as described in section 5-2-2. Figure 48 (a) shows anodic polarization curves for MAB, MABHT

and MABCu microstructures. Figure 48 (b) shows a selected region from the same graph to better visualize the slopes.

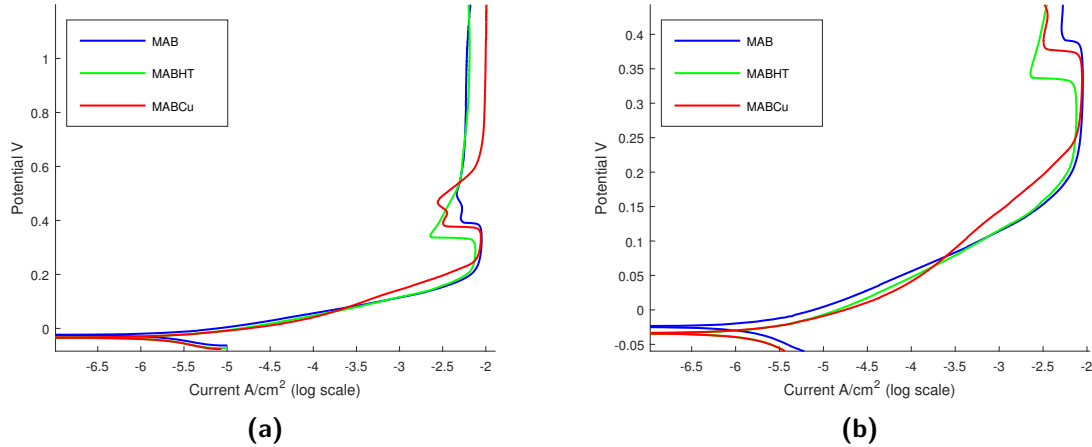


Figure 48: Anodic Polarization curves corresponding to MAB, MABCu and MABHT microstructures. (a) an overview and (b) a selected region from the curves.

It can be seen from the polarization curves in Figure 48 (a) that no passivation was observed in all the three microstructures. At a positive potential of about 200 mV against SHE, limiting current is observed in all the copper alloys. In the literature, this peak current has been attributed to CuCl formation [53, 54]. Anodic currents at even higher overpotentials are associated with formation and dissolution of CuCl, involving Cu^{+2} ions [54]. This observation is coherent with the stability of Cu^{+2} ions in Cu Pourbaix diagram shown in Figure 45 (a). Notably, in Figure 48 (b) for MABCu, the slope of polarization curve changes slightly above an overpotential of 0.05 mV v/s SHE. The microstructure of MABCu alloy, shown in Figure 44 (c), comprises of columns of α phase separated by interdendritic precipitates. It is speculated that precipitates preferentially corrode in the initial stage. Once the precipitates get depleted from the top surface, only the α phase may corrode resulting in a different kinetics and hence the slope of polarization curve. Contrary to this, in MAB and MABHT microstructures, there is abundance of anodic sites namely β phase and grain boundaries, respectively. Hence, a consistent slope is observed while the anodic regions selectively corrode over the entire range. To substantiate the claims made above, further investigations into electrochemical stability of precipitates and local measurements will be needed, which are beyond the scope of current work.

5-3-4 Surface Morphology Analysis

SEM micrographs of corroded surfaces after being subjected to an overpotential of +200 mV v/s E_{OCP} during PDP tests can be seen in Figure 49.

The morphology of attack on the surface in Figure 49 (a) suggests that β phase has preferentially corroded. This observation is consistent with studies in literature [13]. In Figure 49 (b) grain boundaries of MABHT microstructure were prone to corrosion. Due to fine grain size and abundance of grain boundaries, the attack is relatively severe. In MABCu, Figure 49 (c)

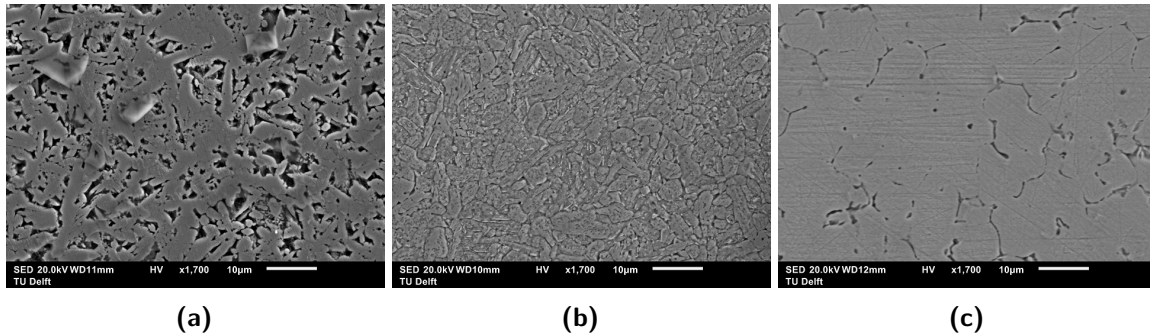


Figure 49: Electron micrographs of alloy surfaces subjected to forced corrosion during polarization experiments (a) MAB, (b) MABHT and (c) MABCu

the consequences of attack are far less severe. Interdendritic precipitates (discussed in section 4-3-2) have been preferentially dissolved. XRD and EDS analysis can provide additional information about the phases lost due to corrosion, however, they have not been explored in current work.

5-4 Conclusions

The corrosion behaviour of three Cu alloys, as deposited MAB, post processed MABHT and WAAM processed in-situ alloyed MABCu was investigated. Open circuit and potentiodynamic polarization analysis were performed in 0.01M HCl + 0.5M NaCl electrolyte. Based on the results, the following conclusions can be drawn -

- Anodic behaviour of all the three alloys are similar and are largely governed by the reaction $Cu \rightarrow Cu^+ + e^-$. Peak currents are observed at positive overpotential of ~ 200 mV v/s SHE due to formation of CuCl.
- Clear differences are evident in cathodic polarization behaviour. MABCu has slower kinetics of H_2 gas evolution due to its homogeneous microstructure. Larger cathodic currents were observed for as deposited MAB since α and β phases form galvanic sites for cathodic reaction.
- Corrosion current density and hence the rate of corrosion of in-situ alloyed MABCu alloy is ~ 3 times lower as compared to as-deposited MAB alloy.
- In MAB alloys, the β phase is the preferential attack site causing severe surface degradation. In MABHT and MABCu, attack occurs in the grain boundaries and is far less severe.

Current work indicates that in-situ alloying (Chapter 4) shows improvement in resistance against selective phase corrosion. Further investigations are needed to develop a holistic understanding of corrosion resistance of the alloys. The new alloy (MABCu) shows improvement in corrosion resistance but has lower mechanical strength (hardness). Hence in next chapter, microstructure control strategies to improve mechanical behaviour are explored.

Grain Refinement

6-1 Introduction

Microstructure plays an important role in the resulting mechanical and functional properties of a material. Primary grain morphology of solidification microstructure is governed by thermal gradient, speed of solidification front and local composition near solid-liquid interface (discussed in section 2-3). During wire and arc additive manufacturing using GTAW, heat is extracted towards the base plate against the direction of deposition across a steep thermal gradient [55]. The single phase cellular microstructure of our alloy thus obtained has been discussed in detail in section 4-3-2.

One of the key shortcomings of WAAM is that the mechanical properties are inferior to conventional manufacturing processes. This can be attributed to epitaxial grain growth (section 2-3-2) and hence anisotropy in properties [4]. An equiaxed grain structure on the other hand ensures uniform and enhanced mechanical properties [56].

Deliberate suppression of columnar grains in order to form equiaxed microstructure is an industrially important and widely studied approach of grain refinement in the field of ingot casting for Al and Mg alloys [56, 57]. Addition of potent nuclei in the form of inoculants has been used as a common strategy to achieve grain refinement and columnar to equiaxed transition, CET. According to classical nucleation theory, presence of heterogeneous substrates (surface of inoculant particles) reduces the free energy barrier for nucleation and hence promotes finer grains [58]. For a particle to be a potential nucleating site, it should have a higher melting point than the parent alloy, good wetting with surrounding liquid (interfacial energy γ), should be uniformly distributed [56]. Microalloying additions of elements like Zr, Ag, P, B to de-oxidised copper ingots have been explored previously by researchers [59, 60]. Balart et al. identified Ag as a critical microalloying element for grain size control in copper.

In the following chapter, addition of inoculants is explored as a microstructure control strategy towards improving mechanical properties of the WAAM processed single phase copper alloy discussed in Chapter 4 of this thesis. For simplicity, amount of iron (a potential candidate for inoculation), an existing alloy component (as opposed to foreign element like Ti, Zr and Ag), has been increased and the evolution of microstructure has been investigated.

6-2 Experiments

A conventional GTAW setup (described in section 3-2) was used to perform the experiment. To investigate the role of addition of inoculants on grain refinement, a coil made from high purity 99.5%wt Fe was added to the in-situ alloyed MABCu deposit (as described in section 4-2). A 0.2 mm diameter Fe wire was wound around itself in order to create a multi-strand twisted coil with a length of 70 mm. The configuration of the coil and hence the mass distribution along its length is schematically shown as an orange line in Figure 51 (a). The configuration of the coil was chosen to increase the percentage of Fe in the deposit progressively from 2%wt (original MABCu composition) to 5%wt. The value of 5% was arbitrarily chosen based on composition of NAB alloy, a commercial aluminium bronze with excellent mechanical properties.

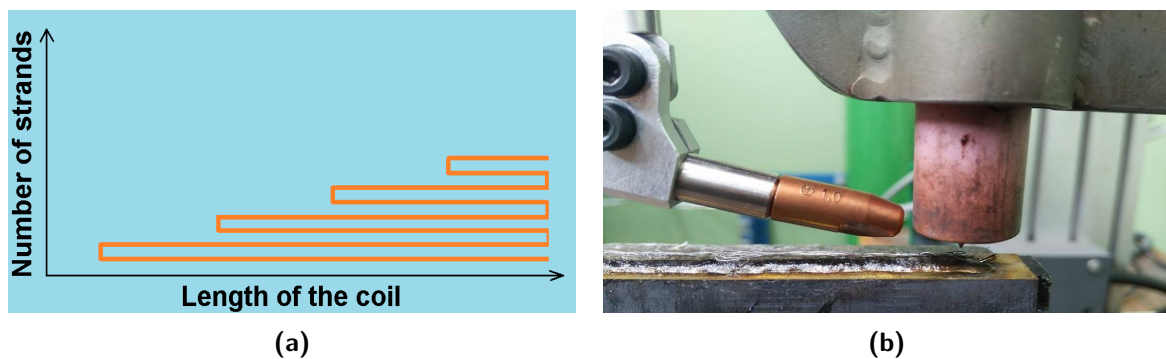


Figure 50: (a) A schematic of coil configuration and mass distribution along the length of the deposit. (b) the welding setup along with MABCu deposit and Fe coil spot welded onto it.

The Fe coil was spot welded at its ends along the length of the MABCu deposit as shown in Figure 51 (b). The coil and deposit were subjected to a heat input using a gas tungsten arc (length - 2.5 mm). The welding parameters applied in this experiment are tabulated in Table 12. The table also contains welding parameters associated with the MABCu deposit. No additional consumable wire was feed via the feeder during this grain refinement welding pass (unlike section 4-2-2).

Table 12: Processing parameters for grain refinement analysis

S. No/ Material	Current (Amp)	Travel Speed (mm/s)	Feed Rate(mm/s)
1/MAB	150	3	36
2/Cu3Si	150	3	21
Fe	150	3	-

The deposit thus obtained was characterized for its microstructure and hardness. A longitudinal cross section along the length of the deposit was polished using standard metallographic procedures. Microstructure was characterized using optical microscopy and SEM/EDS. Localized mechanical behaviour of the deposit was investigated by means of hardness measurements. Trends were obtained using 5 series of 40 indents each (500 μm apart along the height and length) measured with a load of 0.5 kgf/mm^2 (0.5 HV). Observations are presented and discussed in the sections below.

6-3 Results

6-3-1 Process

An inconsistent deposition and alloying process was observed during the experiment. A bulb of liquid iron was observed at the tip of the coil above the MABCu deposit where it interacted with the arc. As the arc travelled over the Fe coil, the molten bulb grew in mass and size, until a critical mass was reached. At this critical mass, the droplet detached from the coil under its own weight and fell within the MABCu melt pool below it. The process of bulb formation and droplet detachment continued as the arc travelled over the deposit. Hence, alloying within the melt pool took place at discrete instances and not continuously. This has been schematically represented in Figure 51.

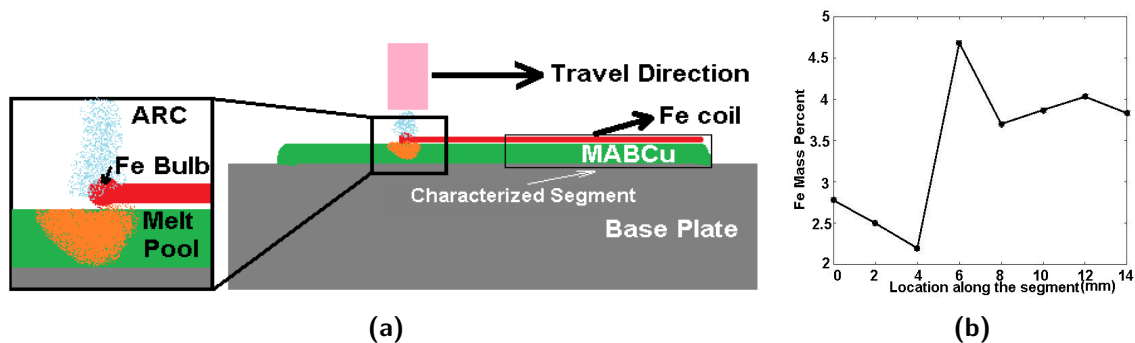


Figure 51: (a) Schematic diagram of grain refinement alloying process (b) Mass % of Fe along the segment, determined using EDS

Thus, remelting the MABCu deposit by GTAW while feeding an iron coil does not produce a consistent and homogeneous microstructure. The chemical composition and thus, the development of microstructure will change with both time and location. Possibilities of wire feeding or blown powder need to be explored for robust, reproducible and homogeneous outcomes.

6-3-2 Microstructure

A segment of the deposit was sectioned and characterized using optical microscopy and vickers hardness indentation. Segment is schematically shown and labeled as "characterized segment" in Figure 51. Figure 52 shows an optical macrograph of the segment including hardness indents. Similar to Figure 30, the dark regions represent FCC Cu α phase (region B in Figure 52). The lighter regions correspond to the β phase and the grain boundaries (region D in Figure 52). Concentration of Fe from left to right along the deposit as shown in Figure 51 (b). However, no particular trend was observed.

In the Figure 52, patches of light and dark regions indicate that a heterogeneous microstructure has been obtained. This can be explained as a consequence of inconsistent alloying during process. The microstructure of selected regions related to droplet transfer (labeled as A,B,C and D correspondingly in macrograph 52) are shown in Figure 53. Based on the EDS data, Fe wt% representative of each microstructural region is mentioned in the respective subcaptions.

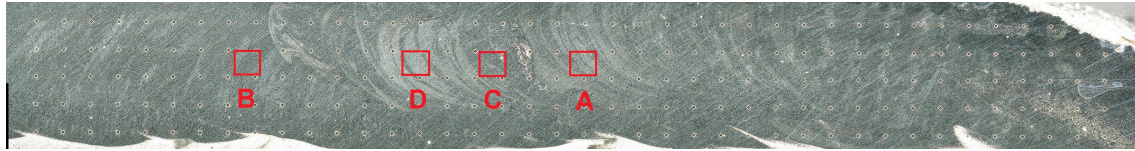


Figure 52: Macrostructure of Fe enriched MABCu deposit

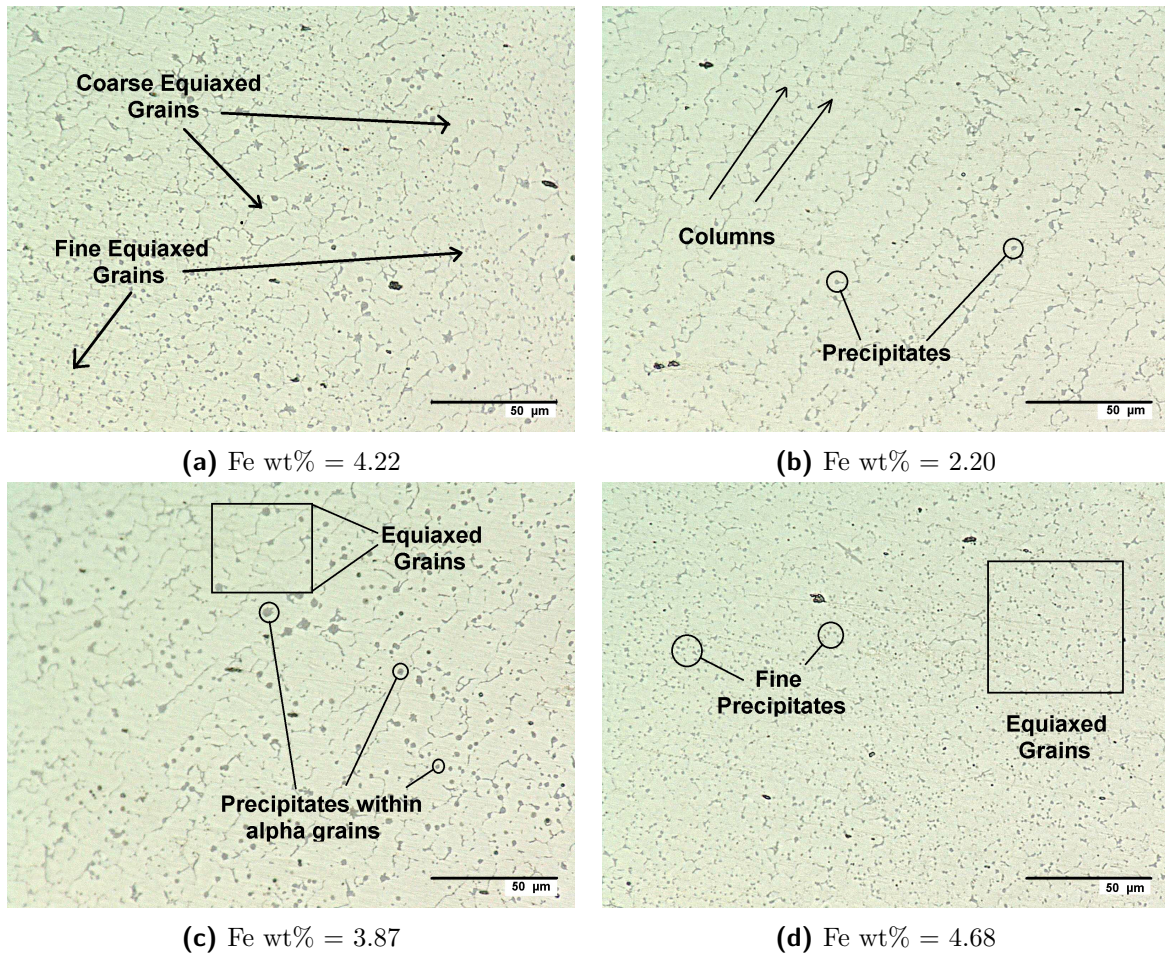


Figure 53: Optical micrographs of different regions in the grain refined deposit (a) Heterogeneously distributed Fe dispersoids (b) columnar alpha (c) coarse equiaxed and (d) fine equiaxed

Figure 53 (a) shows the extent of heterogeneity in the microstructure. The coarse and fine equiaxed grain regions can be seen as alternate bands less than $25\mu\text{m}$ wide. The heterogeneous microstructure of the deposit was characterized into 3 different morphologies that can be seen in Figures 53 (b), (c) and (d). Figure 53 (b) shows a columnar microstructure similar to in-situ alloyed microstructure as discussed in 4-3-2. Due to addition of Fe as an inoculant, the microstructure is enriched with precipitates, but Columnar to Equiaxed Transition (CET) was not observed. The alpha phase predominantly is still columnar. In regions with higher Fe content (~ 3.5 wt%), CET (Figures 53 (c) and (d)) was observed. Further investigations with a robust processing method are needed to investigate changes in morphologies.

In Figure 53 (c) and Figure 53 (d), the equiaxed morphology of α copper grains is evident. Columns as seen in Figure 53 (b) are no longer present. Precipitates within α grains indicate that they served as the heterogeneous nucleation sites during non-equilibrium solidification. In Figure 53 (c), a lower number of active nucleants resulted in relatively larger equiaxed grains as compared to Figure 53 (d) where a larger number of finely dispersed precipitates subsequently give rise to finer Cu α grains.

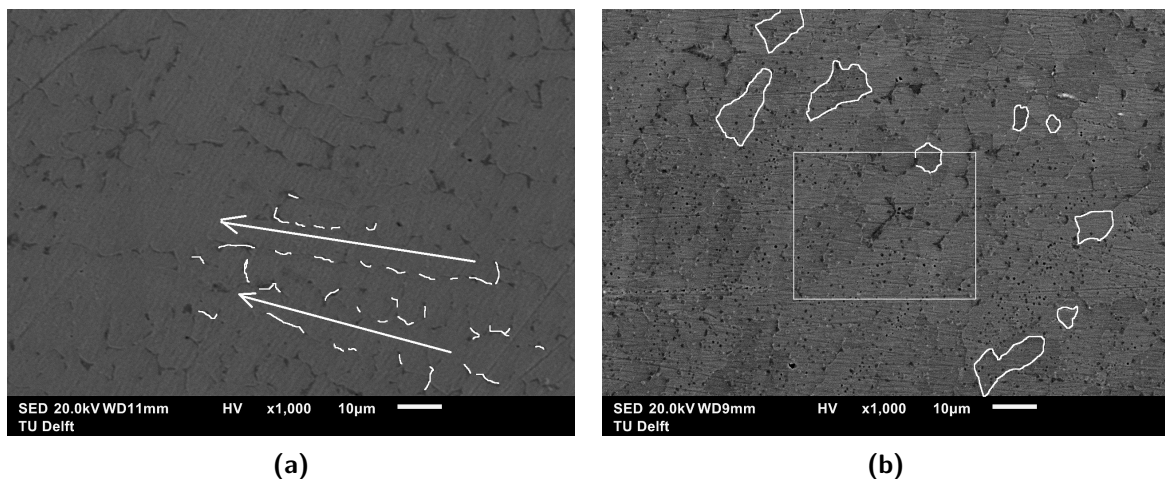


Figure 54: Scanning electron micrographs of (a) MABCu (Chapter 4) consisting of columnar grains (b) Fe enriched MABCu deposit consisting of a equiaxed grains

In Figure 54 scanning electron micrographs (at same magnification) of the in-situ alloyed columnar and grain refined equiaxed microstructures can be seen. Figure 54 shows Cu α phase columns separated by interdendritic precipitates (discussed in detail in section 4-3-2). Some precipitates have been highlighted to show α columns (also shown using arrows). Columnar to Equiaxed Transition has been achieved upon addition of Fe (Figure 54 (b)). Some representative grain boundaries are highlighted to show change in morphology. Regions corresponding to coarse and fine dispersed precipitates can be seen. The area marked in Figure 54 (b) was further investigated using EDS, the corresponding elemental maps can be seen in Figure 55. The Fe rich precipitates comprise of Fe, Mn and Si. Hence it is speculated that $\text{Mn}_{1.2}\text{Fe}_{1.8}\text{Si}$ precipitates may be present as was also observed in the in-situ alloyed microstructure in section 4.3.2. The interdendritic $\text{MnNi}_{1.24}\text{Si}_{0.76}$ precipitates were not visible in the elemental maps. XRD analysis of a bulk sample can be performed in future to gain more insights into precipitates present within the system.

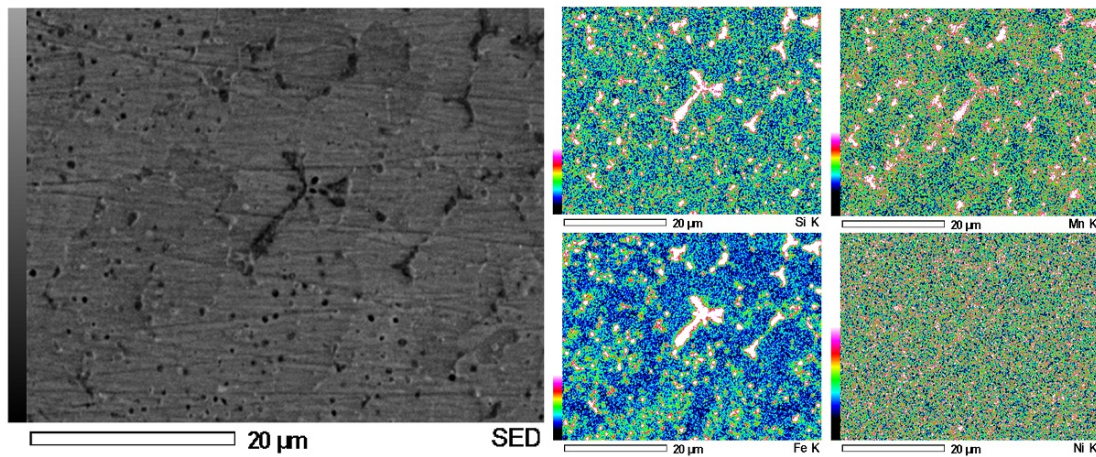


Figure 55: Scanning electron micrograph of grain refined microstructure along with the EDS elemental maps of the selected region

6-3-3 Hardness

The result of hardness measurement can be seen in Figure 56. Five series of 40 indents each have been depicted as a contour map. The location of the indents can also be seen in the macrograph in Figure 52.

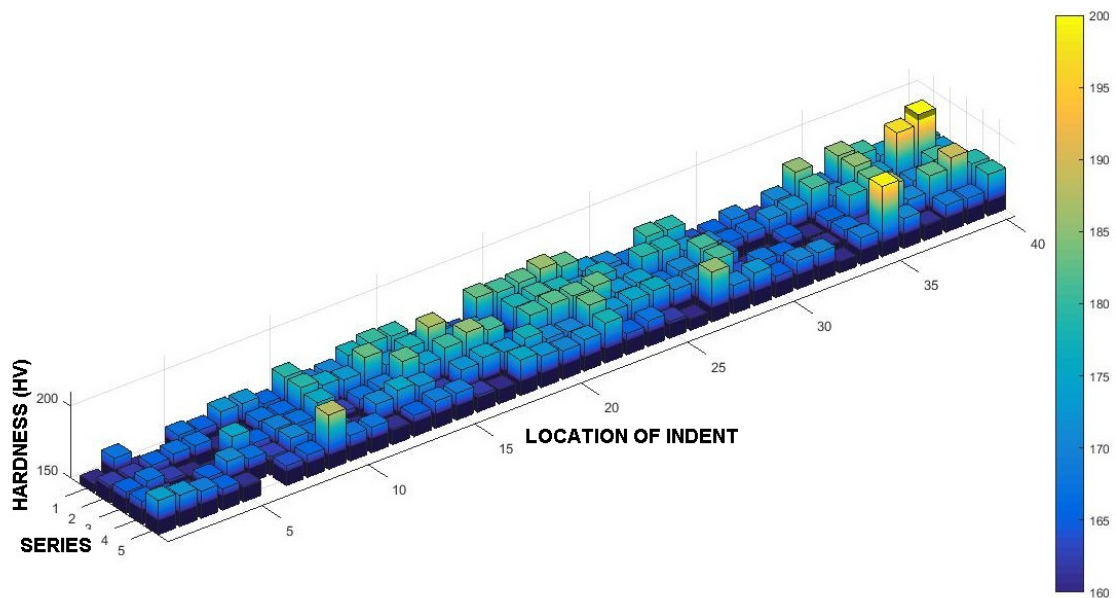


Figure 56: A 3D bar plot depicting hardness values of 0.5HV indents marked along the deposit

In the Figure 56, the XY plane is a grid of 5X40 elements, each corresponding to an indent on the grain refined structure. Heights of the bars correspond to hardness value associated with the indent on the corresponding location. The color of the top surface of the bar indicates the value as depicted by color bar on the right. Limits of values on Z axis have been selected to

pictorially show the differences in hardness values. Minimum hardness value was 149 HV and maximum value was 204 HV. No clear trends can be observed along the length of the deposit. This can be explained by heterogeneous microstructures throughout the deposit. However, to understand the relationship between hardness values and grain refinement, indents were categorized into 3 groups based on their microstructural environment, namely, columnar, coarse equiaxed and fine equiaxed. Figure 57 shows representative indents of corresponding categories.

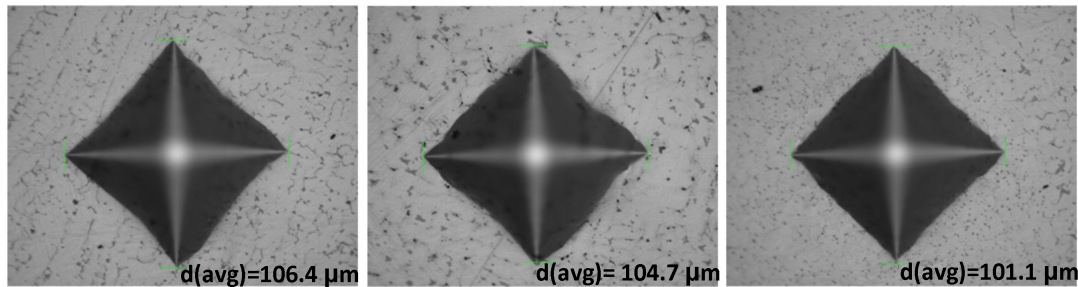


Figure 57: Indents categorized according to their microstructural environment (a) columnar (b) coarse equiaxed and (c) fine equiaxed

Ten indents each corresponding to the three different categories were selected and analysed. The results have been plotted below in Figure 58

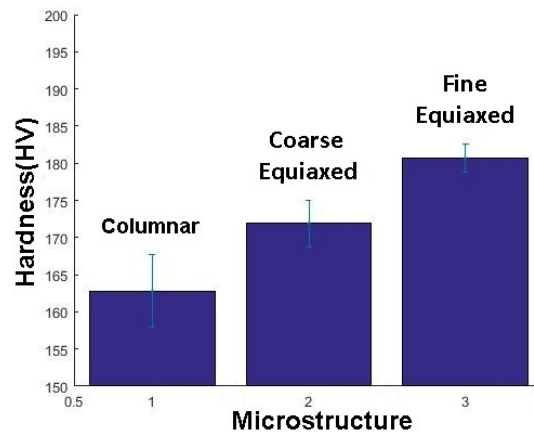


Figure 58: Trends in hardness values of different microstructures

6-4 Discussion

6-4-1 Microstructure

A Columnar to Equiaxed Transition was observed in grain morphology at high amounts of Fe wt% (>3.5%). A section of Cu-Fe phase diagram shown in Figure 59 offers insight into the observed behaviour.

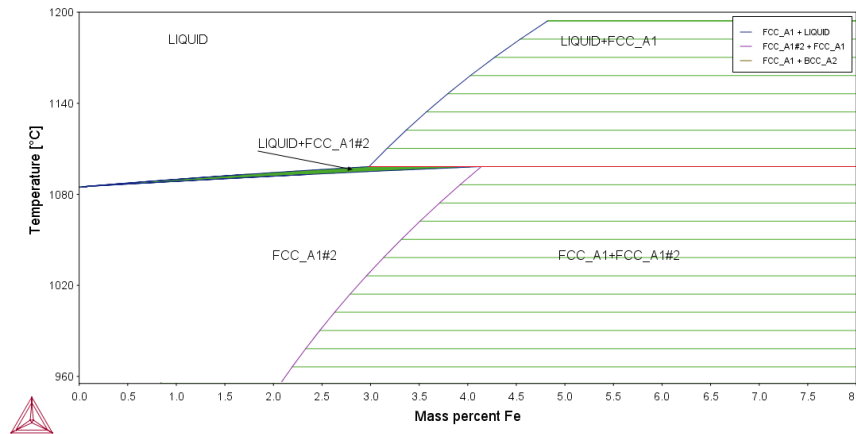


Figure 59: A section of Cu-Fe binary phase diagram. At Fe wt% > ~3%, peritectic region is observed. FCC A1 and FCC A1(2) are both copper rich phases

Based on the composition of Fe in the alloys, two different regions can be observed in the phase diagram. At Fe wt% < 3%, Cu-Fe single phase is found at elevated temperatures, however at Fe wt% > 3%, peritectic region is observed. This potentially results in differing mechanisms of grain refinement. The two key factors controlling grain refinement [61] are -

- potency, size and distribution of nucleating particles - role of inoculants
- local alloy chemistry, that triggers and sustains nucleation events through constitutional undercooling - role of solute

Wang et al. suggest that a low degree grain refinement is obtained from the constitutional undercooling components, particularly associated with segregation of solute atoms from single phase solidification front (speculated to be the case for microstructure in Figure 53 (b)). However, in peritectic regime, a high degree of grain refinement is obtained from both segregation and potent nuclei that promote heterogeneous nucleation [62]. Hence, equiaxed and refined grains are obtained for peritectic compositions of Fe wt% > 3% (in case of Figures 53 (c) and (d)). Further, this discussion is restricted to the role of inoculants in grain refinement. More investigations are needed to discuss the grain refining roles of several solute atoms present in the alloy system (Al, Mn, Ni, Si and Zn)

Free growth model by Greer et al. [63] is used to determine the potency of nucleants and to study the influence of particle distribution on grain refinement. According to the model, a grain grows from a particle at an undercooling which is inversely proportional to the diameter of the particle. For a fixed composition, particle diameter is also inversely proportional to particle density. Thus there is a trade off where larger particles are easier to grow upon but due to their lower density, they may be too few to contribute towards grain refinement.

It is speculated that the particle density factor dominated the phenomenon of grain refinement in the experiment. Larger particles in Figure 53 (c) were too few to form fine grains. Contrary to this, growth was sustained on fine particles in Figure 53 (d) resulting in a fine equiaxed microstructure.

The origin of local differences in particle distribution and the mechanisms of subsequent grain growth are beyond the scope of this work. Furthermore, modelling of the melt pool flow including redistribution of Fe and subsequent evolution of the microstructure should be explored. These preliminary results only indicate potential of using inoculants to tailor the microstructure of WAAM components.

6-4-2 Hardness

The trends in hardness values thus observed can be explained via means of various strengthening mechanisms namely grain boundary strengthening and dispersion strengthening [41]. Factors that influence local plastic deformation behaviour influence the hardness values in that region. Plastic deformation is governed by the ease of movement of dislocations within a polycrystalline material. Grain boundaries act as barriers to dislocation movement. The Hall-Petch relationship describes the relationship between strength of a material and its grain size. Yield strength is given by,

$$\sigma_o = \sigma_i + k'D^{0.5}$$

Here σ_i corresponds to frictional stress opposing motion of dislocation, k is the unpinning constant, that measures the extent to which dislocations are piled up at barriers and D is the average grain diameter. Hence, grain refinement contributes to strengthening of the microstructure. In addition to grain boundaries, the presence of fine particles in a ductile matrix also retards the motion of dislocations (dispersion strengthening). The degree of strengthening depends on the distribution of these particles. A parameter γ , being interparticle spacing is critical to the dispersion of particles and is given by,

$$\gamma = \frac{4(1-f)r}{3f}$$

Here f is the volume fraction of dispersoids and r is the particle size. Furthermore, depending upon the nature of matrix, dispersoids and mechanical loading, different deformation mechanism like dislocations cutting through dispersoids or bypassing them, can operate. Further investigation is needed to identify deformation mechanisms for the alloy system under discussion. For instance, bowing of dislocations in between non-deformable particles results in a Hall-Petch like relationship between interparticle spacing γ and strengthening [41]

$$\Delta\sigma = \sigma_o + k'\gamma^{1/2}$$

Hence, grain refined microstructures Figures 53 (c) and (d) have a higher hardness than the columnar microstructure due to grain boundary strengthening. Further, the microstructure with finely dispersed particles, has lower γ (a smaller r with a constant f) and hence higher strengthening contribution from dispersion strengthening.

6-5 Conclusions

Microstructure control strategies for improvement of mechanical properties during wire and arc additive manufacturing have been explored. Small quantities of Fe were introduced locally in the melt pool using a GTAW setup. The evolution of microstructure and trends in hardness of the microstructure are investigated. Following conclusions can be drawn-

- Upon addition of Fe to wt% $> \sim 3\%$, a distinct Columnar to Equiaxed Transition and grain refinement is observed in the microstructure owing to introduction of potent nuclei for heterogeneous nucleation in the peritectic regime.
- Based on local composition and distribution of Fe rich inoculant particles, the microstructure was categorized into columnar (Fe wt% $< 3\%$), coarse equiaxed (Fe wt% $> 3\%$, large Fe particles) and fine equiaxed (Fe wt% $> 3\%$, fine Fe particles)
- The hardness values of the microstructural regions increase in the order - columnar, coarse equiaxed and fine equiaxed owing to grain boundary strengthening and dispersion strengthening

Further investigations into developing robust process control (by exploring powder blowing or wire feeding approaches) can potentially result in a homogeneous fine grain equiaxed microstructure with improved mechanical properties.

Chapter 7

Summary

In the current work, metallurgical aspects of Wire and Arc Additive Manufacturing (WAAM) of Manganese Aluminium Bronze (MAB) are addressed. A conventional GTAW setup mounted on a CNC stage capable of motion along X,Y and Z axis has been used to deposit the filler wire. Influence of process parameters and complex thermal cycling on the evolution of microstructure is studied. Further, in-situ alloying during deposition has been explored as a process control strategy to tailor the microstructure. Susceptibility towards selective phase corrosion is evaluated for WAAM processed and in-situ alloyed material. Lastly, improved mechanical behaviour has been achieved through grain refinement during deposition.

7-1 Conclusions

The key conclusions from the work can be summarized as follows -

- During deposition of MAB single bead, the primary solidification microstructure consists of columnar and equiaxed β grains. For low heat input, columnar grains are prominent whereas at high heat input, morphology is predominantly equiaxed.
- Upon cooling, non equilibrium β phase transformations result in grain boundary, acicular and Widmanstätten α . Intermetallic precipitates can also be seen. Further, due to complex thermal cycling during WAAM, bands of coarse and fine grain morphologies are observed.
- In a MAB deposit, incremental addition of Cu₃Si filler wire while ensuring remelting and mixing results in a compositionally graded deposit. Solidification microstructure changes from dual phase to single phase due to reduction in aluminium wt %.
- Controlled in-situ alloying of MAB and Cu₃Si during deposition can be used to tailor phase fractions to achieve a single phase columnar microstructure (MABCu) can be achieved. It was observed that microstructural integrity of the new alloy is sensitive to thermal treatments as it is susceptible to void formation at elevated temperatures.

- The rate of corrosion for single phase MABCu was found to be almost 3 times less as compared to dual phase MAB based on Potentiodynamic Polarization analysis. Severe selective phase corrosion was observed on anodic beta phase of MAB surface whereas MABCu surface experienced a mild selective corrosion along the inter-dendritic precipitates.
- Introducing Fe within the melt pool during deposition is a promising approach towards improving mechanical behaviour of the alloy. Upon increasing Fe %wt to >3%, columnar to equiaxed transition was observed in the morphology
- Fe rich dispersoids within the melt pool act as potent nuclei for heterogeneous nucleation thereby promoting equiaxed fine alpha grains. This resulted in improved mechanical behaviour based on grain boundary and dispersoid strengthening

7-2 Outlook

The current work only scratches the surface of microstructure control possibilities associated with wire and arc additive manufacturing. Additionally, due to the given time frame of the project, a plethora of fascinating metallurgical aspects have not been explored in depth. Further investigations are needed to develop a thorough understanding of phenomena associated with the work presented. Some suggestions for further explorations are recommended below.

- Solidification morphology maps can be developed to link process parameters with the resulting microstructure for a predictable process control. On microstructural front, use of pre-heated substrate can be explored for tailoring the microstructure.
- The in-situ alloyed MABCu is sensitive to thermal cycles. Hence evolution of microstructure during its WAAM processing needs further investigation. Silicon based precipitates are prone to void formation. A similar in-situ alloying analysis can thus be performed for a silicon free copper filler wire to avoid detrimental features.
- Potentio-dynamic Polarization experiments are not a comprehensive method tool to validate the complex corrosion behaviour of alloys. Advance microstructural techniques like Scanning Kelvin Probe Force Microscopy (SKPFM) can be used to investigate tendency towards selective phase corrosion.
- Investigations into stability of protective film, mechanism of corrosion and susceptibility towards other forms of corrosion like erosion, pitting and cavitation are needed to develop a holistic understanding of corrosion behaviour in marine environment.
- Further explorations are needed to define a robust process for addition of inoculants within melt pool. Insights into heat and mass transfer within the melt pool can help define process parameters for a fine homogeneous microstructure. Alternatively, micro-alloying additions of Ag, Zr and/or B can be explored for microstructure control.

Thus, the current work provides a basis for future explorations aimed at better understanding of Wire and Arc Additive Manufacturing of Manganese Aluminium Bronze.

Appendix A

Aging Analysis of MAB

MAB deposit was aged in Nabertherm furnace at different temperatures for 2.5 *hrs* and quenched in water. The parameters are tabulated below and the optical micrographs of the cross-sections of the deposit can be seen in the Figure. 60 and 61

Table 13: Heat treatment parameters for aging analysis of MAB

Temperature ($^{\circ}\text{C}$)	Time (hrs)	Cooling
650 $^{\circ}\text{C}$	2.5	Water Quench
750 $^{\circ}\text{C}$	2.5	Water Quench
850 $^{\circ}\text{C}$	2.5	Water Quench
950 $^{\circ}\text{C}$	2.5	Water Quench

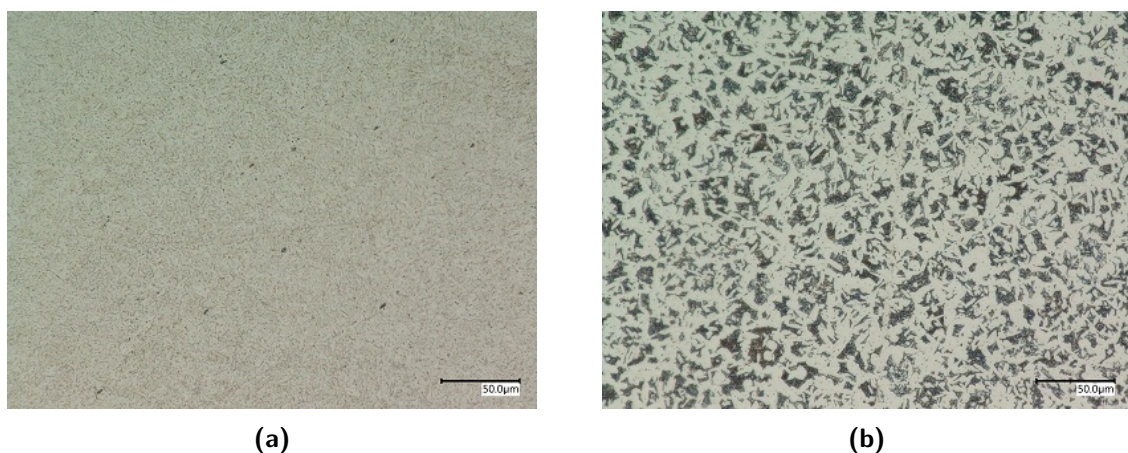


Figure 60: Optical micrographs of aged MAB samples at (a) 650 $^{\circ}\text{C}$ (b) 750 $^{\circ}\text{C}$

Samples aged at 750 $^{\circ}\text{C}$, 850 $^{\circ}\text{C}$ and 950 $^{\circ}\text{C}$ are dual phase where as the sample aged at 650 $^{\circ}\text{C}$ is predominantly single phase. Coarsening was also observed from 850 $^{\circ}\text{C}$ and 950 $^{\circ}\text{C}$ samples.

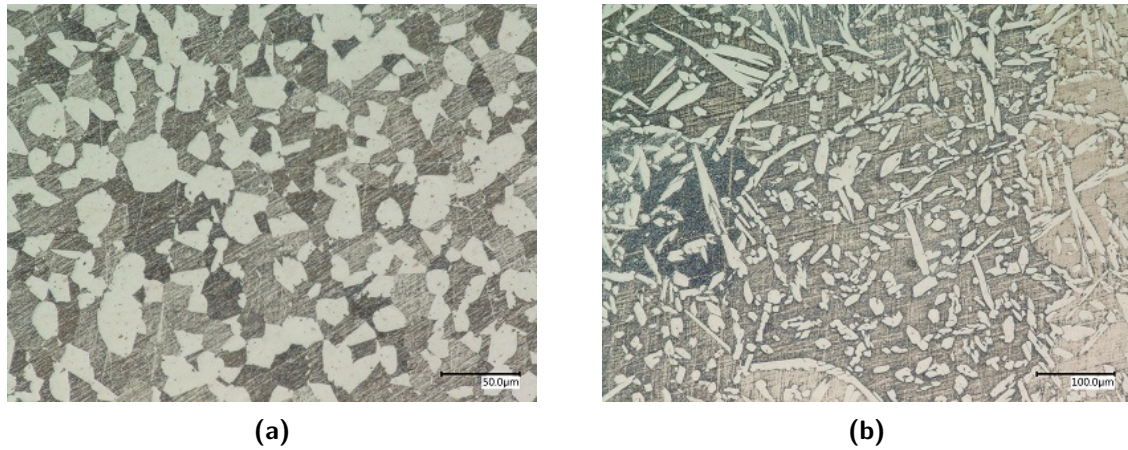


Figure 61: Optical micrographs of aged MAB samples at (a) 850 °C (b) 950 °C

XRD pattern of the MAB sample aged at 650 °C is shown in Figure 62. The amount of β phase has significantly reduced.

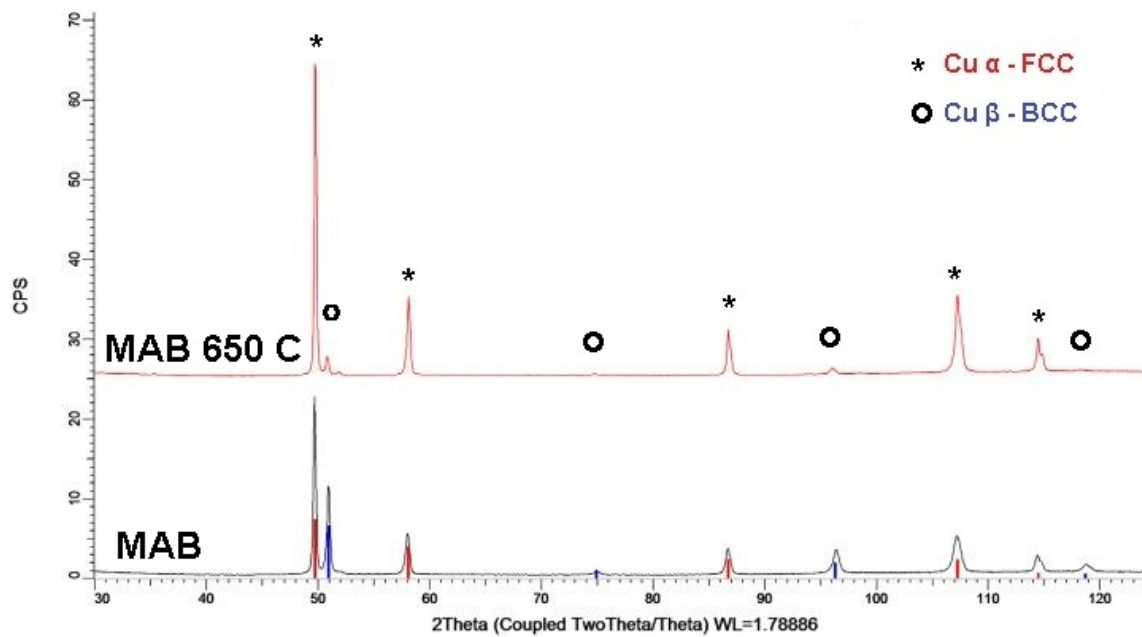


Figure 62: XRD pattern of MAB aged at 650 °C and MAB as-deposited

Appendix B

Process Parameter - In-situ Alloying

Cu3Si filler wire was deposited on a MAB deposit using parameters tabulated below in Table 14. Process parameters for initial MAB deposit are also included in row 1.

Table 14: Parameter selection for in-situ alloying

Material	Current (A)	Travel Speed (mm/s)	Feed Rate (mm/s)
MAB	150	3	36
Cu3Si (1)	125	3	24
Cu3Si (2)	150	3	24
Cu3Si (3)	175	3	24

Macrographs of cross-sections of the deposits are shown below in Figure 63

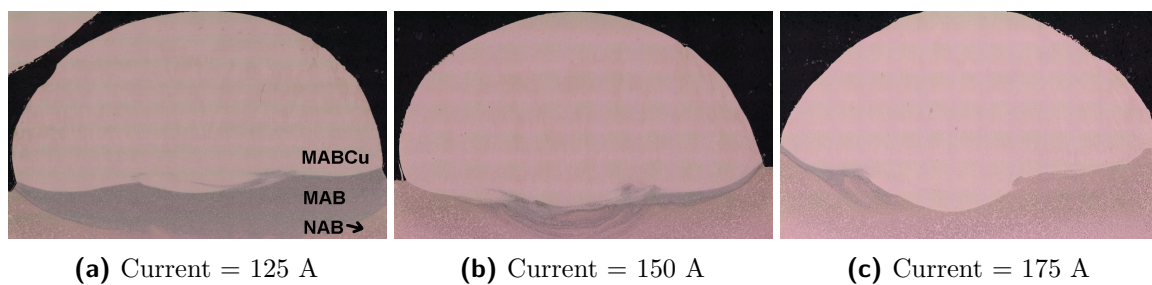


Figure 63: Macrographs of in-situ alloyed deposits. Differences in re-melting and mixing between MAB and Cu3Si are observed

Incomplete mixing and remelting was observed for welding current of 125 A. On the other hand, 175 A current resulted in remelting of the base plate as well. At a welding current of 150 A, optimal remelting and mixing was obtained. Hence, the graded deposit and optimal alloy were deposited using this value (section 4-2).

Bibliography

- [1] W. Callister and D. Rethwisch, *Materials Science and Engineering: An Introduction*. Wiley, 2010.
- [2] E. Herderick, “Additive manufacturing of metals: A review,” *Materials Science and Technology*, pp. 1413–1425, 2011.
- [3] S. M. Kelly and S. L. Kampe, “Microstructural evolution in laser-deposited multilayer ti-6al-4v builds: Part i. microstructural characterization,” *Metallurgical and Materials Transactions A*, vol. 35, pp. 1861–1867, Jun 2004.
- [4] F. Wang, S. Williams, P. Colegrove, and A. A. Antonysamy, “Microstructure and Mechanical Properties of Wire and Arc Additive Manufactured Ti-6Al-4V,”
- [5] W. E. Frazier, “Metal Additive Manufacturing: A Review,” *Journal of Materials Engineering and Performance*, vol. 23, pp. 1917–1928, jun 2014.
- [6] “Measurement Science Roadmap for Metal-Based Additive Manufacturing,” 2013.
- [7] D. Ding, Z. Pan, D. Cuiuri, and H. Li, “Wire-feed additive manufacturing of metal components: technologies, developments and future interests,” *The International Journal of Advanced Manufacturing Technology*, vol. 81, pp. 465–481, Oct 2015.
- [8] Srcthor, “Marine propeller fabricated using waam: Ramlab rotterdam,” 2017.
- [9] R. Ferrara and T. Caton, “Review of dealloying of cast aluminum bronze and nickel-aluminum bronze alloys in sea water service,” *MATER PERFORMANCE*, vol. 21, no. 2, pp. 30–34, 1982.
- [10] M. Fuller, S. Swaminathan, A. Zhilyaev, and T. McNelley, “Microstructural transformations and mechanical properties of cast nial bronze: Effects of fusion welding and friction stir processing,” *Materials Science and Engineering: A*, vol. 463, no. 1, pp. 128 – 137, 2007. TMS 2006, Mukherjee Symposium.

- [11] D. Ding, Z. Pan, S. van Duin, H. Li, and C. Shen, "Fabricating superior NiAl bronze components through wire arc additive manufacturing," *Materials*, vol. 9, no. 8, 2016.
- [12] J. Bailey, R. Francis, J. Galsworthy, D. Meigh, C. Powell, L. Tikana, C. Tuck, and P. Webster, "Guide to Nickel Aluminium Bronze for Engineers," 2016.
- [13] H. J. T. A. T. T. Meigh, "Cast and wrought aluminium bronzes : properties, processes and structure," 2008.
- [14] J. Iqbal, F. Hasan, and F. Ahmad, "Characterization of Phases in an As - cast Copper - Manganese - Aluminum Alloy," *J . Mater . Sci . Technol*, vol. 22, no. 6, 2006.
- [15] F. Hasan, A. Jahanafrooz, G. W. Lorimer, and N. Ridley, "The Morphology, Crystallography, and Chemistry of Phases in As-Cast Nickel-Aluminum Bronze,"
- [16] C. Tang, F. Cheng, and H. Man, "Improvement in cavitation erosion resistance of a copper-based propeller alloy by laser surface melting," *Surface and Coatings Technology*, vol. 182, pp. 300–307, apr 2004.
- [17] D. Arnaud, "CARACTERISTIQUES MECANIQUES A CHAUD DES ALLIAGES CUIVREUX MOULES.," pp. 393–406, nov 1972.
- [18] K. Oh-Ishi and T. R. McNelley, "Microstructural modification of as-cast NiAl bronze by friction stir processing," vol. 35 A, pp. 2951–2961, sep 2004.
- [19] Q. Luo, Z. Wu, Z. Qin, L. Liu, and W. Hu, "Surface modification of nickel-aluminum bronze alloy with gradient Ni-Cu solid solution coating via thermal diffusion," *Surface and Coatings Technology*, vol. 309, pp. 106–113, 2017.
- [20] G. den Ouden and M. J. M. Hermans, *Welding technology TT -*. Delft :: VSSD,, 1st ed. ed.
- [21] C. Körner, H. Helmer, A. Bauereiß, and R. F. Singer, "Tailoring the grain structure of IN718 during selective electron beam melting," *MATEC Web of Conferences*, vol. 14, no. 08001, 2014.
- [22] J. D. Hunt, "Steady state columnar and equiaxed growth of dendrites and eutectic," *Materials Science and Engineering*, 1984.
- [23] Y. Lee, M. Nordin, S. S. Babu, and D. F. Farson, "Effect of Fluid Convection on Dendrite Arm Spacing in Laser Deposition," *Metallurgical and Materials Transactions B*, vol. 45, pp. 1520–1529, aug 2014.
- [24] P. C. Collins, D. A. Brice, P. Samimi, I. Ghamarian, and H. L. Fraser, "Microstructural Control of Additively Manufactured Metallic Materials," *Annu. Rev. Mater. Res*, vol. 46, pp. 63–91, 2016.
- [25] L. Thijs, F. Verhaeghe, T. Craeghs, J. V. Humbeeck, and J.-P. Kruth, "A study of the microstructural evolution during selective laser melting of ti-6al-4v," *Acta Materialia*, vol. 58, no. 9, pp. 3303 – 3312, 2010.
- [26] P. Mercelis and J. Kruth, "Residual stresses in selective laser sintering and selective laser melting," *Rapid Prototyping Journal*, vol. 12, pp. 254–265, oct 2006.

-
- [27] C. Qiu, G. Ravi, and M. M. Attallah, "Microstructural control during direct laser deposition of a β -titanium alloy," *Materials & Design*, vol. 81, pp. 21–30, sep 2015.
- [28] H. Ren, D. Liu, H. Tang, X. Tian, Y. Zhu, and H. Wang, "Microstructure and mechanical properties of a graded structural material," *Materials Science and Engineering: A*, vol. 611, pp. 362 – 369, 2014.
- [29] P. A. Kobryn and S. L. Semiatin, "The laser additive manufacture of Ti-6Al-4V," *JOM*, vol. 53, pp. 40–42, sep 2001.
- [30] R. Banerjee, S. Nag, S. Samuel, and H. Fraser, "Laser-deposited Ti-Nb-Zr-Ta orthopedic alloys," *Journal of Biomedical Materials Research Part A*, vol. 78A, pp. 298–305, aug 2006.
- [31] S. Nag, S. Samuel, A. Puthucode, and R. Banerjee, "Characterization of novel borides in ti-nb-zr-ta+2b metal-matrix composites," *Materials Characterization*, vol. 60, no. 2, pp. 106 – 113, 2009.
- [32] Y. Ma, D. Cuiuri, N. Hoye, H. Li, and Z. Pan, "Characterization of In-Situ Alloyed and Additively Manufactured Titanium Aluminides," *Metallurgical and Materials Transactions B: Process Metallurgy and Materials Processing Science*, vol. 45, no. 6, pp. 2299–2303, 2014.
- [33] H. B. Cary, *Modern welding technology*. Prentice Hall: Prentice Hall, 2011.
- [34] Wikipedia, the free encyclopedia, "Gas tungstun arc welding," 2017. [Online; accessed August 15, 2017].
- [35] J. Chapuis, E. Romero, F. Soulié, C. Bordreuil, and G. Fras, "Transient behaviour of deposition of liquid metal droplets on a solid substrate," *Heat and Mass Transfer*, vol. 52, pp. 2283–2292, oct 2016.
- [36] M. M. RAHNI, B. BEIDOKHTI, and M. HADDAD-SABZEVAR, "Effect of filler metal on microstructure and mechanical properties of manganese–aluminum bronze repair welds," *Transactions of Nonferrous Metals Society of China*, vol. 27, no. 3, pp. 507 – 513, 2017.
- [37] J. E. Potts, T. L. Smith, and H. Cheng, "Electron beam pumped lasing in znse grown by molecular beam epitaxy," *Applied Physics Letters*, vol. 50, no. 1, pp. 7–9, 1987.
- [38] C. Liu, X. Tian, H. Tang, and H. Wang, "Microstructural characterization of laser melting deposited ti-5al-5mo-5v-1cr-1fe near titanium alloy," *Journal of Alloys and Compounds*, vol. 572, pp. 17 – 24, 2013.
- [39] Z. Tanabe, "EFFECT OF METAL COMPOSITION AND HEAT TREATMENT ON DE-ALUMINIFICATION OF Cu-A1 ALLOYS*,"
- [40] Copper Development Association Inc., "Aluminum Bronzes," 2009.
- [41] G. Dieter, "Mechanical metallurgy. 3rd ed., mc graw-hill book co., new york 1986. xxiii + 751 p., dm 138.50, isbn 0-07-016893-8," 1986.

- [42] M. Bermingham, D. Kent, H. Zhan, D. StJohn, and M. Dargusch, "Controlling the microstructure and properties of wire arc additive manufactured ti-6al-4v with trace boron additions," *Acta Materialia*, vol. 91, pp. 289 – 303, 2015.
- [43] D. A. Porter, K. E. Easterling, and M. Y. Sherif, *Phase transformations in metals and alloys*. Boca Raton FL: CRC Press, 3rd ed. / ed., 2009.
- [44] M. Rappaz, J.-M. Drezet, and M. Gremaud, "METALLURGICAL AND MATERIALS TRANSACTIONS A A New Hot-Tearing Criterion,"
- [45] B. G. Ateya, E. A. Ashour, and S. M. Sayed, "Corrosion of α -Al Bronze in Saline Water,"
- [46] H. J. Leidheiser, "The corrosion of copper, tin and their alloys," p. 82, 1971.
- [47] A. Hossain, M. A. Gafur, F. Gulshan, and A. S. W. Kurny, "Electrochemical investigation of the corrosion behavior of heat treated Al-6Si-0.5Mg-xCu (x=0, 0.5 and 1) alloys," *Journal of Electrochemical Science and Engineering*, vol. 5, mar 2015.
- [48] D. Jones, *Principles and Prevention of Corrosion*. Macmillan, 1992.
- [49] B. Sabbaghzadeh, R. Parvizi, A. Davoodi, and M. H. Moayed, "Corrosion evaluation of multi-pass welded nickel-aluminum bronze alloy in 3.5% sodium chloride solution: A restorative application of gas tungsten arc welding process," *Materials and Design*, 2014.
- [50] F. Walsh, "Flow influenced electrochemical corrosion of nickel aluminium bronze - Part I. Cathodic polarisation," *Journal of Applied Electrochemistry*.
- [51] G. Kear, B. Barker, and F. Walsh, "Electrochemical corrosion of unalloyed copper in chloride media—a critical review," *Corrosion Science*, vol. 46, no. 1, pp. 109 – 135, 2004.
- [52] A. M. Alfantazi, T. M. Ahmed, and D. Tromans, "Corrosion behavior of copper alloys in chloride media," *Materials and Design*, vol. 30, no. 7, pp. 2425–2430, 2009.
- [53] A. L. Bacarella and J. C. Griess, "The Anodic Dissolution of Copper in Flowing Sodium Chloride Solutions Between 25 and 175C," *Journal of The Electrochemical Society*, vol. 120, p. 459, apr 1973.
- [54] D. Tromans and J. C. Silva, "Behavior of copper in acidic sulfate solution: Comparison with acidic chloride," *CORROSION*, vol. 53, no. 3, pp. 171–178, 1997.
- [55] A. Antonysamy, J. Meyer, and P. Prangnell, "Effect of build geometry on the β -grain structure and texture in additive manufacture of ti6al4v by selective electron beam melting," *Materials Characterization*, vol. 84, pp. 153 – 168, 2013.
- [56] B. S. Murty, S. A. Kori, and M. Chakraborty, "Grain refinement of aluminium and its alloys by heterogeneous nucleation and alloying," *International Materials Reviews*, vol. 47, no. 1, pp. 3–29, 2002.
- [57] T. Mukai, M. Yamanoi, H. Watanabe, and K. Higashi, "Ductility enhancement in az31 magnesium alloy by controlling its grain structure," *Scripta Materialia*, vol. 45, no. 1, pp. 89–94, 2001.

-
- [58] W. Kurz and D. Fisher, *Fundamentals of solidification*. No. v. 1, Trans Tech Publications, 1986.
- [59] M. J. Balart, J. B. Patel, F. Gao, and Z. Fan, “Grain Refinement of Deoxidized Copper,” *Metallurgical and Materials Transactions A: Physical Metallurgy and Materials Science*, 2016.
- [60] H. Pal, S. K. Pradhan, and M. De, “Characterization of deformed and as-cast microstructure of copper-aluminium-iron alloys (α -phase),” *Japanese Journal of Applied Physics*, vol. 32, no. 3R, p. 1164, 1993.
- [61] M. Easton, M. Qian, A. Prasad, and D. StJohn, “Recent advances in grain refinement of light metals and alloys,” *Current Opinion in Solid State and Materials Science*, vol. 20, pp. 13–24, feb 2016.
- [62] F. Wang, Z. Liu, D. Qiu, J. A. Taylor, M. A. Easton, and M.-X. Zhang, “Revisiting the role of peritectics in grain refinement of al alloys,” *Acta Materialia*, vol. 61, no. 1, pp. 360 – 370, 2013.
- [63] A. Greer, A. Bunn, A. Tronche, P. Evans, and D. Bristow, “Modelling of inoculation of metallic melts: application to grain refinement of aluminium by al-ti-b,” *Acta Materialia*, vol. 48, no. 11, pp. 2823 – 2835.

